Influence of Thermal Resistance on Heat Distribution of Selected Parts of Low-Pressure Turbine of Aircraft Engines

Bartosz Zacharko, MSc, Eng.
Faculty of Mechanical Engineering and Aeronautics
Rzeszow University of Technology

Supervision: Robert Smusz, DSc, PhD, Eng., Associate Professor
Auxiliary supervisor: Wojciech Bar, MSc, Eng.

This dissertation is submitted for the degree of
Doctor of Philosophy

2021

Streszczenie pracy

Podstawowym celem doktoratu wdrożeniowego jest wypracowanie korelacji, która pozwoli na poprawne modelowanie wymiany ciepła w rejonie kontaktów pomiędzy wybranymi częściami turbinowego silnika lotniczego. W szczególności dotyczy to takich obszarów jak: platforma zewnętrzna łopatek kierowniczych turbiny niskiego ciśnienia będąca w kontakcie z zewnętrzną obudową turbiny, połączenie śrubowe obudowy turbiny z jej kołnierzem wylotowym, czy styk łopatki wirującej z dyskiem. Obecnie obszary te modelowane są prostą korelacją, która nie uwzględnia szeregu czynników wpływających na termiczny opór kontaktowy. Uzyskane rozkłady temperatur przy pomocy aktualnej metody wykazują dużą rozbieżność z wynikami eksperymentalnymi zebranymi z testów silników lotniczych oraz innych maszyn przepływowych. Rozbieżność ta stanowi duży problem w procesie projektowania i analiz komponentów silników lotniczych, ponieważ wprowadza duży margines błędu do obliczeń wymiarujących wytrzymałość statyczną i zmęczeniową projektowanych części. Wypracowanie korelacji pozwalającej na dokładniejszą analizę powyższych obszarów znacząco zmniejszyłoby niepewność analiz numerycznych na podstawie których podejmowane są krytyczne decyzje.

Prace nad korelacją zostaną przeprowadzone w **czterech etapach.**

I etap - Rozpoznanie i identyfikacja

W pierwszym etapie należy szczegółowo rozpoznać zagadnienie i zidentyfikować wszystkie czynniki wpływające na termiczny opór kontaktowy komponentów turbiny niskiego ciśnienia silnika lotniczego. Należy zidentyfikować mechanizmy wymiany ciepła, które powinny być uwzględnione w korelacji. Możemy mieć tu do czynienia z przewodzeniem pomiędzy elementami pozostającymi w kontakcie, promieniowaniem oraz konwekcją gazu przepływającego w szczelinach powierzchni kontaktowej. Dodatkowo należy rozpoznać pozostałe czynniki, które mogą wywierać wpływ na termiczny opór kontaktowy. Wstępnie zidentyfikowano: właściwości fizykochemiczne materiału i przepływającego płynu, siły nacisku, ciśnienia i siły masowe, struktura warstwy wierzchniej (fizyczna i geometryczna), rodzaj kontaktu i jego zmienność w czasie, warstwy ochronne (powłoki), wibracje silnika. Oprócz makroskopowej skali, z punktu widzenia doktoratu ważnym będzie rozważenie zagadnienia w aspekcie mikrostruktury powierzchni kontaktowych. Należy bowiem mieć na uwadze, że chropowatość oraz sposób wykończenia części zawsze jest określana z pewnymi odchyłkami od wymaganej wartości, która niepodważalnie ma wielki wpływ na zachodząca wymianę ciepła. Deformacje, które występują w wyżej wymienionych częściach również nie zawsze przebiegają w sposób jednolity i identyczny. Stąd też, istotnym będzie przeprowadzenie szczegółowej analizy czynników zewnętrznych pozwalającej określić ich rożne spektra wariacji i ostateczny wpływ na wartości współczynnika wymiany ciepła występującego na połączeniu analizowanych części.

II etap – Przegląd dostępnych korelacji

Kolejnym etapem prac będzie analiza dostępnych w literaturze badań eksperymentalnych i wypracowanych na ich podstawie korelacji analitycznych. Przegląd źródeł badań pozwoli na dokładniejsze poznanie metod badawczych wykorzystywanych do modelowania zjawiska termicznego oporu kontaktowego, analizy typów i zakresów warunków brzegowych oraz sposobu opisu zjawiska za pomocą matematycznych równań. Dzięki temu możliwe będzie również rozpoznanie najistotniejszych faktorów mających wpływ na wymianę ciepła w obszarze kontaktu oraz redukcję tych marginalnych. Wyniki studiów powinny posłużyć w przyszłości konfrontacji z obecnie stosowanymi metodami analityczno-numerycznymi wykorzystywanymi przez firmę MTU Aero Engines oraz do zastosowania nowatorskiego modelu numerycznego Lattice-Boltzmann (LBM) stworzonego w ramach omawianej pracy doktorskiej.

III etap – LBM

Trzeci etap prac obejmie wykorzystanie innowacyjnej metody symulacji numerycznych LBM w celu rozpatrzenia zjawiska termicznego oporu kontaktowego w mniejszej skali. Dane, których można nie uzyskać w sposób eksperymentalny, spróbują zostać oszacowane numerycznie. LBM jest techniką numeryczną, która pozwala na rozwiązanie równania Naviera-Stokesa dla przepływów nieściśliwych lub quasi-ściśliwych, gdy pominięto wpływ lepkości objętościowej. W przypadku przepływu gazu założenie o ciągłości strumienia nie zawsze jest spełnione dla mikro-przepływów, zwłaszcza w przypadku przepływów molekularnych. Równanie kinetyczne ruchu Boltzmanna opisuje przepływ dokładniej, co oznacza, że modele oparte na metodzie sieciowej Boltzmanna mogą być z powodzeniem stosowane w szerszym zakresie przypadków niż modele z wykorzystaniem metody skończonych objętości – od przepływów ciągłych do przepływów molekularnych. LBM jest uważany za numeryczny solver równania Boltzmanna. Równanie Boltzmanna jest analogiem równania Naviera-Stokesa na poziomie molekularnym, gdzie opisuje dynamikę czasoprzestrzenną wielkości statystycznej, zwaną funkcją rozkładu prawdopodobieństwa, która jest zdefiniowana w 6-wymiarowej przestrzeni fazowej. Liczba zjawisk fizycznych objętych modelem LBM na poziomie molekularnym jest większa niż na poziomie hydrodynamicznym równania Naviera-Stokesa. Co więcej, model molekularny jest w stanie wychwycić zjawiska związane z transportem temperatury, takie jak tarcie czy dyfuzja. Metoda LBM jest bardzo obiecującym modelem CFD, który odegra ważną rolę w kolejnych latach w dziedzinie obliczeniowej mechaniki płynów. Dlatego postanowiono też, aby symulację z wykorzystaniem modelu LBM skonfrontować z klasycznym modelem numerycznym.

Etap IV - Wdrożenie

Ostatnim etapem prac będzie zebranie wyników uzyskanych na podstawie analiz numerycznych. Dane zostaną wykorzystane do stworzenia odpowiedniej bazy stanowiącej fundament korelacji umożliwiającej bardziej precyzyjne wsparcie numerycznego modelowania rozpatrywanych obszarów silnika, a tym samym bardziej wiarygodną ocenę wytrzymałości danego połączenia, stopnia degradacji materiałów i ewentualnej optymalizacji kontaktu.

Słowa kluczowe: wymiana ciepła, turbina niskiego ciśnienia, termiczny opór kontaktowy, metoda gazu sieciowego Boltzmanna

Abstract

The main goal of this implementation PhD is to develop calculation procedure that will allow correct modelling of heat exchange in the areas of contact between selected parts of turbine aircraft engines. In particular, this applies to areas such as: the outer platform of the low-pressure turbine vanes connected to the outer turbine housing, the connection of the turbine casing with the turbine exhaust case, or the rotor blade to the disc. Currently, these areas are modelled by a simple correlation that does not take into account a number of factors affecting contact resistance. The temperature distributions obtained using this method show a large discrepancy with the experimental results collected from tests of aircraft engines and flow machines. This discrepancy causes a significant problem in the design and analysis of aircraft engine components, because it introduces a large margin of error when calculating the static and fatigue strength of the designed parts. The development of an accurate calculation procedure, allowing the analysis of these areas, would significantly reduce the uncertainty of numerical analyses on the basis of which critical decisions are made.

Work on the calculation procedure was carried out in **four stages.**

Stage I - Recognition and identification

In the first stage, the identification of all factors affecting the thermal contact resistance of the low-pressure components of the aircraft engine were studied in detail. The heat transfer mechanisms that will be included in the calculation procedure, i.e. the conduction between the elements in contact, radiation (which is usually neglected), and the convection of flowing gas in contact surface gaps should be considered. Additionally, other factors that may influence thermal contact resistance should be determined. The following factors were initially identified: physicochemical properties of the material and flowing fluid, pressure forces, mass forces, structure of the surface layer (physical and geometric), type of contact and its variability in time, protective layers (coatings), and engine vibrations. In addition to the macroscopic scale, from the point of view of this PhD thesis, it will be important to consider the issue in terms of contact surface microstructure. It should be taken into account that the roughness and finishing method of the part is always determined with some deviations from the required value which undeniably has a great impact on the heat exchange that takes place. Deformations that

occur in the above-mentioned parts also do not always run in a unified and identical manner. Therefore, it will be important to conduct a detailed statistical analysis that allows for the determination of different variation spectra and their definitive influence on the values of the heat exchange coefficient occurring at the connection of the analysed parts.

Stage II - Review of available correlations

The next stage of work will be the analysis of available experimental studies and analytical correlations based on them. Review of the research sources will allow a more accurate understand the experimental methods of modelling the phenomenon of thermal contact resistance, analysis of types and ranges of boundary conditions, and description of the above with use of mathematical equations. Thanks to this, it will be possible to identify significant factors affecting heat transfer in the contact area and reduce margin ones. The study results should be utilised to confront the currently used analytical and numerical methods in MTU Aero Engines and presentation of the innovative Lattice-Boltzmann numerical model created for doctoral dissertation purposes.

Stage III - LBM

The third stage of investigation will consist of an innovative method of numerical simulations to supplement the baseline data for correlation. Data, that may be not obtained in an experimental way will be estimated numerically. An interesting experience will be to perform a numerical simulation using the Lattice-Boltzmann method. This process is a numerical technique that allows the solution of the Navier-Stokes equation, for incompressible or quasi-compressible flows, when the effect of volumetric viscosity is neglected.

For gas flow, the assumption of stream continuity is not always met for micro-flows, especially in the case of molecular flows. The kinetic equation of Boltzmann's motion describes the flow more accurately, which means that models based on the Lattice-Boltzmann Method (LBM) can be used successfully in a wider range of cases than models using the finite volume method—from continuous flows to molecular flows. LBM is considered to be the numerical solver of the Boltzmann equation. The Boltzmann equation is an analogue of the Navier-Stokes equation at the molecular level, where it describes the space-time dynamics of a statistical quantity, called the probability distribution function, which is defined in the 6-dimensional phase space. The number of physical phenomena covered by the LBM model at this molecular level is greater than at the hydrodynamic level of the Navier-Stokes equation. What is more, the molecular model is able to capture transport-related phenomena, such as friction, diffusion, and temperature transport, to obtain appropriate transport rates. The LBM method is a very promising CFD model, which will play an important role in the subsequent years in the field of computational fluid mechanics. Therefore, the simulation using LBM model will be confronted with the classic numerical models.

Stage IV - Implementation

The final stage of work on the dissertation will be the collection of results obtained on the basis of numerical analyses. The data will be used to create an appropriate base that is the fundament for a correlation, enabling more precise support of numerical modelling of considered engine areas. Thus, it will provide a more reliable assessment of the strength of a given connection, the degree of material degradation, and possible future optimisation of given contact parts.

Key words: heat transfer, low-pressure turbine, thermal contact resistance, lattice-Boltzmann method

Acknowledgement

Poniższą pracę doktorską zrealizowano przy udziale firmy MTU Aero Engines we współpracy z Wydziałem Budowy Maszyn i Lotnictwa Politechniki Rzeszowskiej. Z tej strony chciałbym podziękować za możliwość realizacji tematu pracy doktorskiej oraz wsparcia w trakcie trwania projektu dr Ewaldowi Lutum, dr Jochenowi Gier oraz koledze Rafałowi Architektowi. Jestem bardzo wdzięczny prof. PRz, dr hab. inż. Robertowi Smuszowi za objęcie profesjonalną merytoryczną opieką oraz prof. PRz, dr hab. inż. Joannie Wilk za szansę realizacji doktoratu. Podziękowania składam także prof. dr hab. inż. Markowi Orkisz, dr hab. Piotrowi Wygonik oraz Michałowi Kuźniar za wsparcie otrzymane podczas wszystkich lat studiów na Politechnice Rzeszowskiej. Finalne, lecz najważniejsze podziękowania kieruję w stronę moich rodziców, za nieustająca wiarę we mnie i ciągłe wsparcie, niezależnie co by się działo. Bez nich nie byłoby mnie w tym miejscu.

The following PhD thesis was carried out with MTU Aero Engines in cooperation with the Faculty of Mechanical Engineering and Aviation at the Rzeszow University of Technology. I would like to thank Dr. Ewald Lutum, Dr. Jochen Gier, and my friend Rafał Architekt for helping me to realise my PhD topic and for their support during the project. I am very grateful to prof. dr hab. inż. Robert Smusz for his professional, substantive support, and prof. dr hab. inż. Joanna Wilk for the chance to undertake this project. I would also like to thank prof. dr hab. inż. Marek Orkisz, dr hab. Piotr Wygonik and Michał Kuźniar for support received during all years of study at the Rzeszów University of Technology. Last but not least, special thanks go to my parents, for their constant faith in my character and their continuous support, no matter what happens. Without them, I would not be in this place.

Bartosz Zacharko
Rzeszów, 25/07/2020

Table of contents

List of symbols

Roman symbols

a - area of the contact spot

A - nominal area of the solid

A_n - nominal area of contact

A_e - area of sample

A_c - real area of contact

b_L - microscopic dimension of component

c – speed of sound

C - autocorrelation function

d - distance between mid-planes of the contacting surfaces

E - energy

F - force

g - shape factor of contact spots

h – heat transfer coefficient

Gr - Grashof number

k_B – Boltzmann constant

K- raw moment

Kn - Knudsen number

L_e - elementary length of profile

n - number of contact spots

n_{sum} - density of summits

m - average asperity slope

M - central moment

M_n - *n*th moment of the power function

Ma - Mach number

u - molecular velocity

P - power function

q – heat flux or wall location

r_c - radius of the contact spot for circular contacts

R - thermal resistance, gas constant, or autocovariance function

R_a - mean arithmetic roughness of surface profile

s - distance between contact spots

S - structure function

T - temperature

U - flow quantity

x, y, z - Cartesian coordinates

x_{BC} - boundary location

z - height of profile

Greek symbols

α - accommodation coefficient

β - radius of asperity curvature

δ - out-of-flatness

Δ - amplitude

η - resolution of the measuring instrument

λ - wavelength of roughness

ν – kinematic viscosity

Θ - characteristic structure function

ρ - curvature of surface

ρ_c - radius of curvature of the summit for circular contacts

σ- r.m.s. height of roughness or standard deviation of surface heights

σ' - r.m.s. slope of roughness or standard deviation of asperity slope

σ''- r.m.s. curvature of roughness or standard deviation of asperity curvature

σ_K - Kapitza resistance

τ - distance between two x coordinates of the profile in horizontal direction, torque, relaxation time, shear stress tensor

ω - frequency of roughness or collision frequency

Ω - random element set or collision operator

Other symbols

¯ - mean value

^ - dimensionless value

= - lattice value

Chapter 1: Introduction

When two rough surfaces are brought into contact, actual contact only occurs at certain discrete spots or micro-areas, while the non-contacting areas form vacuums or are filled with some medium (such as air, water or oil, etc.). Due to the difference of thermal conductivities of solids and interface materials (or non-interface materials), the heat flow through the solid surface may be limited, resulting in a heat transfer resistance at the interface, commonly known as thermal contact resistance (TCR).

The engineering definition of TCR is the ratio of the temperature drop at the contact interface to the average heat flux across the junction, which is also called thermal boundary resistance or thermal joint resistance in many papers or books. The inverse of TCR is thermal contact conductance (TCC). In fact, both terms are used to describe the heat transfer of the contact interface. Like many other engineering problems, TCR research includes two aspects: engineering applications and basic theories. On one hand, the goal of such research is to decrease (or increase) the TCR to meet practical needs. In order to reach the maximum efficiency of heat removal, the thermal contact component/cooler must be enhanced. On the other hand, it is equally important that the correlation equations, theoretical models, and numerical methods are explored to help predict the TCR before designing and creating the contact components, choosing the interstitial materials, and deciding on the assembly methods.

In order to develop theoretical models and methods for predicting TCR, it is necessary to conduct basic research on several levels: surface geometry, mechanics of contact areas, and thermal mechanisms. Theoretical prediction research can not only help to understand the physical mechanism of TCR, but also solve some practical engineering problems. Careful prediction of the TCR is important to thermal analysis and controlling the condition of aircraft engine parts. Considering a number of factors, it is possible to carry out detailed numerical analyses to know the impact of the TCR on heat distribution in engine components.

There are two different ways to numerically simulate fluid flow, i.e., one based on a macro-continuous model from top to bottom or a micro-discrete model from bottom to top. Using Euler and Navier-Stokes equations, classical numerical methods of finite difference method, finite volume method and finite element we can discretise the equations and obtain the linear equations to solve the problem. While such from top to bottom approaches are intuitive, there are still many discrepancies left. For example, such methods often focus on analysis from the continuous differential equations to the discrete algebraic equations of the truncation error, but ignore the discrete process of conservation of certain physical quantities. Furthermore, in dealing with complex flow systems, solving these types of nonlinear differential equations is very difficult or even impossible.

In recent years, much attention has been given to the Lattice Boltzmann method [1, 2] (hereinafter referred to as LBM). This method belongs to micro-discrete type based on the bottom to top approach. In the LBM method, the fluid is an abstract for a large number of micro-particles, and these micro-particles in a discrete lattice migrate and collide in accordance with a simple movement rule. By using particle statistics, is possible to get the macro movement of fluid characteristics.

LBM method also provides the possibility and the reality of macro and micro-system investigations. At the same time, LBM breaks the traditional concept of modelling of complex systems and provides for them an entirely new procedure based on a simple mathematical model. The evolution process of the LBM method is very simple, clear and its program is more concise than previously mentioned classical methods. The Lattice-Boltzmann Method involves calculations which are localised, with the natural parallelism, and are very suitable for large-scale parallel computations. Because of these advantages, LBM method is considered a promising technique of calculation and has generated strong interest among all enthusiasts of numerical methods. Hence in this paper, the usage of LBM method with an exemplary problem related to the phenomenon of thermal contact resistance, is going to be presented.

Chapter 2: Geometrical Solid Surface Characterisation

Among the most significant variables influencing heat flow through two bodies is the surface layer design. The thickness of such a layer can vary between one hundred micrometres to a few millimetres, based on the manufacturing method applied. In comparison to the majority of the material product, the surface layer, (being the internal border of the strong fabric), is defined by distinct physical and chemical properties. The above-mentioned characteristics gradually differ in direction perpendicularly to the solid's internal border, reaching its bulk numbers at a certain range from the border. The effects from this change are caused by lubricants, ferrous and other oxides, and also variations in the characteristics of crystals near the border that are plastically different and deformed. Differences generally occur in the surface layer's microstructure or texture, hardness, heat or electrical characteristics, or internal stress allocations.

The surface texture represents a regular or random deviation from the nominal layer that shapes the three-dimensional surface topography which is defined in turn by features such as:

- nano or micro-roughness – which is formed by fluctuations in the surface of short wavelengths, marked by hills and valleys of different amplitudes and gaps, which are vast compared to molecular dimensions,
- waviness – the imperfection of the layer of larger wavelengths. Wavelength may arise from variables such as deflections in the device or workpiece, vibrations, warm-up or strain warping. Waviness covers all irregularities with a distance larger than the roughness sample length and smaller than the wavelength of the sampling.
- lay that is the primary orientation of the predominantly manufacturing method determined by technology used in shaping process.
- flaws that are unnecessary, unforeseen, and unwanted texture interruptions.

Below, on figure 2.1 visual exhibit of unidirectional surface texture is presented.

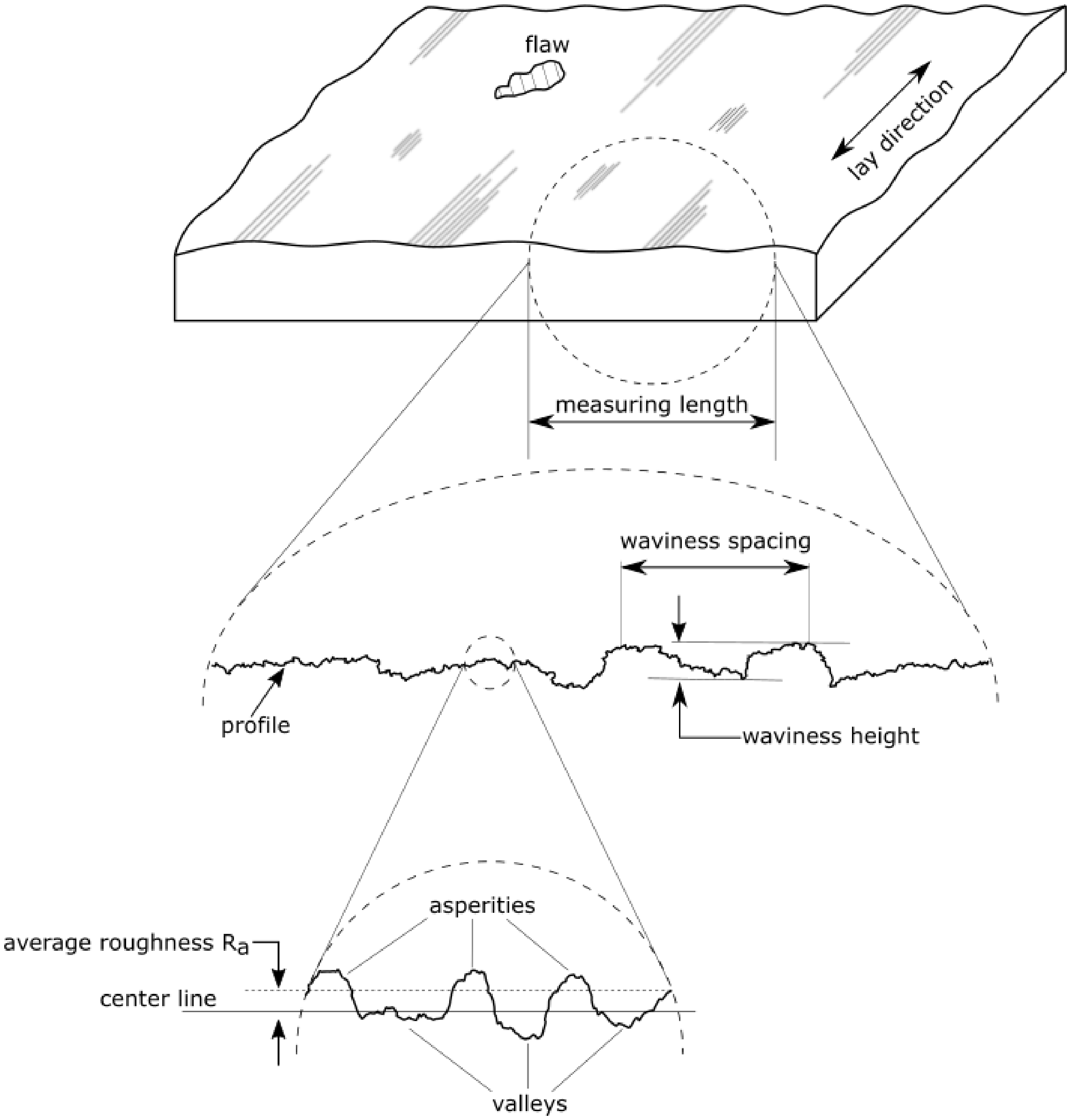

Fig. 2.1. Scheme of surface texture with its characteristic parameters

.

The texture may also involve large deviations in nominal shape, which is recognised as a mistake in form, they are usually not a component of the surface texture. The often-posed issue is whether different geometric features should be evaluated individually or collectively. All features however cannot normally be measured simultaneously. Which characteristic are included in the analysis relies on product applications.

As mentioned above, the solid surface's geometric structure is influenced by many relationships that may be deterministic, random, or both. Relatively easy analytical and empirical methods can examine deterministic surface textures because their thorough description is straightforward. However, most construction models' characteristics are arbitrary, either isotropic or anisotropic, and Gaussian or non-Gaussian.

An overall depiction of solid surface typology is shown below.

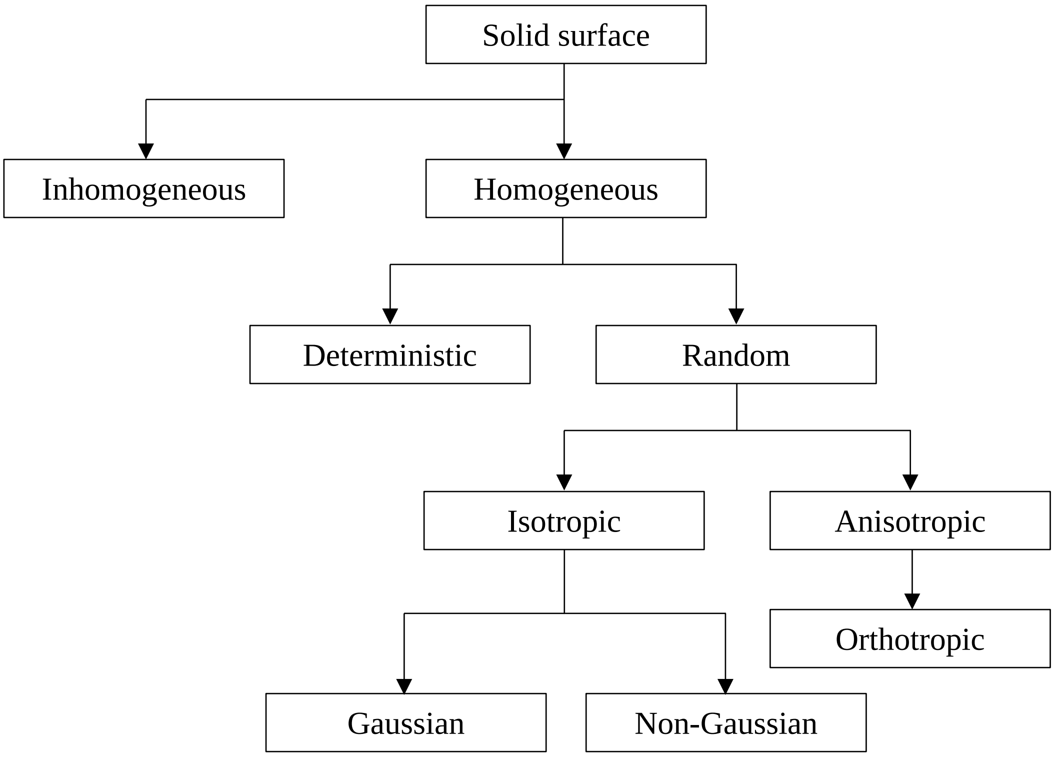

Fig. 2.2. General topology of solid body surfaces

The modelling of geometric interface details is required in order to compare experimental results of heat transfer across joints and develop theoretical patterns to describe this phenomenon. This classification is generally carried out on an average level where vertical and lateral interface data are described by their average results. The rough surface is structured quite uniformly and is generally presumed at first glance to be accidental [3]. It has recently been established that behind this noticeable accidentality, a certain order can be found when analysing the raw surface using fractal characterisation [4], [5].

Two rugged surfaces in contact were modelled and proven to be a smooth and an equivalent rough surface when in contact [6]. The issue of adequate characterisation of the equivalent layer is significantly reduced by this evidence. A relevant surface description for each of the contacting individual solids showed geometrical parameters of this corresponding layer. Furthermore, certain further simplifications are assumed in the modelling of the geometric surface structure. Perhaps most importantly, some stereometric characteristics of the entire layer can be characterised through readings conducted on different parts of the surface. Therefore, with the isotropic texture of the surface only one path can be found in a profilogram. Average values can be deterministically or statistically defined for these averaged parameters.

Currently, five distinct surface measuring instruments are accessible [7]:

- the stylus-type surface profilometer,
- the optical measurements based on white-light interference,
- the scanning electron microscope,
- the atomic force microscope, and
- the scanning tunnelling microscope.

Microscopic techniques are, on the other side, adequate for most engineering and production applications and these are usually mechanical or optical methods, such as stylus-shape profilometers or white light interference optical based measurement. Some of these procedures are also suitable for measuring surface geometric parameters. The measuring method can be split into two wide-ranging classifications:

a) a contact type where a measuring instrument element effectively contains the layer to be evaluated during testing,

b) a non-contact type.

If used with a sharp stylus tip, an instrument of contact type can damage surfaces, especially soft ones. Many other methods could have either been proven in the laboratory and have never been publicly used in specialised applications.

2.1 Deterministic Characterisation of Single Solid Surface

Averaging is supposed to occur on the A_e area of a sample in the deterministic description of a surface. The roughness of this sample is regarded as a trait of the whole surface and therefore, the sample can be treated as a certain representative, repetitive and basic element. A function describing the height of the surfaces *z(x,y)*, with their horizontal coordinates *x* and *y*, defines the surface shape. Any mean parameter connected with a function *f* that describes a surface feature can be mathematically described as [7]:

$$\langle f \rangle = A_e^{-1} \int_{A_e} f(x,y)\, dA_e \tag{2.1}$$

The local surface height, relative to the location of the mean plane (Fig. 2.3), is easily determined with the following formula:

$$\bar{z} = \langle z \rangle = A_e^{-1} \int_{A_e} z(x,y) dA_e \qquad (2.2)$$

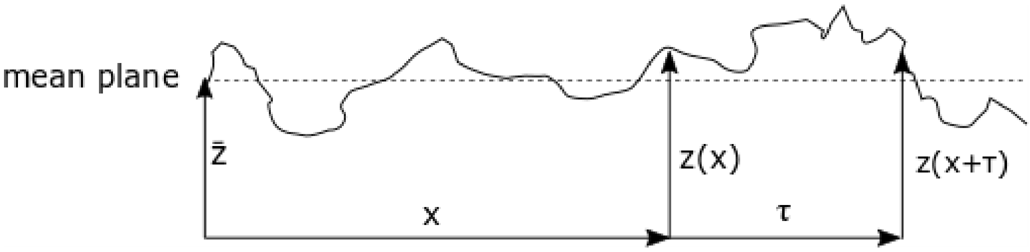

Fig. 2.3. Mean surface profile plane

For the majority of this text, the symbol *z* is understood as the roughness height which is measured in relation to the mean level. The mean plane is the nominal surface of the solid. Many mean parameters describe the raw surface both vertically and horizontally.

In the case of the surface with isotropic texture, the following parameters are the most frequently used for modelling of thermal exchange phenomena [7]:

- the root mean square (r.m.s.) deviation of surface height σ:

$$\sigma = \sqrt{L_e^{-1} \int_0^{L_e} [z(x)]^2 dx} \qquad (2.3)$$

where L_e is the sampling length of the profile (profile length)

- the r.m.s. slope σ' of the roughness:

$$\sigma' = \sqrt{L_e^{-1} \int_0^{L_e} \left[\frac{dz}{dx}(x)\right]^2 dx} \qquad (2.4)$$

and

- the r.m.s. curvature σ'' of the roughness:

$$\sigma'' = \sqrt{L_e^{-1} \int_0^{L_e} \left[\frac{d^2z}{dx^2}(x)\right]^2 dx} \qquad (2.5)$$

The latter parameter is regarded as the opposite of the asperity radius. The surface slope, at any stage on a surface, is acquired by identifying the square roots of the slope in two orthogonal x and y directions. The curvature can be obtained by finding the average curvature at any point on the surface on two orthogonal (x and y) axes [3]. The height information are added to determine the average height, tilt, and curvature in the least-square sense before the calculation of the roughness parameters.

2.1.1 Spatial Functions

The following sub-sections will help to understand what spatial functions are and how they are divided.

If we consider two sine wave surfaces with the same amplitude and distinct frequencies, we assume that they supposed to have the same R_a and σ, but different surface heights in spatial schemes. Features like slope and curvature are generally omitted because they are not sufficient to define the surface alone. They only refer to one specific spatial size of the features.

In such cases the so-called spatial functions are used. The spatial functions are a form of representation of the characteristics of all wavelengths or spatial dimensions. Due to the methodologies used by them, the following functions are distinguished:

- the autocovariance (or autocorrelation) function (ACVF/ACF),
- structure function (or variance) (SF/VF),
- power spectral density function (PSDF).

Listed above functions are also known as surface texture descriptors and will be next shortly described.

2.1.2 Auto-Covariance and Auto-Correlation Functions

The Auto-Covariance Function has been the most common manner of depicting temporal variety. The ACVF of a random function is understood as a criterion of how well potential variable outcomes can be forecast depending on previous experiences. It is formulated in following way [8]:

$$R(\tau) = \lim_{L \to \infty} \frac{1}{L} \int_0^L z(x) z(x + \tau) dx \tag{2.6}$$

The ACVF is the average value for the spatial separation of τ for the function $z(x)$ of the product of two readings on profile from distance $z(x)$ and $z(x+\tau)$. It is obtained by making comparison of the *z(x)* function to the replica of itself, where a replica has been moved for a distance τ (see Figure 2.3).

The standardized shape of the ACVF, called the Auto-Correlation Function (ACF), is given as:

$$C(\tau) = \lim_{L\to\infty} \frac{1}{L\sigma^2} \int_0^L [z(x) - m][z(x+\tau) - m]dx = [R(\tau) - m^2]/\sigma^2 \qquad (2.7)$$

The above formula shows also the relationship between the ACVF and the ACF.

By using one of following methods it possible to calculate the Auto-Correlation function:

- height distribution of the digitized profile,
- Fast Fourier Transform (FFT) method.

In second point by taking an FFT of the surface height and squaring the results we obtain a Power Spectral Density Function (one of the spatial functions). Then by utilizing an inverse FFT of the PSDF we receive the ACVF.

2.1.3 Structure Function

The second example of spatial functions is the Structure Function. For a *z(x)* profile, the structure function (SF) or variance function (VF) is expressed as:

$$S(\tau) = \lim_{L\to\infty} L^{-1} \int_0^L [z(x) - z(x+\tau)]^2 dx \qquad (2.8)$$

This formula reflects the mean square of the anticipated height difference over any range of space τ. SF's two main benefits are that its utilization is not restricted to the stationary cases, and it is independent of the mean plane. Moreover, it also includes the same data as the ACVF for stationary constructions.

The ACVF and ACF are linked to the structure function as follows:

$$S(\tau) = 2[\sigma^2 + m^2 - R|(\tau)] = 2\sigma^2[1 - C(\tau)] \qquad (2.9)$$

2.1.4 Power Spectral Density Function

Often the roughness of the surface is evaluated using spectral methods and therefore its Power Function is applied instead of the Auto-Correlation or Structure Function [9]. The rough profile is viewed in spectral analysis as an overlay of waves at various frequencies. The Power Function gives a relationship between the square of amplitude of waves and their frequency:

$$\omega = 2\pi/\lambda \tag{2.10}$$

where λ denotes wavelength of roughness.

Power function enables to discover long-wavelength shape flaws, medium wavelength periodic waviness and short-wavelength surface roughness. It also allows the deterministic (periodic) component of surface roughness and its random part to be found. The power function is linked to the previous Auto-Covariance Function by [10]:

$$\begin{aligned} P(\omega) &= P(-\omega) \\ &= \int_{-\infty}^{+\infty} R(\tau)\exp(-i\omega\tau)d\tau \\ &= \int_{-\infty}^{+\infty} \sigma^2 C(\tau)\exp(-i\omega\tau)d\tau + m^2\delta(\omega) \end{aligned} \tag{2.11}$$

where $i = \sqrt{-1}$.

The PSDF can also be achieved immediately from the Fourier transformation of *z(x)* by getting FFT of the profile information and squaring the outcomes as follows:

$$P(\omega) = \lim_{L\to\infty} \frac{1}{L_e}\left[\int_0^L z(x)\exp(-i\omega x)\,dx\right]^2 \tag{2.12}$$

Knowledge of the power function enables us to readily determine the variation of surface height, slope and curvature of the roughness. The squares of the latter parameters are generally equivalent to the moments of a distinct order of the Power Function identified as:

$$M_n = \frac{1}{2\pi}\int_{-\infty}^{+\infty} [P(\omega) - m^2\delta(\omega)]\omega^n d\omega \tag{2.13}$$

where m_n is known as the spectral moment of the *n*th order.

We note for a Gaussian function that [1]:

$$M_0 = \sigma^2 = \frac{1}{L_e}\int_0^{L_e} (z-m)^2 dx \tag{2.14}$$

$$M_2 = \sigma'^2 = \frac{1}{L_e}\int_0^{L_e} (dz/dx)^2 dx \tag{2.15}$$

$$M_4 = \sigma''^2 = \frac{1}{L_e}\int_0^{L_e} (d^2z/dx^2)^2 dx \tag{2.16}$$

where σ' and σ'' are the standard deviations of the first and second derivatives of the functions. For a surface/profile height, these are the surface/profile slope and curvature, respectively.

According to [3] a random and isotropic surface with a Gaussian height distribution can be adequately characterised by the three-zeroth (M_0), second (M_2) and fourth moments (M_4) of the Power Spectral Density Function.

Based on the principle of random processes, two features can fully characterise an irregular and isotropic object in a statistical context (rather than a deterministic context):

- the height density, and
- the Auto-Correlation Function (ACF).

2.2 Deterministic Characterisation of Two Surfaces

So far, a case of only one plane has been analysed, the next chapter describes co-action of two surfaces.

At the very beginning it is worth reminding that two surfaces can be regarded as a contact of a smoothly-flat and rigid layers (planes) that represents an equivalent surface, which is described as follows [10]:

$$z(x, y) = z_1(x, y) - z_2(x, y) \tag{2.17}$$

where z_1 and z_2 indicate each surface height (Fig. 2.4).

The mean planes of contacting surfaces are initially (before loading) separated by a gap d:

$$d = \bar{z}_1 - \bar{z}_2 \tag{2.18}$$

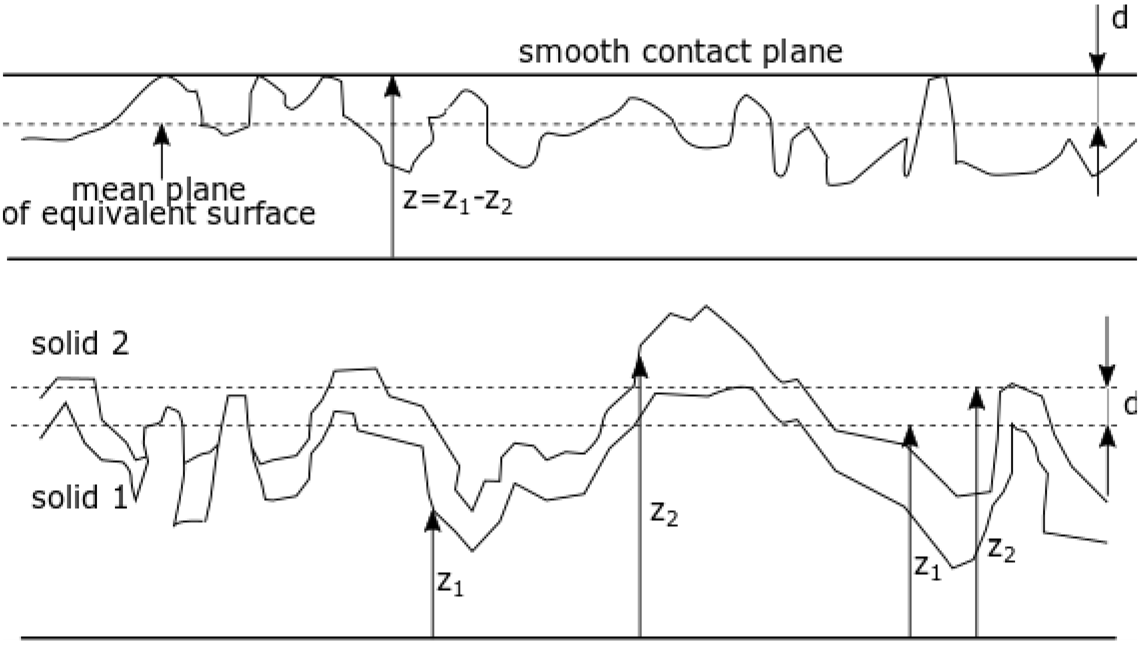

Fig. 2.4. The equivalent surface definition

If there is no correlation between the roughness of two contacting surfaces, the Power Function for the corresponding layer is the same as the total of the Power Functions for the separate surfaces:

$$P(\omega) = P_1(\omega) + P_2(\omega) \tag{2.19}$$

The same connection maintains for the Auto-Correlation and Structure Functions, moments of Power Function which are described as:

$$\begin{aligned} M_{0ef} &= M_{01} + M_{02} \\ M_{2ef} &= M_{21} + M_{22} \\ M_{4ef} &= M_{41} + M_{42} \end{aligned} \tag{2.20}$$

where M_e denotes the respective value (i=0,2,4) for each (j=1,2) of surfaces.

When both parts are compressed, a reduction of d parameter between the smooth contact plane and the mean plane of the corresponding layer occurs. (Fig. 2.5).

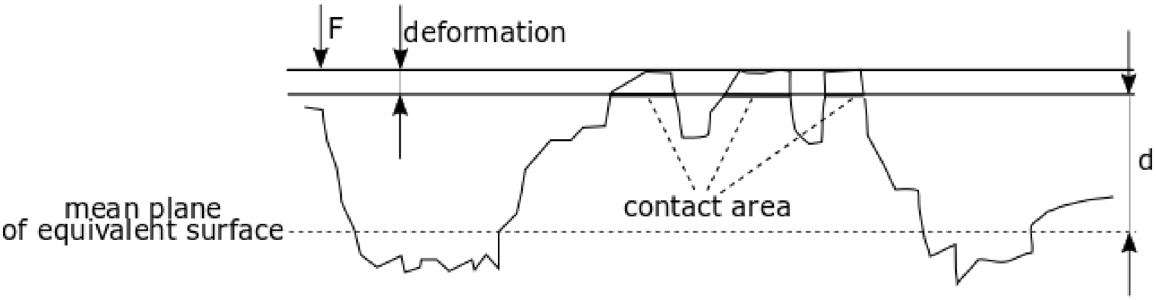

Fig. 2.5. The area of contact and its relation to the mean separation of the surfaces

Utilizing the assumption that the surface geometry doesn’t alter with compression, the area of real contact A_c, the mean number of contact spots n, the mean area of contact spots $\bar{a}$ and the mean distance between contact spots s , can be calculated by intersecting the surface by a plane at different distances d from the mean plane.

In order to assess the above parameters, the typical function of the rough surface described by the formula should be introduced:

$$\Theta(x,y,d) = \begin{cases} 0 \; for \; d > z(x,y) \\ 1 \; for \; d \; \leq z(x,y) \end{cases} \tag{2.21}$$

By taking an average of the characteristic function we can calculate the ratio of average mean area of the contact and nominal area:

$$A_c(d)/A_n = \langle \Theta(d) \rangle = A_e^{-1} \int_{A_e} \Theta(x,y,d)\, dA \tag{2.22}$$

The average amount of contact points n per unit surface area can be calculated as:

$$\bar{n} = \frac{n_x n_y}{g(\frac{A_c}{A_n})} \tag{2.23}$$

where n_x and n_y stands for number of contact spots in x and y direction respectively, g is the shape factor of the contact spot (g =1 for the rectangular cross section and $g = 4/\pi$ for the elliptical contact spot) [11].

With a knowledge about the true contact area and the average amount of contact points, the mean area of the contact spot and mean distance between contact spots can be calculated

$$\bar{a} = (A_c/A_n)/\bar{n} \tag{2.24}$$

$$\bar{s} = \sqrt{\bar{n}^{-1}} \tag{2.25}$$

The roughness mean wavelength can also be predicted, by the approximated value of the distance between the contact spots:

$$\bar{s} \approx \bar{\lambda} = 2\pi(\frac{\sigma}{\sigma'}) \tag{2.26}$$

Application of the fast Fourier transform to the function describing the surface leads to a relation between amplitude Δ_i and frequency f_i. From these data the asperity areal density n_i and radius of asperity curvature β_i can be computed for each frequency level according to [12]:

$$n_i = 2f_i^2 \tag{2.27}$$

$$\beta_i = \frac{1}{4\pi^2 \Delta_i f_i^2} \tag{2.28}$$

The real contact region is described as follows:

$$A_c = \left(\prod_{i=1}^{i_{max}} \bar{A}_{ci}\, n_i \right) A_n \tag{2.29}$$

where $\bar{A}_{ci}$ is the single asperity contact area at a certain frequency level, while i_{max}, refers to the highest level of frequency considered.

This definition refers to optically smooth contact layers whose the out-of-flatness parameter δ is of the same magnitude as the roughness of a surface and whose curvature of the surface does not affect the change in contact pressure distribution.

If the out-of-flatness is higher, i.e. if contact occurs on non-conforming rough surfaces, the contact with the equivalently rough and flat spherical surface shall be simplified. On the illustration below (Fig. 2.6) modelling of the contact between two non-conforming rough surfaces has been presented.

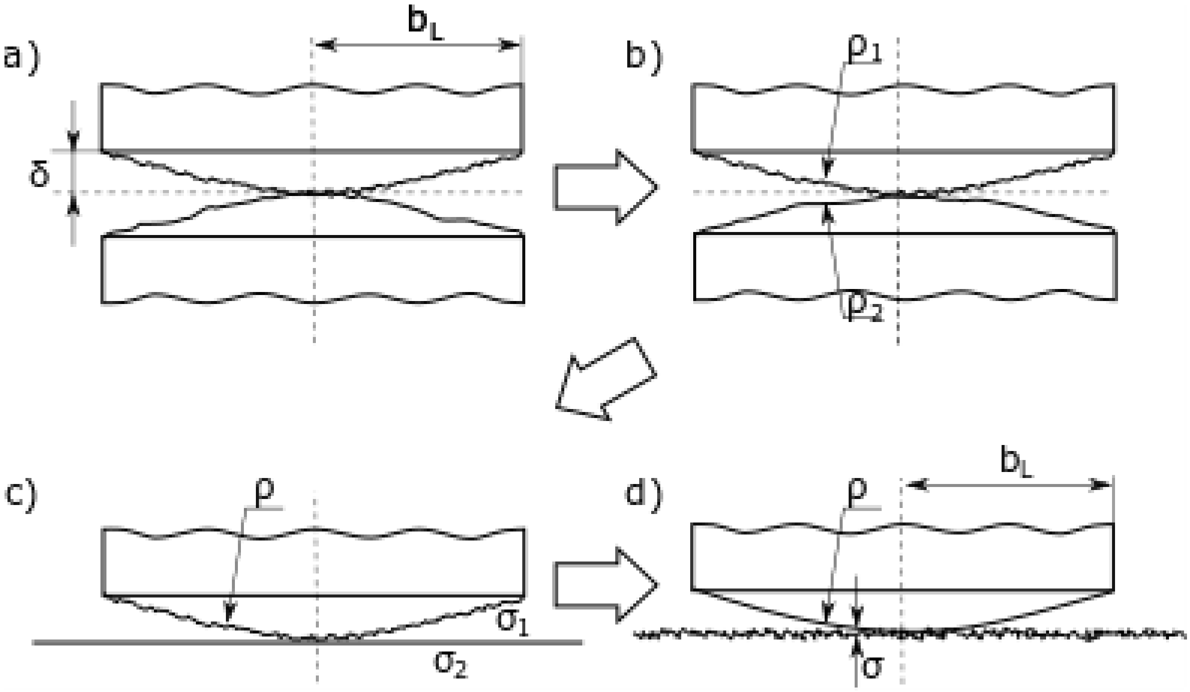

Fig. 2.6. Flow diagram of geometrical modelling: a) contact of non-conforming rough surfaces, b) contact of two spherical segments, c) rough sphere with effective radius of curvature — flat contact, d) equivalent sphere with effective radius of curvature — rough flat contact [13].

The out-of-flatness δ_i for *i*th surface can be linked to its radius of curvature ρ, for comparatively big radii of curvature with use of the following formula:

$$\rho_{ci} = \frac{b_L^2}{2\delta_i} \tag{2.30}$$

where b_L, stands for the macroscopic dimension of a component.

Additionally, the efficient curvature radius for two contact surfaces can be defined:

$$\frac{1}{\rho_{cef}} = \frac{1}{\rho_{c1}} + \frac{1}{\rho_{c2}} \tag{2.31}$$

2.3 Statistical Characterisation of Solid Surface

Due to the unique personality of roughness, the statistical method is very often used in classical design or roughness characteristics. This definition treats a rough surface as a random variable – an element Ω of the random array, where the probability function $\rho(\Omega)$ is represented. Any distinctive parameter which describes the rough surface is then recognised as the statistical average (anticipated valuation) for all set elements. Thus, one can define statistical mean for any function $f(x, y|\Omega)$ as:

$$f(x,y) = \int f(x,y|\Omega)\rho(\Omega)d\Omega \qquad (2.32)$$

where incorporation takes place over all rough surface realisations.

All mean parameters describing the characteristics of the rough surface, such as the mean plane $\bar{z}(x,y)$, the mean separation distance between the mean planes $d(x, y)$ of two rough surfaces, as well as the r.m.s. deviation of the profile $\sigma(x)$, slope $\sigma'(x)$ and curvature $\sigma''(x)$ are treated as statistical averages. The same applies to the Auto-Correlation $C(x,\tau)$, Power $P(x, \omega)$ and Structure $S(x, \tau)$ functions. All these quantities are typically varied by the location in (x, y) plane or along the x coordinate of the profile. The statistical method enables to readily identify homogeneous or inhomogeneous surfaces and their isotropy or anisotropy. The statistical homogeneity of the surface means that $\rho(\Omega)$ is autonomous of the place (x, y) on the surface.

The surface statistical isotropy is associated with a probability density invariance $\rho(\Omega)$ under different angle rotations and any plane reflections. The statistical average is usually distinct from the average surface area mentioned in the prior chapter but these two averages combined together may give the same consequence.

It happens in cases in which there is a stationary random process, that is, the statistical average does not differ from place to place. This is recognised as the ergodic rule. It is generally presumed that the ergodic theorem is present in the depiction of real surfaces.

Special consideration is paid to calculating the true contact region A_c between the two solids in the statistical depiction of contact. This area can be expressed in relation to the nominal area for the statically uniform surface, and when using the characteristic function $\bar{\Theta}(x,y|\Omega)$:

$$\frac{A_c(d)}{A_n} = \Theta(d) = \int \Theta(x,y,d|\Omega)\rho(\Omega)d\Omega \qquad (2.33)$$

One can differentiate, between those realisations acquired from others through transitions in the (x, y) plane, and clearly define the probability density as follows:

$$\rho(\Omega) = \rho(x',y')\rho(\Omega|x',y') \qquad (2.34)$$

where $\rho(x', y')$ is the probability density of finding point (x', y') on the considered plane and $\rho(\Omega|x', y')$ denotes the respective probability density of Ω when the point (x', y') has been already fixed. This allows to redefine definition (2.33) into the following form:

$$\begin{aligned}\frac{A_c(d)}{A} &= \{\Theta(d)\} = \\ &= \int\int_A [\Theta(x,y,d|\Omega)\rho(x',y')dA]\rho(\Omega|x',y')d(\Omega|x',y') \\ &= \int_d^{+\infty} f(z)dz\end{aligned} \tag{2.35}$$

where *f(z)dz* denotes the probability of finding *z* in the range *(z, z + dz)* while the expression, on the right-hand side of eq. (2.35) is the probability of making contact at any given asperity of the height *z*.

Experimentally, it has been discovered that for the rough and random surfaces, i.e. formed by grinding, *f(z)*. can be approximated by normal i.e. Gaussian distribution [14]:

$$f(z) = \frac{1}{\sqrt{2\pi}\sigma} e^{-\frac{z^2}{2\sigma^2}} \tag{2.36}$$

where σ is the standard deviation of profile heights.

Such surface with isotropic asperities randomly distributed on the surface is often called "the Gausian surface". For the Gausian surface the r.m.s. slope σ' is related to the average asperity slope *m* by the formula:

$$\sigma' \approx 1.25m \tag{2.37}$$

where the latter is defined by the formula:

$$m = L_e^{-1} \int_0^{L_e} \left|\frac{dz}{dx}(x)\right| dx \tag{2.38}$$

In the case when the average asperity slope is required but not recorded the following correlations between *m* and the standard deviation σ can be used for rough estimations [13]:

$$\begin{gathered} m = 0.152\sigma^{0.4} \\ m = 0.124\sigma^{0.743} \text{ for } \sigma \le 1.6\mu\text{m} \\ m = 0.076\sigma^{0.52} \end{gathered} \tag{2.39}$$

When the Gaussian profile is introduced into the definition of the surfaces in contact, eq. (2.25), the following expression relating the mean area of contact to the mean separation between the mean plans of contacting surfaces is obtained:

$$A_c/A_n = 0.5erfc\left(\frac{d}{\sqrt{2}\sigma}\right) \tag{2.40}$$

where *erfc(y)=1-erf(y)* and *erf(y)* is the error function.

The mean number of contact spots n_x per unit length of the profile can then be determined from the formula similar to eq. (2.17), i.e.:

$$\begin{aligned} n_x(d) &= \partial_x \Theta(d)s \\ &= \int\int_A [\partial_x \Theta(x,y,d|\Omega)\rho(x,y)dA]\rho(\Omega|x,y)d(\Omega|x,y) \\ &= \int_d^{+\infty}\int_{-\infty}^{+\infty} |\partial_x z|\, f(z,|\partial_x z|)d|\partial_x z|dz \end{aligned} \qquad (2.41)$$

The formula 2.42 can be considerably reduced if probability density distribution of the roughness heights and slope distributions are independent. If, additionally both these probability distributions are Gaussian then, the mean number of contact spots per unit area of the surface can be expressed as:

$$n(d) = \frac{n_x n_y}{g(A_c/A_n)} = \frac{1}{4\pi^2 g}\frac{\sigma'_x\sigma'_y}{\sigma_x\sigma_y}\exp\,[-(d/\sigma)^2] \qquad (2.42)$$

where σ'_x, σ'_y stand here for the standard deviation of surface slopes in *x* and *y* directions for the equivalent surface.

The relations between standard deviations (variances) in surface heights, slopes and curvatures of the equivalent surface and the contacting surfaces are the same as those shown in eq. (2.14).

For the circular contact spots the mean areal number of contact spots can be found from the formula [15]:

$$n(d) = \frac{1}{16}\left(\frac{\sigma'}{\sigma}\right)^2 \left[exp\left[-2(d/\sqrt{2}\sigma)^2\right]/erfc(d/\sqrt{2}\sigma\right] \qquad (2.43)$$

The mean area of the contact spot can be easily calculated from the mean number of the contact port per unit length of the profile:

$$\bar{a} = (A_c/A_n)^2\frac{g}{n_x n_y} \qquad (2.44)$$

While g is the contact spot shape factor and the normal distribution of the profile slope, it is equal to:

$$\bar{a} = \frac{4\pi^2 g(A_c/A_n)^2}{\frac{\sigma'_x\sigma'_y}{\sigma_x^2}\exp\,(-d^2/\sigma_x^2)} \qquad (2.45)$$

For the circular contact spots the mean radius of the contact spot $r_c(d)$ is described by the expression [15]:

$$r_c(d) = \sqrt{\frac{8}{\pi}}\left(\frac{\sigma'}{\sigma}\right)\exp\,[(d/\sqrt{2}\sigma)^2]erfc(d/\sqrt{2}\sigma) \tag{2.46}$$

From the knowledge gained about the mean number of contact spots it is possible to calculate the mean distance between them using eq. (2.15) which for the normal distribution takes the following form:

$$s = 2\pi\sqrt{g(A_n/A_c)\exp\,(d^2/\sigma_x^2)}\,\frac{\sigma_x}{\sqrt{\sigma_x'\sigma_y'}} \tag{2.47}$$

Sometimes other parameters or connections such as: summit density, the variance of surface heights or the radius of curvature of the summits are used in the statistical description of the surface structure.

2.4 Fractal Characterisation of Solid Surface

It is generally stated that rough surfaces should be characterised in a way that retains the structural information of roughness at all scales. There are cases in engineering when the roughness in all optical aberrations appears quite comparable in composition. Hence, the multiscale nature of surface roughness in above examples should be somehow quantified. For this, the fractal technique is used.

A surface consists of a large amount of roughness distance scales superimposed on each other. The roughness of the surface, as mentioned above, is generally determined by the standard deviation of surface height. It is known however, that the surface height variances, their derivatives and other rawness parameters are highly dependent on the accuracy of the measuring equipment, and therefore, for an analysed surface they are not exceptional features. The statistical self-affinity can be defined by fractal geometry because the shape of the image is similar under various magnifications. The fractal method can characterise surface roughness through scale-independent parameters and gives data on the composition of roughness in all scales of the distance which show a fractal pattern. Surface features can be anticipated within fractal systems in all size scales by the measure at a single scanning distance [16] [17] [18].

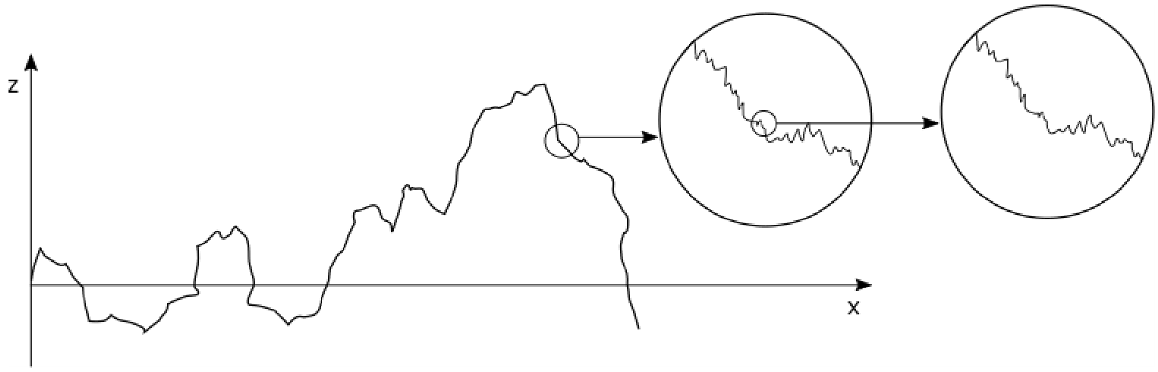

Figure 2.7. Self-affinity of the surface profile with a different magnification level

A self-affine fractal surface's Structure Function obey a Power Law and can be expressed as [19]:

$$S(\tau) = C^{*}\eta^{(2D-3)}\tau^{(4-2D)} \tag{2.48}$$

$$P(\omega) = \frac{c_1\eta^{(2D-3)}}{\omega^{(5-2D)}} \tag{2.49}$$

and

$$c_1 = \frac{\Gamma(5-2D)\sin\,[\pi(2-D)]}{2\pi}C \tag{2.50}$$

Fractal analysis enables two parameters D and C to describe surface roughness, which are tool-independent and special for each surface.

Parameter D (varying from 1 to 2 for a surface profile) refers mainly to the comparative strength of frequency components, and C to the amplitude for all frequencies, when η is the sampling device's horizontal range, τ is the incremental magnitude (range), and ω is the roughness rate. The roughness is decreased over all frequencies for the decreased numbers of D (C = constant). When C drops (with D = constant), the profile is smoother, indicating the predominance of the low-frequency element [19].

2.5 Chapter Summary

In conclusion, the above chapters served as an important introduction to the theory of solid surface. Three main ways of describing the solid surface layer were distinguished, the basic parameters that characterise them, and general rules prevailing in their interpretation were presented.

It is generally known that in the case of the mutual interaction of two solid bodies, an elastic, plastic or elasto-plastic deformation of asperities occurs [20]. A significant factor implicating the type of deformation is the contact pressure and the temperature gradient between objects. On them will be founded the correlation which will be established at a later stage. However, due to the specificity of contacts analysed in this dissertation, the entire theory of deformation and mechanical features will be omitted. It is caused, due to the inability to characterise behaviour each of the contacts separately and the lack of space for such huge part of theory, hence the existence of deformation part will be only mentioned with this entry and briefly in the Chapter 3.

Moreover, the mutual contact of the surfaces in the thermomechanical analysis of the low-pressure turbine components is rather treated as steady rather than sliding, in which the so-called “frictionally excited thermoelastic instability phenomenon” may occur [21]. In fact, in the aircraft engines come to small axial or radial part shifts in discussed regions, which are tried to block, depending on the type of connection, by various solutions.

Chapter 3: Heat Transfer Between Two Solids and Interstitial Medium

Mutual contacts between machine components in aviation engineering systems are inescapable. Because of the intrinsic roughness of the constructed materials, caused by manufacturing processes, the heat transfer between the cooperating components is influenced considerably. The accurate quantification of energy transport across interfaces is a critical aspect in the thermal analysis and design of engine components.

The thermal contact conductance (TCC) being the reciprocal of the thermal contact resistance (TCR) between interfaces must be known a priori for precise aerothermal predictions of computational fluid dynamic and heat transfer (CFD / CHT / FEM) models. For two predominant reasons, the majority of the existing TCC models are limitedly applicable:

a) they are based on over-simplifying assumptions of surface peak dimensions and character of their distribution on the surface, which do not take into account their impact on the TCC,
b) in order to calculate the thermal contact conductance, surface topography inputs are required as entry information however, they are not usually available and if, not consistent with standard industry surface data.

Due to the huge amount of information brought by the subject and the number of correlations developed in an analytical and experimental way, the author limited himself to presenting only the most important examples. The scope of the topic extends from the macroscopic to microscopic scale, which additionally causes a growth of the complexity and difficulties in unequivocal definition of appropriate correlations.

First, basing on available literature sources, representative models of TCC determination were discussed. Afterwards, approaches used in TCR modelling were presented with simultaneous discussion of the similarities and scopes of applicability of those correlations. The last part of this chapter was devoted to topics that due to their importance could not be omitted, i.e. vibrations in the issue of thermal contact conductance, the impact of bolt and rivet joints — widely used in aviation — on the temperature distribution in the contact interface and the hysteresis effect.

3.1 General Characteristic of Heat Transfer Mechanisms

The primary mechanisms of the heat transport at the interface of two metallic objects is the conduction that takes place between contact spots. In those parts where asperities are not in contact, thermal energy is mostly transmitted by conduction or radiation through the interspersed gas/fluid pockets.

The mean distance between the surfaces is usually several dozen micrometres high, hence, the Grashof number estimation derived from the effective length of the mesoscale air pockets at the interface is very small ($\sim 10^{-5}$). The latter implies that energy transfer through air pockets by convection can be seen as marginal. However, convection cannot be totally omitted in case when solids are weak conductors or interface mediums are good heat transmitters. Mechanisms of heat transport through air gaps, such as conduction and radiation, depends on the total temperature of the interface and thermophysical properties of the objects in contact.

The quantity that determines the intensity of the heat transfer is the thermal contact conductance, and its definition, for two surfaces being in contact, is expressed as follows:

$$h = \frac{\dot{Q}}{A \Delta T} \tag{3.1}$$

where: $\dot{Q}$ denotes the rate of heat transfer through the interface, A is the apparent or nominal area of contact and ΔT is the temperature drop across the contact interface.

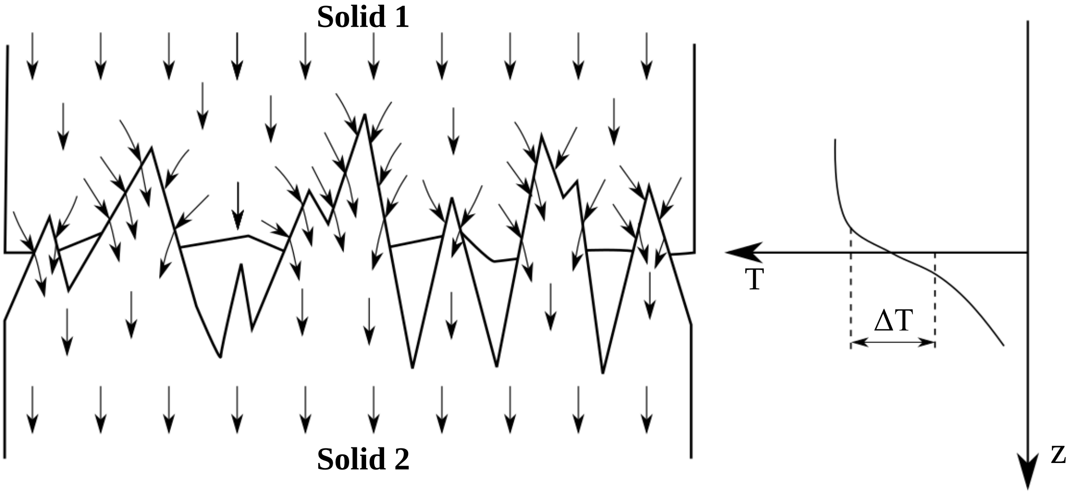

Fig. 3.1. Schematic of the microscale of solid-solid contact showing the constriction of the heat flux as it passes through the interface and the temperature drop profile at the interface

The reciprocal of the thermal contact conductance is defined as thermal contact resistance [22]:

$$R = \frac{A\Delta T}{\dot{Q}} \tag{3.2}$$

The TCR is a function of the mechanical and geometric parameters of the system as well as the time. Therefore, the values of this parameter change respectively with the load cycle and when the surface roughness, contact pressure, materials of the objects in contact, or the media between them are modified.

If one is able to determine the total heat flow through solid spots and through the medium between bodies separately then the following equation can be written:

$$\dot{Q} = \dot{Q}_S + \dot{Q}_G \tag{3.3}$$

This is when the resistance for solid spots will be expressed by the formula:

$$R_S = \frac{A\Delta T}{\dot{Q}_S} \tag{3.4}$$

and for the gas gap as:

$$R_G = \frac{A\Delta T}{\dot{Q}_G} \tag{3.5}$$

Their total value will give also the total resistance:

$$R = R_S + R_G \tag{3.6}$$

The purpose of this breakdown is caused due to the fact of its easier and more convenient to examine each of the resistances of a system separately.

If the thermal conductivity of the contacting bodies is low, the TCR is very weak compared to the intrinsic thermal resistance of the bodies. When the thermal properties of the contacting bodies are high the role of the TCR in the heat transfer mechanisms becomes very important [23] [24] [25] [26] [27].

In recent years, various commercial software required from user to supply correlations with a R or h value, with the possibility in some cases to set h as a function of time for a given set of process conditions. For most researchers in this area information about the TCR mechanisms on liquid-solid and visco-solid interfaces has become a significant concern. Due to the fact that TCR is affected by the topographical, mechanical and thermal elementary features, it is necessary to develop a quantitative understanding of the all mechanisms affecting thermal characteristics of the TCR.

3.2 TCR/TCC Calculation Models

The TCC in general is determined by the actual contact area at the interface through which the heat is primarily flowing in two assembled surfaces. Under the strains influenced by the external loads i.e. pressure fields, asperities penetrate and deform creating contact points. The area of contact spots and the topography of the deformed common surface interface affects the propagation of heat transfer through the system. Additionally, temperature variations at the interface influence also the material properties of the objects hence the issue becomes strongly non-linear, as shown in figure 3.2.

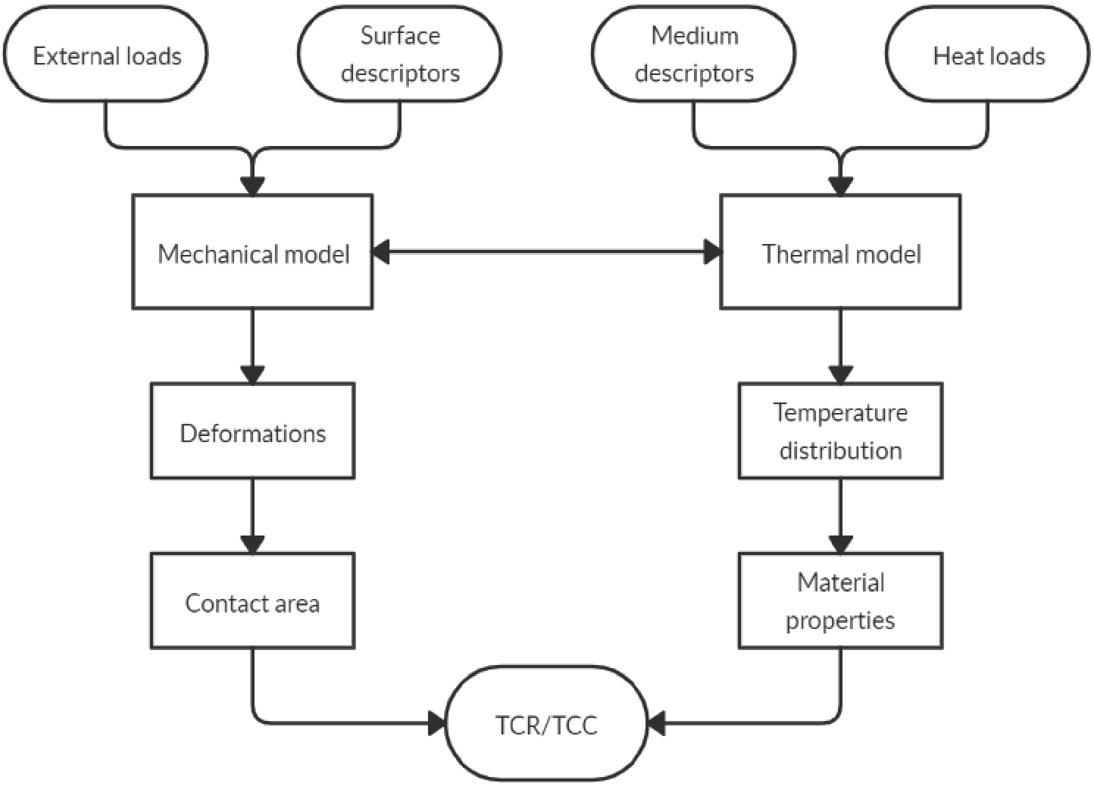

Fig. 3.2. Diagram of the elements involved in thermal contact resistance / conductance estimation

Over the last few decades several scientific studies between various types of interfaces have been carried out to expound the possible factors that influence TCC [28] [29] [30] [31]. Reseachers proposed several correlations for the TCC evaluation. Generally, those approaches can be split depending on the type of model under consideration, i.e. mechanical or thermal. For a mechanical issue, the two main approaches are:

- single-contact model and
- multi-contact model.

Literature sources sometimes distinguish the third type — fractal model — but in most cases it is considered together with the multi-contact models [32]. Concerning the thermal boundary resistance and the manner in which energy is transferred between surfaces at atomic level, there are two other approaches that can be distinguished:

- acoustic mismatch model (AMM), and
- diffusive mismatch model (DMM).

In the next chapters the assumptions of the above models and a few of the most important TCC-related studies according to the author are discussed in detail. One of them, called the Single-Contact Model, will be the foundation of subsequent numerical analysis.

3.2.1 Single-Contact Model

The Single-Contact Model, also known as Holm Tube Model [32] focuses on the fundamental assumption that each pair of touching asperities within an interface behave independently and identically. The deformation mechanics and constriction of heat flow occurs when one pair is assumed to hold no influence on neighbouring pairs, which are in contact. As a result, the thermal and mechanical models used in this approach are developed upon the analysis of a single and idealised point of contact. To get a result for thermal analysis, surface asperities are calculated by using simple geometric forms, such as circles, cones, cubes and parabolas. The representative contact is understood as the interaction formed by two distinct asperity products touching at the plane of symmetry. Each contact spot retrieves heat from a non-existent chamber, which is referred to as a flux tube or lead [32]. And so, the interface of the contact is similar to a collection of independent and parallel flux tubes, each having its own contact spot at the centre. When using the flux tube model, the tightening of the heat flow at the contact point intensifies heat resistance. The analysis for a single spot may be also extended at the interface using the electrical network analogy, where the thermal contact resistance can be expressed as the sum of parallel resistances of all contact points. It is often recognised that asperities do not cause friction and are subjected only to regular loads. Using the deformation model, half of the hemisphere’s surface and the average load can be calculated. To work out the real contact surface area and determine its association with the applied load, the mechanical behaviour of the contact is typically extended out to the whole interface.

Greenwood [30] [33] published one of the first key studies, in which the TCR was found as the measure of the sum of parallel resistances of all contact spots. He presented the method of finding the total thermal resistance of a microcontacts cluster which was determined as the sum of parallel microcontact resistances. The conductance network approach was used also by Cooper et al [34] to develop a model in order to predict the TCC correlation of different metal-metal interfaces in vacuum conditions. The measured interface pressure was found to be very sensitive to variations of the interface geometry and the surface temperature distribution. Dimensionless conductance and heat flux presented very accurate correlation, oppositely to relation of dimensionless conductance and pressure. Authors suggested that it could be caused due to insufficient surface description details, major inconsistencies in the contact pressures and a limited knowledge of multiple macro-contacts conductance. The experimental findings of this analysis were also compared to conductance data and models reported previously. The theoretical model of Cooper et al. [34], laid the groundwork for several researchers who followed the proposed thermal model, considering specific TCR models whilst also looking into various hypotheses of asperity deformation and methods of surface characterisation [35] [36] [37] [38].

3.2.2 Multi-Contact Model

The extension of the thermal and mechanical behaviour of representative contact of single-contact models to multiple interface contacts is based on the assumption that contact points on the interface are spread uniformly. In regards to real interfaces, the patterns of asperities that are in contact can cause the random distribution of contact points, without exact correlation, creating a variance in microcontacts clustering. This lends itself to the heat flow distribution held in the interface and which is marginally affected by the corresponding location of neighbouring and contacting asperities. A more accurate representation of the thermal and mechanical interactions across interfaces is only possible if the multiple asperities of the rough surfaces are brought simultaneously in contact. The TCC is computed using the temperature and heat flux distributions obtained from thermal transport simulations through the deformed interface geometry. Over the last decade two- and three-dimensional multi-contact models have been developed with advancement in both numerical methods and computer technology.

As an example, can serve work done by Liu and Zhang who presented a 2D thermo-mechanical TCC model which was developed in order to study the contact of high temperatures in superalloys and composites [39]. The model minimised the rough surfaces to the equivalent surface and the asperities were approximated as a set of identical rectangles. The finite element method was used in the work, which was properly calibrated in relation to the results obtained in experimental research. Based on findings, the relationship between the actual contact surface, contact pressure and temperature was developed. Nonetheless, by not matching predictions with other datasets the predictive potential of the proposed model was not shown.

An interesting work for the case of the three-dimensional surface topography was presented also by the above author Zhang et al. [40]. The authors presented simulation in which they tried to achieve realistic distribution of surface contact spots, with utilisation of equi-peripheral grids in cylindrical coordinates. The surfaces were discretised with use of solid bars and the deformation model was assumed to be completely plastic. Subsequently, the steady-state heat conduction simulation was carried out using a network method. The expected TCC values were correlated with the variables reported in [41] and quantitatively accepted.

In the scientific literature one can find many other examples in which the authors attempted to build a reliable model determining TCR on the interface of two bodies. However, the biggest problem that continuously occurs is precise description of the surface along with the definition of accompanying boundary conditions i.e. pressure load, that need to be considered in order to compute heat transport with the large degree of accuracy. Unfortunately, the matter is not only limited to how many spots will be in contact with each other or how their distribution and deformation model will behave. The next issue to consider is the thermal transfer process at the contact point interface, which will be discussed in more detail in the following two sub-chapters.

3.2.3 Acoustic Mismatch Model

Kapitza reported in 1941 a paper on the thermal boundary resistance topic concerning a heat flow through the common boundary of a liquid helium and copper [42]. Author observed that between media at their interface temperature drop that met the following equation occurred:

$$q = \sigma_K (T_1 - T_2) \tag{3.7}$$

where: q is the heat flux, σ_K denotes Kapitza conductance and T is the temperature of medium.

Thermal boundary resistance, also known as Kapitza resistance, differs from the macro-constriction resistance because it may exist even at atomically perfect surface interfaces. This behaviour is induced by variations in vibrational properties of materials as the energy carrier (phonon or electron) scatters in the common surface interface, when it tries to travel from one body to another. Existence of the Kapitza resistance however has a limited impact on the overall thermal resistance of the macroscopic structures hence it is often omitted. Nevertheless, its importance is increasing for nanostructured heat transfer, in which it plays a dominant role.

One of the two theories describing heat transfer through the smooth interface of two bodies is the acoustic mismatch model (AMM) formulated by I. M. Khalatnikov [43]. The theory is based on the fact that heat transfer in solids occurs through propagation of elastic waves of two types:

- longitudinal acoustic waves (LA), and
- transverse acoustic waves (TA).

The general picture of reflection and refraction of a longitudinal wave is shown in figure 3.3. It can be seen that while the longitudinal and transverse acoustic waves are scattered (and refracted), one longitudinal and one transverse wave are formed. This contributes to temperature changes between media and a lack of thermal equilibrium at the interface

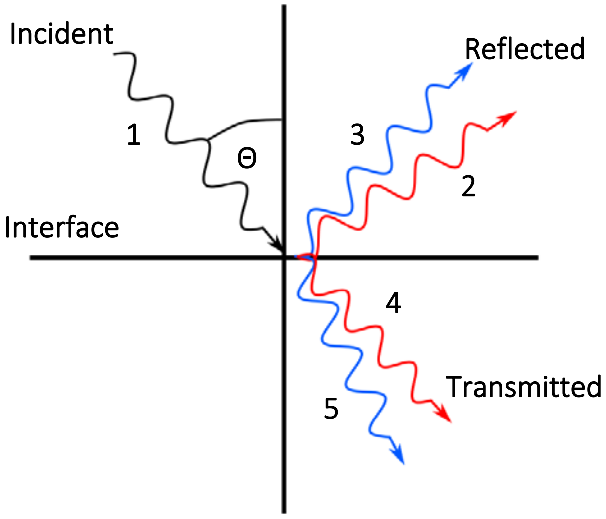

Fig. 3.3. Specular wave transfer scheme through the interface of two bodies, where: Θ is the incident angle, 1 is the incident wave, 2 the reflected longitudinal wave, 3 is the reflected shear wave, 4 the refracted longitudinal wave and 5 the refracted transverse wave

In general, the very often met in the literature statement that AMM works well below 30K for smooth surfaces is not entirely true for nanostructures. It results directly from the nano-surface roughness value which is of tens of nanometres (much smaller than the macro-scale) and by fact that, the frequency of elastic waves is limited by the maximum value obtained from the dispersion relations. A thorough study reveals that these two conditions guarantee a fairly large ratio of the elastic wavelength to the average roughness up to the temperatures of the order 1000 K [44].

Complete calculation procedure of the total energy that propagates through the interface, determination of the net heat flux through the interface, and computation of the Kapitza resistance using the acoustic mismatch model was presented in [44].

3.2.4 Diffusive Mismatch Model

Second of the two theories describing heat transfer through the rough interface contact is the diffusive mismatch model (DMM) formulated by Swartz and Pohl [45]. The main assumption of this model is that the heat energy is transferred through the phonons (massless elements). It assumes that phonons lose their memory after reaching the interface and that the probability of transmission to either side of the interface depends on the ratio of the density of phonon states. Certain phonons are distributed through the interface and some are back-dispersed, moreover they can propagate in random directions circling the hemispheres, as shown in the diagram 3.4:

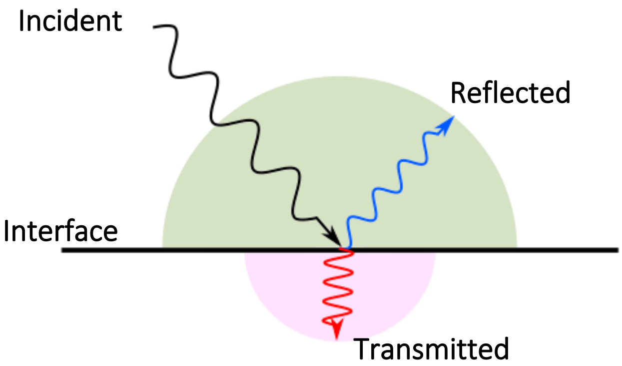

Fig. 3.4. Diffusive phonons transfer scheme through the interface of two bodies

The authors [45] unfortunately did not describe exactly all aspects and information of the method, including the physical mechanism of the process of phonons passing through the interface of two bodies. The transition layer, although its presence is tacitly presumed, in fact neglected. Attempts to solve the problem were undertaken by the authors of paper [46] who proposed a reasonable model briefly described below. The authors assumed that phonons can include some variation of the frequency and the wave function in the transition layer which allows for diffusion in the interface from the two sides of the interface. The concept of presence of transverse and longitudinal phonon was omitted, which gave a similarity and good theoretical alignment to the model presented by DMM original authors. In addition, the phonon velocity in their model had a certain average value, and by the additional use of the Monte Carlo numerical method it was possible to analyse the phonon diffusion at a transient layer. However, there is still an open question: how to define phonons transportation to other media from the common interface.

AMM and DMM models assume phonon-phonon relationships, i.e. for materials that are either semiconductors or insulators, materials in which heat transfer takes place mainly through phonons interactions. When one of the materials is a metal and the other is non-metal, another resistance occurs resulting from the necessity of energy transportation from the phonon to the electron in the metallic body. This phenomenon is of great importance and must be taken into account when the temperatures of objects in contact are equal or higher than the Debey temperature [46].

3.3 Heat Transfer in Interstitial Medium

Gaps between asperities of contacting objects can be evacuated, filled by air as well as other gases or by interstitial solid materials, which all can be used for an enhancement or a decrease of heat flow intensity.

Heat energy in is gases transported via gas molecules. Occurrence of solid boundaries influences the velocity distribution and disturbs the state of thermal equilibrium. The transfer of heat through the gas layer between two parallel plates is generally classified into four heat-flow regimes which are based on the Knudsen number [47]:

1) Free molecular
2) Transition
3) Slip
4) Continuum

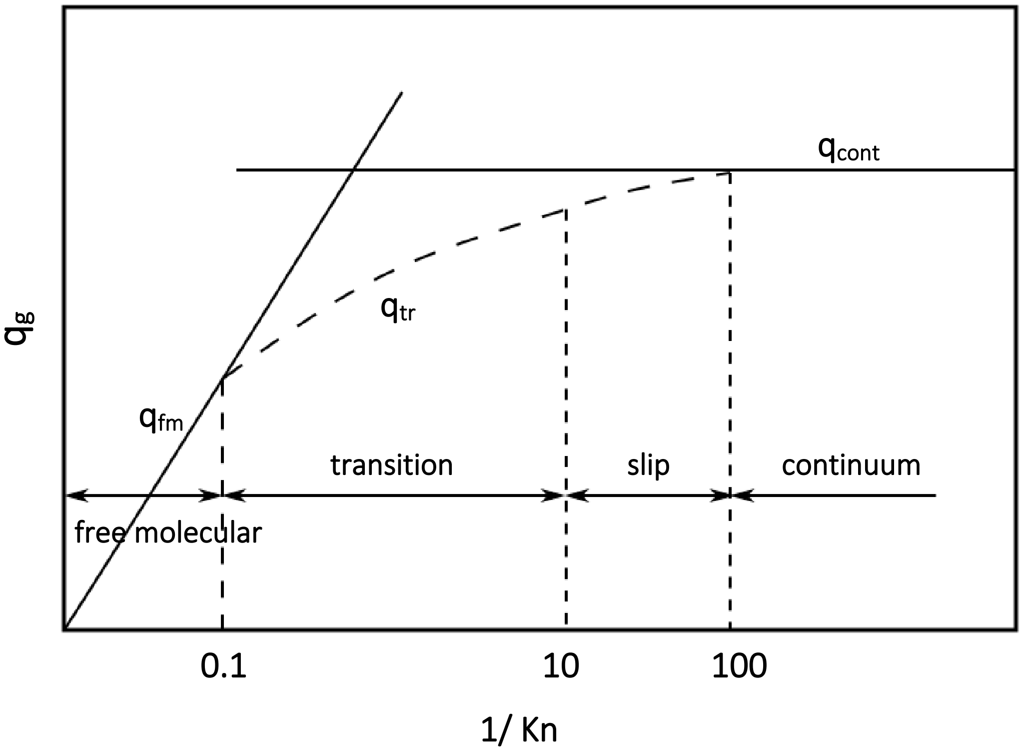

Fig. 3.5. Four heat transfer regimes as a function of inverse Knudsen number

The Knudsen number is dimensionless number defined as the ratio of the molecular mean free path length to a representative physical length scale.

In the free molecular regime ($K \geq 10$) for very low gas pressures intermolecular collisions are rare. The essential mechanism for heat transfer in this regime is the energy exchange between the gas molecules moving from the hot to the cold boundary plates. The wall effects dominate strongly the overall heat transfer which also remains independent of the gas gap width separating two objects. For insulation materials where gases are kept under very low pressure, the Knudsen number should be as high as possible to ensure low thermal conductivity.

For $0.01 \leq Kn \leq 0.1$ the heat transfer exhibits a temperature slip (temperature-jump) behaviour. The energy transfer between the gas molecules and the plate is incomplete and a discontinuity of temperature develops at the wall-gas interface. Heat transfer in the medium part of the layer where molecule velocity is not influenced by wall effects can be calculated with use of the Fourier's law of conduction.

The intermediate area between the temperature slip and the free molecular regimes ($0.1 \leq Kn \leq 10$) is called the transition region. In this state intermolecular collisions and the energy exchange between the gas molecules and the boundary walls are important.

In the fourth regime called continuum ($Kn << 1$), the heat flow depends on the gas gap thickness. Heat exchange between the solid walls is independent of the gas pressure but varies with the gas temperature. It takes place mainly though collisions of the gas molecules, and the rate of heat transfer. In this system Fourier's law of conduction is fully usable. For example airflow around an airliner in flight conditions has a low Knudsen number, keeping it squarely in the realm of continuum mechanics.

As a result of interaction of gas molecules with the boundaries of solids, some of their energy is reflected or transmitted deep into the material. It therefore differs about some value from the mean energy of the incident molecules and those being in the thermal equilibrium. In order to determine this delta, the so-called accommodation coefficient is used, which is defined as follows [46]:

$$\alpha = \frac{E_i - E_r}{E_i - E_A} \tag{3.8}$$

where: E_i is the incident energy, E_r is the reflected energy, and E_A stands for the equilibrium intensity of molecules.

The accommodation coefficient is dependent on gas temperature and composition, type of gas and material of the surface as well as on its state. The values of the accommodation coefficient are usually determined experimentally and range from 0.01 to 1.0. The physical significance of the parameter is represented by the rate at which molecules actually condense at the surface to rate of their strike at the surface.

In the field of the accommodation coefficient studies, many aspects have been investigated, examples of which are e.g. studies of:

1) Song and Yovanovich in 1987 [48] published their work done for surfaces with adsorbed layers of gases and oxides. They conducted research for different model of gases: monoatomic, diatomic and polyatomic. In their work, the correlation showed a good agreement with experimental data up to 25%. Their experimental data proved that:
    - accommodation coefficient decreases with temperature on unclean surfaces,
    - accommodation coefficient increases with temperature on clean surfaces,
    - monoatomic gases or gases with lower molecular mass have lower accommodation coefficients,
    - for rough surfaces accommodation coefficient is greater than for smooth surfaces,
    - pressure practically does not affect accommodation coefficient.

2) In Rhetner’s work [49] the thermal accommodation coefficients have been obtained for nitrogen gas colliding with various surfaces of the disk-drive air bearing using molecular beam scattering techniques. Analysis of the velocity and angular distributions of scattered species indicated that the gas was fully accommodated at the relevant surfaces for energies characteristic of room temperature gas.

3) Fan and Manson in 2008 [50] presented a calculation procedure in order to obtain accommodation coefficients values for the heavy rare gases like argon, krypton and xenon with metal surfaces. They used classical theory for atom–surface collisions that includes both direct scattering and trapping– desorption processes. Three-dimensional calculations were compared with the available data for the accommodation coefficients of rare gases at a tungsten surface. They research showed good agreement with available data.

4) Most recent research from 2020 conducted by Sonnick et al. [51] presented study for material pairs of silica and gases like helium, air, argon or carbon dioxide. Authors developed a calculation method for determining thermal accommodation coefficients from the thermal conductivity curves in combination with the pore size distribution of silica. Thermal accommodation coefficients were experimentally determined for the first time for inner pore wall-gas boundary layer of silica.

The accommodation coefficient as well as the previously mentioned models of energy transfer at the molecular level AMM and DMM are the topics that supplement the main content concerning thermal contact resistance. Because of the inability to validate numerically and experimentally their effect on particular cases considered in the dissertation, they will not be the subject discussed in later considerations.

3.4 Contact Heat Transfer Experimental Determination

To determine the TCR on a common interface of two interacting bodies, generalised analytical correlations can be used, knowing the input data beforehand the appropriate experimental study for this purpose can be conducted. The determination of temperature drops, necessary to estimate the TCR intensity may be done experimentally, either by thermocouples embedded in two specimens far from the interface [52], by using thermographic techniques [53] or metallographic methods [54].

Thermocouples application due to its simplicity and relatively low prices are the often-chosen form of the TCR measurement in comparison with other methods. Gauges of this type are placed in the tested surfaces, but due to their mass, volume and additional resistance caused by their installation in the system, it is impossible to measure the temperature of direct contact. Rather, these devices are used to measure the bulk or subsurface layer temperature than interface temperature.

Due to the distortion of the temperature distribution near the interface, surface temperature measurement may be associated with large uncertainties, hence, temperature gradients are measured at some distance from contact spots and then results are extrapolated to the interface of the contact. Their disadvantage is relatively large time constant value.

Thermographic techniques are among the other the best methods of measuring actual surface temperature. These consist of: single infrared detectors, infrared scanners or cameras with arrays of detectors [55]. A measurement can be performed by observing the contact surface directly (when actual geometry of surfaces allows to do that) or by the window of infrared transparent materials, like white sapphire, with high transmission and excellent mechanical properties. Then, by solving the inverse heat conduction problem, it is possible to determine the heat transfer coefficient. In comparison to temperatures determined at discrete points where thermocouples or pyrometers are utilised, modern infrared cameras permit to obtain an information of temperature fields of the objects. IR cameras have other advantages like:

- high thermal resolution 0.018 - 0.1 K at 30°C,
- wide measuring ranges from -40°C up to 2000°C,
- advanced systems allowing saving with high frequency,
- very good accuracy, better than 1% of the current temperature range,
- results can be saved directly on computer discs.

Infrared measurements however require the careful determination of the surface emissivity in order to properly perform the measurement. The emissivity depends on the type of material, surface conditions, temperature and IR radiation wavelengths [56].

Metallographic methods are another example that can be used in order to measure the near-surface temperature. The analysis of the microstructures and the microhardness of the worn specimens does not, however, provide exact data on the maximum temperature reached. Therefore, they are rather seldom used in the practice.

In most engineering situations, we are concerned with unstable conditions rather than with static heat flow through the two-body fluid interface. In the case of non-steady states, measurement becomes even more difficult and is burdened with larger inaccuracies. Various scholars have attempted to quantify those cases as:

- abrupt contact of solids [53],
- periodic contact of solids [57],
- solidification [58] or
- sliding movement [59].

One of the most interesting research in transient measurement field is the study presented by Beck [60], who presented non-linear estimates for both time-dependent and constant values of TCC. He performed a variety of experimental tests to determine the ideal one for his analysed case of two specimens with different temperatures brought suddenly into the contact. He introduced the criterion equation for finding a time-invariant TCC.

One of the conclusions was that the specimens should be insulated at all surfaces except the contact ones to prevent heat losses and to capture properly the phenomenon. Other stated, that the dimensionless Biot number, should be kept possibly small. If $Bi \leq 0.5$ the location of thermocouples becomes not so important, whereas if $B > 0.5$ thermocouples should be located as close as it is possible to the interface, but outside the disturbance region.

Nonlinear evaluation seems particularly interesting due to its usage for both transient and steady-state conditions. Moreover, this method has as a range of advantages over the traditional steady-state analysis:

- it does not need so many thermocouples,
- it does not require extrapolation to assess the temperature on the interface, and
- there is no disruption in the flux transfer between specimens.

Unfortunately, it is impossible to describe in this work all examples of experimental ways applied to the TCC problem. This topic is very extensive and depends on many factors influencing each other and ultimately the TCC. However, the author, on the basis of literature studies and the analysis of examples of the use of various devices, was able to formulate a list of the most common factors on which the final measurement accuracy really depends. These are:

I. Radiative heat losses of the system – occurs when lateral heat transfer is relatively high in comparison to axial direction (low thermal conductivity of specimens or low axial heat transfer due to high contact resistance – low pressure of contact, different shapes of specimens). In many cases the application of the excellent insulation or radiation shield may be not sufficient.

II. Accuracy of temperature extrapolation – the extrapolation error depends mainly on the number of thermocouples and the distance between the nearest thermocouple and the interface. This distance cannot be too small due to heat flux constriction near the interface and also not too large to properly capture the ΔT at the interface. Furthermore, increase in the number of thermocouples does not cause a proportional decrease in the error value. Usually five to six thermocouples are used by authors of studied papers. Errors often exceed 20 percent.

III. Accuracy of temperature measurement – related directly with thermocouple accuracy, and rest of system measuring devices. Manufacturers give these values and for example, the most commonly used thermocouples are of type K, and their “improved” version, type N being increasingly popular last years, for which the measuring range is -200 to 1300[°C], have the accuracy of 2.2[°C].

IV. Accuracy of thermocouple instalment – related to the positioning of the thermocouple in the sample. Very important, especially in microcontacts. The methods of drilling positioning holes are of special importance here, i.e. spark drilling method allowing preparations in metals holes of diameter smaller than 0.3 [mm] and length limited to the electrode length (several centimetres).

V. Accuracy of heat flux determination – it is examined directly in the specimens or by special heat flux meters. Knowledge about the thermal conductivity and temperature gradients is always mandatory. Heat flux-related uncertainty is limited to conductivity variability (seldom less than 3 percent), thermocouple location, and other uncertainties listed above.

Overall uncertainty with regard to the TCC experimental measurement is usually of the order of 15% for measurements carried out in the gaseous environment and less than 10% for vacuum conditions.

3.5 TCC Correlations Overview

Several methods and procedures are used in the prediction of heat transfer coefficients, those that have been described before and those that will be listed below. This chapter reviews the correlation of the various experimental studies characterising the TCC between different types of interfaces over the past few decades to shed light on all the factors which influence thermal contact conductance.

Several authors have suggested derivation ways of the TCC based on regression analysis of calculated data in an effort to include a generic equation that enables TCC estimation for engineering and design calculations. However, since these correlations are purely phenomenological in nature, they lack universality and often provide inaccurate estimates of the TCC. Broadly, these models may be classified into two previously discussed categories, namely, single-contact models and multi-contact models.

Greenwood and co-workers [33] as already mentioned in Chapter 3.2.1 presented one of the first studies in which the TCC was approximated as the sum of parallel conductance of all contact spots. This work was developed in 1966 and is considered as the origin for many other studies of the TCC models. Authors, furthermore suggested separate mechanical structures describing shape of asperities in elastic and plastic type of deformation. The mechanical reaction of a single contact was then generalised to several contacts, using a Gaussian asperity height distribution. In the Greenwood and Williamson models, all touching asperities were believed to have spherical surfaces with the same radius and to deform elastically under load according to Hertz's equations.

Cooper et. al. [34] have used a conductance network method and developed a technique for predicting the TCC of metal-vacuum-metal interfaces. Based on the 2D axisymmetric approach of steady-state heat transfer, the thermal model was built with two abutting cylindrical asperities that created a circular contact point. They believed the heights of asperity adopted a Gaussian distribution and all asperities produced plastically. Using surface statistics and the hemisphere-plane contact model, a mechanical analysis was carried out on the basis of pure geometric interaction between the equivalent rough surface and the plane, without accounting for plastically displaced material, i.e. without requiring volume conservation.

Many authors followed the thermal model provided by Cooper and co-workers suggesting alternative TCC models by considering various asperity deformation hypotheses and surface characterisation methods. The vast majority of TCC observations from analytics are focused on the Cooper et al. thermal model. The heat transfer across non-contact areas of the system is mostly ignored in their thermal analysis, and takes into account only the heat transfer across contact spots.

Mikic in his work [35] suggested TCC correlations by adding together two additional theoretical mechanical models, one for mere elastic asperity deformation and the second for plastic asperity deformation with elastic bulk content deformation.

Sridhar and Yovanovich [38] developed a TCC model using a comprehensive mechanical model for the behaviour of elastic, elastoplastic and plastic materials. TCC models have also been developed focused on a mechanical study of paraboloid and conical asperity structures instead of hemispheric shapes. All those models were based on the Gaussian distribution of asperity heights.

In the Song and Yovanovich [38] work authors proposed models for the isotropic surfaces undergoing plastic deformation. The relationship between real contact area and nominal contact area was expressed as:

$$\frac{A_r}{A_n} = \frac{P}{H_c} \tag{3.9}$$

where: A_r and A_n denote the real contact area and nominal contact area respectively, P is the nominal contact pressure at the interface and H_c is the microhardness value of the softer surface in contact. Above can be later extended to the equation [48]:

$$\frac{P}{H_c} = \left(\frac{P}{c_1(1.62\sigma'/m)^{c_2}}\right)^{\frac{1}{1+0.071c_2}} \tag{3.10}$$

where m is the absolute average asperity slope, σ' is the root-mean-squared roughness, c_1 and c_2 are experimentally determined parameters.
In the above equation A_r/A_n ratio is the primary function of nominal contact pressure and surface roughness parameters.

Even today, attempts are being made to adapt numerical models in comparison to Song and Yovanovich Eq. 3.10. As interface temperature in the previous investigations was not that high, temperature effect was not of significance.

In 2018 Donghuan et. al. performed research [25], where interface temperature was considered up to 817[K]. Authors of paper conducted a numerical and experimental study to check temperature impact on material properties and thus thermal contact resistance value. Study was performed for superalloy GH600 and C/C composite including radiation effect. Authors of work proposed their own modified version of empirical relationship 3.10 as expressed below:

$$\frac{P}{H_c} = c_o + c_1\frac{P}{E_o'} + c_2T_{int} + \left(\frac{P}{E_o'}\right)^{c_3} T_{int}^{c_4} \tag{3.11}$$

where: c_0, c_1, c_2, c_3 and c_4 are experimentally determined dimensionless parameters. Surface roughness parameters were considered in the geometry modelling of the finite element model, and the effective elastic modulus E_o' was defined as:

$$\frac{1}{E_o'} = \frac{1 - V_1^2}{E_1} + \frac{1 - V_2^2}{E_2} \tag{3.12}$$

where: E_1 and E_2 are elastic modulus of contact body 1 and 2 at room temperature respectively, and v_1 and v_2 are Poisson’s ratio respectively and average interface temperature T_{int}. They made the above equation dependent on the so-called spacing ratio, that means the ratio of width of the micro-contact asperity and neighboured peaks distance. Equation was derived as follows:

$$\frac{b}{a} = \frac{1}{c_o + c_1 \frac{P}{E_o^{'}} + c_2 T_{int} + (\frac{P}{E_o^{'}})^{c_3} \, T_{int}^{c_4}} - 1 \tag{3.13}$$

Numerical findings showed that proposed numerical method compare well with experimental results for both the spacing ratio and thermal contact resistance. That implied the presented model and the calculation method can simulate a high temperature thermal contact resistance in different conditions.

Collectively, individual models of various authors and their derived correlations are presented in Tab. 3.1.

Author	**Correlation**	**Surface model**	**Mechanical model**
Greenwood and Williamson [33]	$h = 1.91 k_e \frac{\Delta_{a,e}}{\sigma_{a,e}} (\frac{P}{H})^{0.98}$	-Gaussian distribution of heights -Identical slope for all asperities	Plastic
	$h = 1.87 k_e \frac{\Delta_{a,e}}{\sigma_{a,e}} (\frac{\sqrt{2}P}{E_e \Delta_{a,e}})^{0.98}$		Elastic
Cooper et. al. [34]	$h = 1.45 k_e \frac{\Delta_{a,e}}{\sigma_{a,e}} (\frac{P}{H})^{0.985}$	-Gaussian distribution of height -Random distribution of slopes, independent of heights	Plastic
Mikic [35]	$h = 1.13 k_e \frac{\Delta_{a,e}}{\sigma_{a,e}} (\frac{P}{H})^{0.94}$	-Gaussian distribution of heights -Random distribution of slopes, independent of heights	Plastic
	$h = 1.55 k_e \frac{\Delta_{a,e}}{\sigma_{a,e}} (\frac{\sqrt{2}P}{E_e \Delta_{a,e}})^{0.94}$		Elastic
Yovanovich [38]	$h = 1.25 k_e \frac{\Delta_{a,e}}{\sigma_{a,e}} (\frac{P}{H})^{0.95}$	-Gaussian distribution of heights -Random distribution of slopes, independent of heights	Plastic

Tab. 3.1. Thermal contact conductance analytical models representing different surface and mechanical models where: $\sigma_{a,e} = \sqrt{\sigma_{a,1}^2 + \sigma_{a,2}^2}$ and $\Delta_{a,e} = \sqrt{\Delta_{a,1}^2 + \Delta_{a,2}^2}$

In the correlations of Tab. 3.1, the exponents value of the ratio *P/H* is around 0.9. Many researchers have compared experimental measurements with the TCC predictions obtained from these correlations, for different metal-pairs and for a range of loading conditions. The correlations suggest that the relationship between the TCC and applied pressure is almost linear, whereas, the measurements showed a strong nonlinear relationship.

For a certain pressure range, which values were presented in dimensionless form, the change of dimensionless TCC value derived with above correlations has been presented in Fig. 3.6. It can be seen that for about half of the pressure value, the spread of TCC values between two extreme models of Mikic and Greenwood is almost 40[%]. This proves a large dispersion of the resulting values and the need of careful selection of the model depending on the application and the exact characteristic of the phenomenon, as the final values can drastically differ.

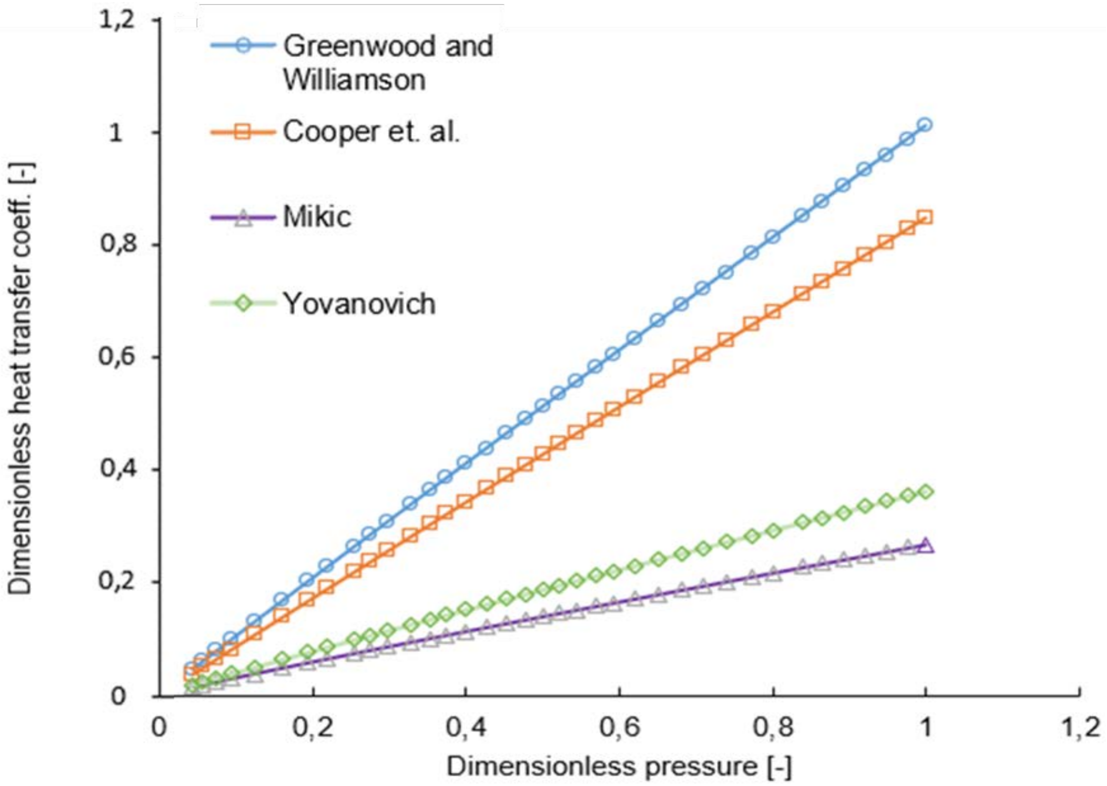

Fig. 3.6. Dependence between dimensionless heat transfer coefficient and dimensionless pressure for all plastic mechanical model correlations presented by authors from Tab. 3.1

Next conclusion which can be stated basing on equations from the Tab. 3.1 and the ways of the experiment conduction is that the magnitude of the contact conductance represents a function of numerous parameters. This includes:

- thermophysical and mechanical properties,
- characteristics of the contacting surfaces,
- presence of gaseous or nongaseous interstitial media,
- contact pressure,
- mean junction temperature and,
- conditions surrounding the junction.

Very important conclusion from all of the developed and studied correlations is that the surface parameters which affect the value of thermal contact resistance the most for a plastic flow are r.m.s. of the surface roughness *Ra* and the average slope of the asperities, whereas in pure elastic deformation only *Ra* plays an important role.

The value of the contact pressure acting on the surface is also extremely important, because it acts on the separation distance between the bodies and thus increases the actual contact surface.

The differences between the correlations visible in the 3.6 chart can be explained by the fact that each of the authors relied on his own research or the data available in the literature to match the correlations determined in analytical way with experimentally measured data. This was done for different operating conditions and contacting materials. And so, for example, for the measurement of Mikic [35] the operating temperature range was varying between 300-500[K] for stainless steel pair with air as interstitial medium. With a pressure change of about 50[MPa] and a constant temperature value, the TCC change was reported at almost 21[kW/m^{2}K], which is shown in the next Fig 3.7.

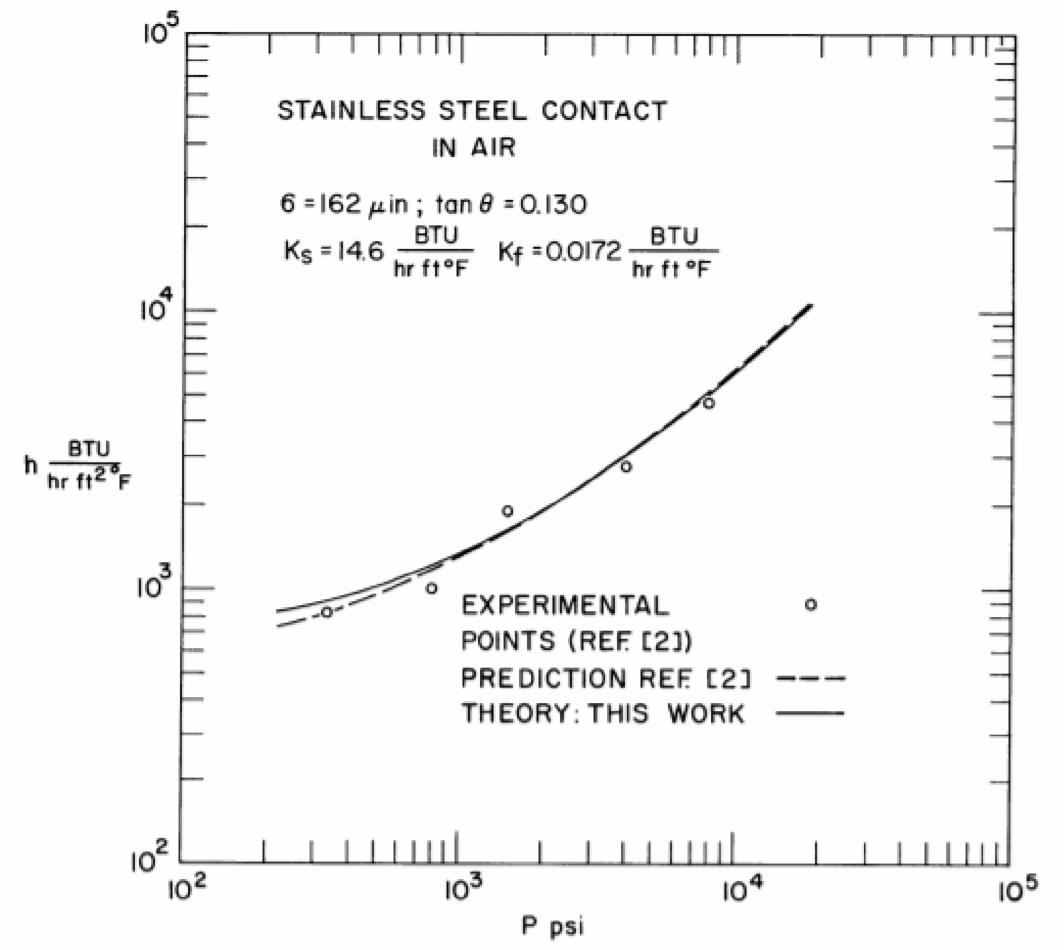

Fig. 3.7. Contact conductance vs. pressure for nominally rough flat surfaces of staniless steel in air [35]

Correlation was really effective at dealing with experimental ranges. One point, most on the right, for which the highest contact pressure was applied, appeared totally off the scale. A cause for that was sadly unexplained.

Yovanovich [38] used dimensionless values for stainless steel contact pair in the air environment. The discrepancies in the relationships are presented in detail in the table below, also distinguishing the influence of all impacting conductances, i.e. contact, gap and joint conductance.

Pressure [MPa]	2,31	5,59	10,49	27,97	55,94
$10^4\widehat{C_c}$ [-]	2,07	4,79	8,7	22,1	42,7
$10^4\widehat{C_g}$ [-]	3,71	4,05	4,35	4,98	5,63
$10^4\widehat{C_j}$ *(Theory)* [-]	5,78	8,84	13,05	27,08	48,33
$10^4\widehat{C_j}$ [-]	7,72	9,25	17,66	25,43	43,46
Difference [%]	-33,6	-4,64	-35,3	6,09	10,1

Tab. 3.2. Reconstructed table from Yovanovich's work with comparison between theory and the experiment where: $\widehat{C_c}$, $\widehat{C_g}$, $\widehat{C_j}$ are contact, gap and joint dimensionless conductance and dimensionless conductance is defined as $C = \frac{\sigma h}{k_s}$, where: σ is the effective surface roughness of two surfaces, h is the conductance and k_s is the harmonic mean conductivity.

It can be seen that there is a strong consensus between the theory and the observed values at three of the five specific contact pressures. The expected C_j values are approximately 35 percent below the observed values at the lowest and the intermediate load. The author stated that the calculated value of $C_j = 17.66 * 10^{-4}$ is uncertain since it is not compatible with the other measured values. Furthermore, in that time, it was impossible to conclude too much about the difference between the hypothesis and the test outcome, therefore the reasons for such discrepancies cannot be fully explained.

Cooper [34], in turn, in his work presented graphically the following relationship in a log-log form between his correlation and experiment results.

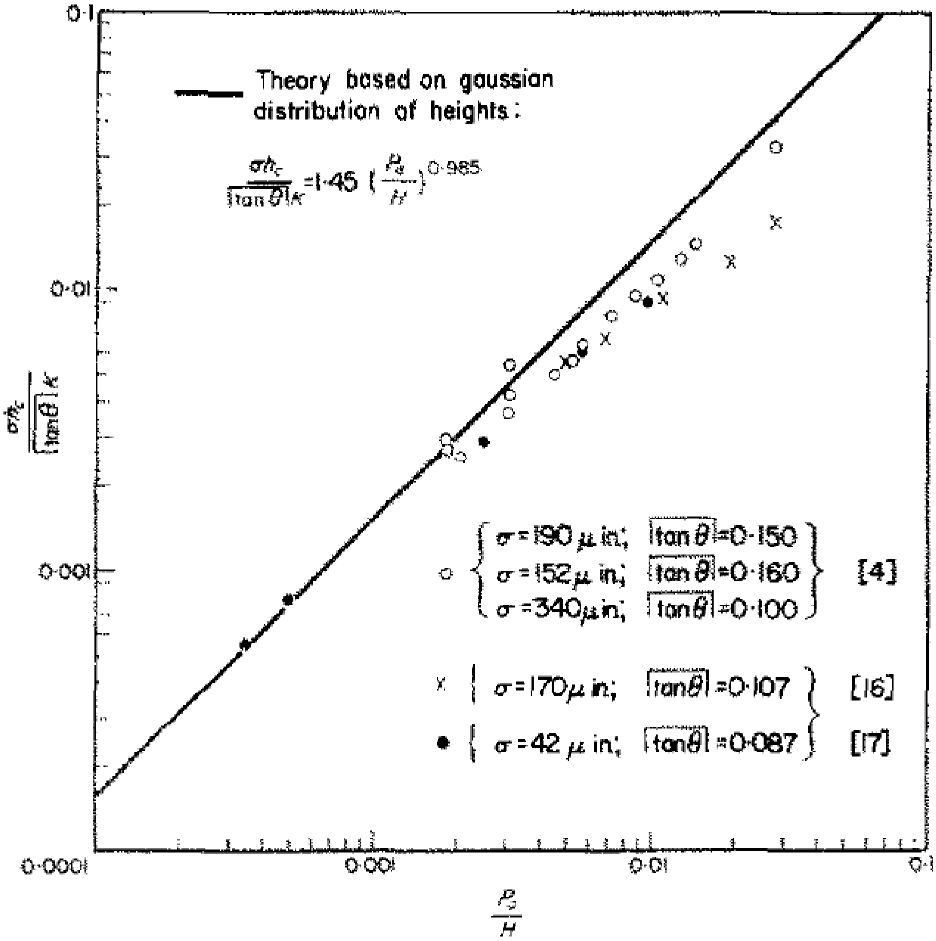

Fig. 3.8. TCC in function of. pressure for nominally flat surfaces in the vacuum [34]

After unit conversion, the contact pressure range for the two extreme measurement data ranged from about 1 to 68[MPa], causing the TCC to change by about 120[%]. It is shown that the experimental points follow the expected pattern, but fall into a band between 50 and 100[%] of the theoretical value. Cooper stated, that in view of the ambiguity related with the actual distribution of the few highest peaks that are primarily involved in the interaction of surfaces, and in view of the neglect of the potential maldistribution of contacts that minimise conduction, this effect is rational and fully explainable.

Greenwood's [33] proposed correlation was compared with existing empirical data to demonstrate quantitatively the validity of the assumptions used to develop his model. However, due to the lack of detailed information it was impossible to extract the exact range of absolute values for which the correlation is valid.

It can be clearly stated that it becomes practically impossible to determine one universal correlation for all materials of contact pairs in the vicinity of the fluid for different temperature ranges, pressures or geometric parameters. In some conditions, the correlations match the experiment very well, and in some ranges the cause of their inconsistency remains unknown. Of course, this is associated to multitude parameters and their bounded complexity affecting the thermal contact resistance as well as the way of conducting the experimental measurements. However, the authors strongly advise and point out where the attention should be particularly paid and what parameters are the decision-makers in a thorough analysis of the phenomenon. The knowledge provided by them will be used in the following part to study the phenomenon numerically.

3.6 Complementary Topics

Due to the inability to omit some topics related to above subchapters, they were briefly described here. These include the effect of vibration on thermal contact conductance, analysis of the use of rivets and screws and their effect on temperature change at the interface, hysteresis effect and its features. A very important topic from the point of view of the TCC phenomenon is utilisation of various materials and media as interstitial materials. However, this subject is too wide to be included in this dissertation, so it had to be omitted, but it should be borne in mind, that in the aviation engines exist wide spectrum of areas where applications have different lubricants or thermal barrier coatings (TBC), which also affect the value of thermal contact resistance. For more information about them, the author sends to the following papers [61] [62] [63].

3.6.1 Vibrations

Vibrations are the inseparable element of the aircraft engine in which the vast majority of components are prone to oscillations. They are related to architecture, mounting, structural features of the engine as well as its operating processes and entire machinery like fuel supply system pulsations or pumps rotations. Other excitation sources include weather conditions, environmental features and atmospheric turbulences. Therefore, various solutions of damping structural vibrations are utilised to prevent their negative impact and resonance effect occurring [64] [65] [66].

During literature studies, no correlation which includes the impact of vibration on thermal contact resistance has been found. Probably it is due to the complexity of their character and non-one-dimensionality features. Undoubtedly, it is challenging and highly complicated to generalise the type of vibration (torsional, bending). Moreover, application of a universal and at the same time accurate factor that would allow implementation of vibrations effect with appropriate frequency and amplitude range is just impossible.

Due to the fact that vibrations have a direct impact on pressure fluctuations, they also change the characteristics of thermal contact resistance. Therefore, it is necessary to estimate the thermal contact resistance value in terms of vibrations among other parameters in order to determine the overall heat transfer reliably in aircraft engine parts. Numerical methods may come with a rescue but because of the limitations of the experimental data availability it would be impossible to validate properly obtained numerical results. Vibrations influence is only briefly mentioned in this paragraph and will not be a part of the simulations later. However, their impact should be the essential aspect to investigate in future works.

3.6.2 Bolted and Riveted Joints

One of the most widely used connections in aviation engineering are bolted and riveted joints. They are produced i.e. from cadmium- or zinc-plated corrosion resistant steels, un-plated corrosions resistant steels or aluminium alloys. Most bolts used in aircraft structures are of general purpose. Aircraft manufacturers produce in certain situations bolts of different sizes with higher durability compared to standard forms. Such bolts are made for a particular application, and it is of extreme importance to use identical bolts in replacement. Special bolts are usually identified by the letter “S” stamped on the head.

Regarding rivets materials they must be enough tough and ductile. They are usually made of steel (low carbon steel or nickel steel), brass, aluminium or copper. However, when strength and a fluid tight joint is the main consideration, then the steel rivets are used. When central bolt connects two flat plates to each other the slab contact region is reduced to a very tiny annulus around the bolt hole [67]. The figure 3.9 schematically shows the bolted connection of two flat plates, where: α denotes the cone dispersion angle, a – near edge of the bolt, c – actual contact region radius, b – bolt head width, z – plate thickness, σ_z - axial stress.

Various experiments and theoretical considerations confirmed that the axial stress distribution decreases from a maximum near the edge of the bolt hole to nearly zero within a short radial distance. Therefore, in order to estimate thermal contact conductance value first the stress distribution at the interface of the joint must be determined. This allow, in turn, to compute the length of the joint contact area which has an essential impact on TCC.

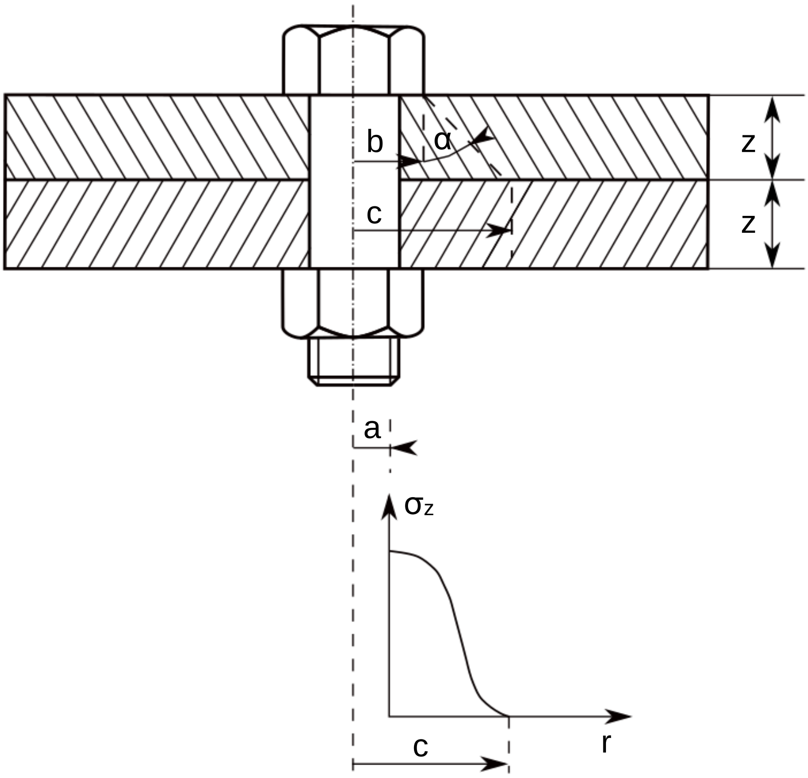

Fig. 3.9. Scheme of bolted joint with stress distribution along the connection

On the next figure 3.10 the pressure and isotherm distribution in a bolted connection was presented. Intuitively, it can be concluded that the total resistance of the axial heat flow through a bolted joint can be considered in two scales:

1) macroscale - caused by the constraint and distribution of the heat flow lines across the contact area, and
2) microscale - defined for each contact spot within the actual contact area.

Basing on above, the total joint resistance for the axial heat flow through the bolted joint can be defined as follows:

$$R_{total} = R_{macro} + R_{micro} \tag{3.14}$$

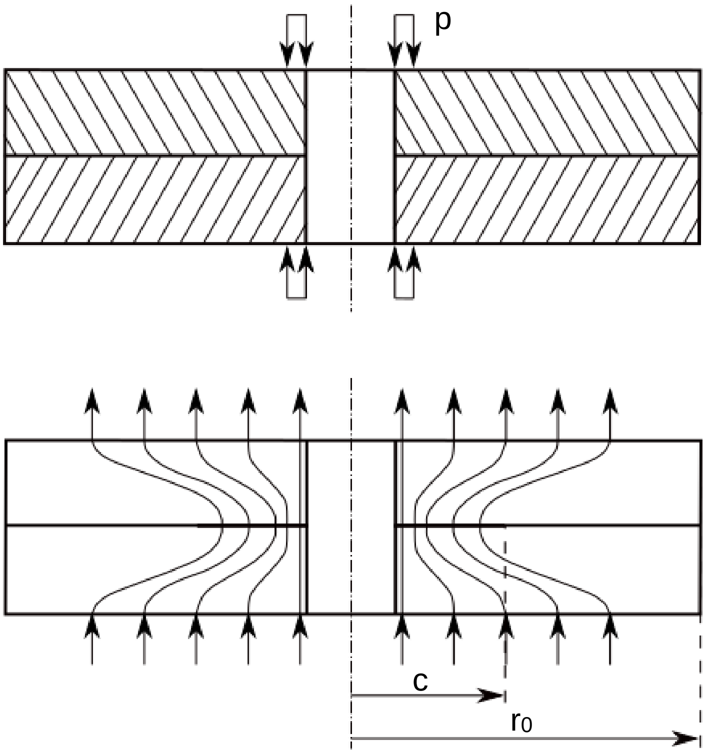

Fig. 3.10. Pressure and heat distribution along the bolted joint

Studies reported that the microscopic resistance depends strongly on the interface pressure distribution within the actual contact area [67]. In addition, the microscopic resistance decreases with the extent of the contact zone, defined by the contact region radius. Because of that it is apparent that radius and its component are the most important parameters determining the TCR for a particular pair of surfaces. The macroscopic resistance may be determined using a finite difference technique or simulated experimentally i.e. using electrolytic tank analogue [68].

The 3.8 and 3.9 diagrams show results obtained from the finite difference analysis, where: k is the ratio of the conductivity of the fluid in the gap to the conductivity of the material of the plates, and the macroscopic resistance $\hat{R}$ is nondimensionalized:

$$\hat{R} = (R - R_S)/R_S \tag{3.15}$$

where: R is the total resistance with the macroscopic constriction and R_S denotes total resistance without the constriction; i.e., the resistance of a hollow cylinder with inner radius r_a, outer radius r_c and the height equal to double plate thickness.

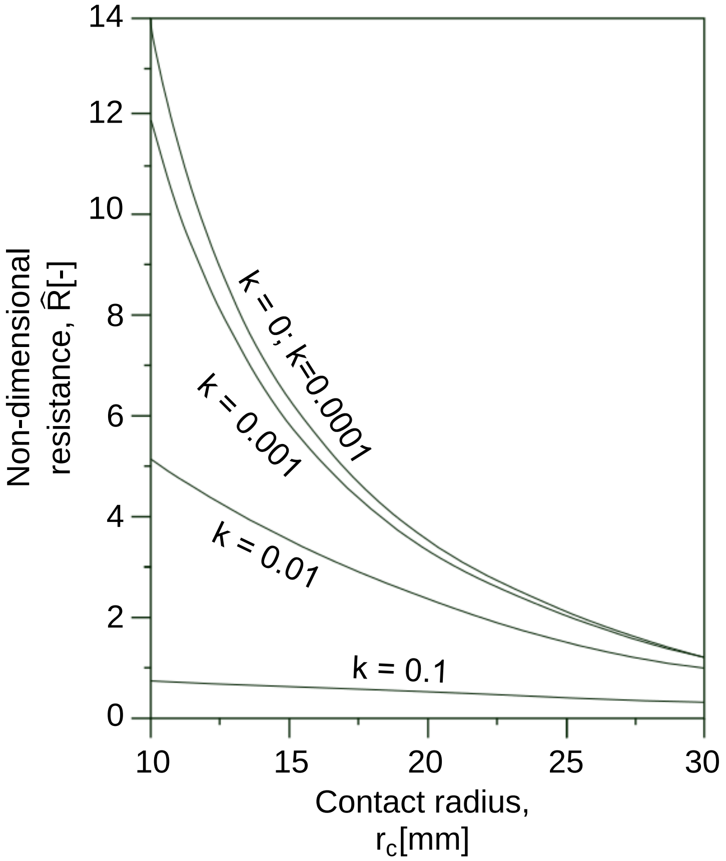

Fig. 3.11. Bolted joint in conducting medium (r_a = 5, r_o = 50, z=12.5). Reconstructed from [11]

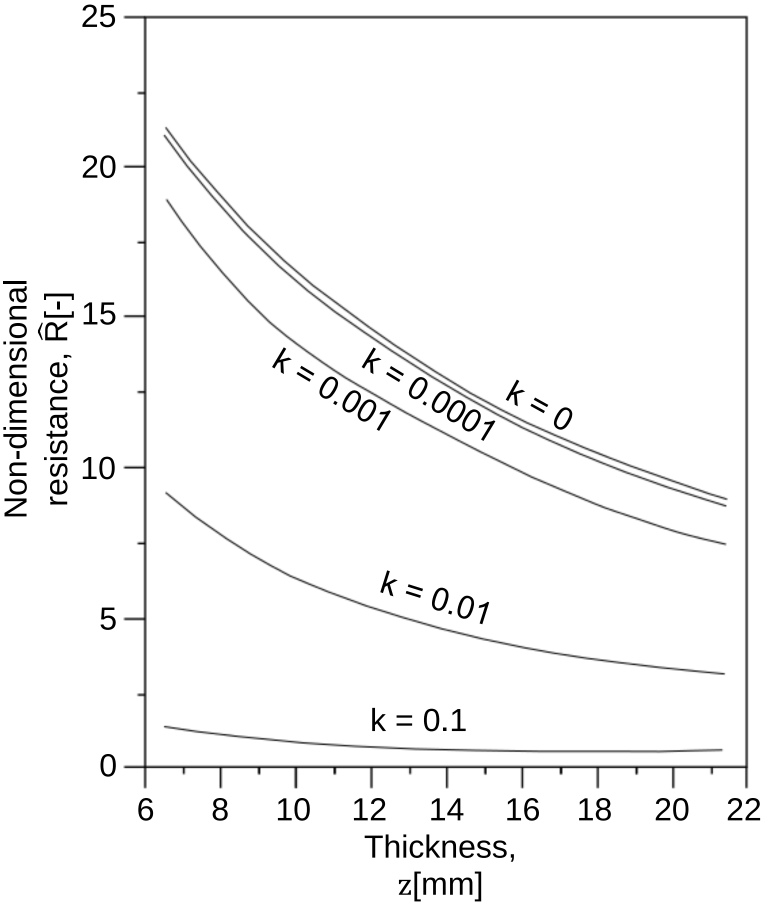

Fig. 3.12. Bolted joint in conducting medium ($r_a = 5$ $r_c = 10$ $r_o = 50$). Reconstructed from [11]

Analysis confirmed that the macroscopic resistance decreases with increase in both the thickness and the contact zone radius which however are not independent in practice. In addition, it is shown that the resistance for $k \leq 0.0001$ is virtually identical to $k = 0$ (vaccum conditions).

At work of Yeh et al. [69] mathematical correlations for the pressure and TCC relation were presented, depending on bolt torque and their number. Their derived equations are defined as follows:

- Four bolts:

$$P = 1.40 + 1.02\tau^{0.28}$$
$$h = 3.89 + 0.29\tau^{1.24} \tag{3.16}$$

- Eight Bolts:

$$P = 1.94 + 0.707\tau^{0.59}$$
$$h = 12.67 + 0.45\tau^{2.01} \tag{3.17}$$

where: pressure P is expressed in [*MPa]*, conductance h in [*kW/(*m^2*K)]* and the torque τ in [*Nm]*.

3.6.3 Hysteresis Effect

It was noticed that during a gradual loading of a joint and afterwards unloading it, the thermal contact conductance values become larger during in the latter case. Various studies in the last decades have proven the existence of this effect, hereinafter referred to as the hysteresis effect. From the conclusions drawn from the carried-out experiments, it was found that this effect occurs much more often in the case of rough surfaces than in the smooth ones. In addition, it has been noticed that the number of joint loads under same pressure values does not affect heat conduction so much in subsequent stages [70]. The studies have also shown that the number of contacts during unloading is considerably higher. Explanations of this phenomenon should be sought in the change of the actual contact surface of asperities in subsequent loadings.

Bradley's theoretical analysis [71] suggested that the surface asperities were plastically deformed during first loading. Then plastically deformed joints recover elastically to some level which led to bigger radii of the individual contact tips and thus a higher real contact area than before loading.

Plastically deformed joints recover elastically to a certain degree, resulting in change of exposure of contact tips and their dimensions. Thus, greater real contact areas can be observed after successive loadings than before first one. It was found that for the Gaussian distribution of asperity heights following statements can be wrote [71]:

a) The actual contact area is proportional to the pressure during initial loading.
b) If one slightly reduces pressure value ($0.5 < p/p_{max} < 1$) the contact area will decrease in proportion to the pressure by $p^{2/3}$

Li et al. work abound with interesting conclusions [72]. As a result, increased load cycles number produces higher contact conductivity values, however the cyclic load cannot endlessly boost the intensity of the contact conductivity. It has been found that the number of around thirty load cycles is sufficient to obtain maximum profits from repeated loading. An additional TCC increase can be achieved through a number of load cycles that exceeds the normal operating pressure. The overloading process could increase the thermal contact conductance by up to 51%.

Above conclusions regarding hysteresis effect can be used to enhance the thermal conductance in practice. To do that, the contact joint should be preloaded beyond the maximum operating conditions. Afterwards, while unloading and reloading the contact conductance value increase will occur and it will be higher than the value that which would be expected if the contact was not preloaded. Then, when reducing the load and increasing it immediately back again the heat transfer rate will peak more significantly than in the non-overloading event.

3.7 Chapter Summary

The established TCC models were analysed in this chapter, demonstrating the implications and shortcomings of the surface characterisation methods and energy transfer mechanisms between bodies being in contact with each other. A literature review of the available correlations for thermal contact resistance was performed. Additional attention was given to the heat transfer regimes that prevails in an interstitial medium. Furthermore, the topics of the TCC in bolted joints, the influence of vibration and the hysteresis effect were discussed. Finally, a few words were dedicated to the description of methods used in experimental researches, which should undoubtedly be included as an extension of the work carried out in this dissertation.

All so far discussed TCC derivation methods are burdened with significant errors, which result from underestimation or overestimation of the heat transfer coefficient. The biggest problem is the surface characteristics which have a significant impact on the value of contact resistance. However, these high-resolution surface data are seldom collected in the industry. Therefore, the topographic inputs that may be needed for estimating TCC in numerical simulations can be hard to find for models built on the basis of high-resolution surface measurements.

For doctoral dissertation purposes it was decided not to ignore such important factor as roughness thus, the topography of rough surfaces and the contact interface will be stochastically reconstructed by numerical script, basing on the commonly available surface topography descriptors. Afterwards, using the macro- and mesoscale numerical models, domain is going to be spatially resolved utilising sets of elements and nodes, allowing thermal transport across the interface to be simulated. Subsequently, the temperature and heat flux distributions will be used in order to compute the TCC as a function of asperities size, fluid flow and pressure load. Obtained data will serve to develop a TCC correlation being a key aspect of the PhD project.

In the following chapters, attention will be devoted to the theory of one of the CFD methods so-called Lattice-Boltzmann Method, which, together with the knowledge gathered so far, will be used to develop the innovative numerical simulation for the thermal contact resistance model.

Chapter 4: Lattice Boltzmann. Fundamentals of Method

4.1 Foreword

The lattice Boltzmann method is a sophisticated computational fluid dynamic approach. It is often utilized to numerically understand the incompressible, time-subordinate Navier-Stokes equation. Its value resides in the ability to easily depict complicated physical processes varying from multiphase processes to reactive chemical coactions between fluid and environment.

In LBM the fluid is represented by fractious particles net, connected and reacting together. The particles can either stream via lattice links or collide with each other at lattice sites. The entire method belongs to the explicit type. In many fields of engineering it is much easier and convenient to use LBM than the standard method of solving N-S equation i.e. in processes requiring thermodynamics integration or the study of flow through porous media. This approach is a link between the microscale and the macroscale, which does not consider the behaviour of each molecule individually, but the whole group as a unit. The whole set is represented by the particle distribution function, which is a key aspect of the method being discussed, and the scale at which this is achieved is called the mesoscale.

Author would like to demonstrate the possibilities of non-mesh techniques in numerical analysis by examining representative example with the LBM in this dissertation. The thermal contact resistance phenomena are often regarded as a kind of macro-wide simplifications with no precise micro- or mesoscale features incorporation. Further detailed analysis may permit other interesting characteristics to be captured at the roughness length level.

4.2 LBM Roots

The LBM technique is regarded as a Boltzmann equation numerical solver. It was introduced in 1988 by McNamara and Zanetti [73]. The Boltzmann equation is the analogue to the Navier-Stokes equation however it describes the space-time dynamic of a statistical quantity called probability distribution function that is defined in six-dimensional stage space at molecular level. The amounts of physical phenomena included in the model at atomic level of representation are larger than in the Navier-Stokes equation at its hydrodynamic level. It is because the Boltzmann equation is not liable to a division of time scales and can describes liquids in non-hydrodynamic routines with enormous atomic mean free paths. Besides, the sub-atomic model can catch transport phenomena features as friction or diffusion.

Lattice Boltzmann models are autonomous from the theory above and were created from so-called Cellular Automata models. The Cellular Automata is a computational model for the evolution of discrete states described by integer variables (in contrast to the floating-point representation of lattice Boltzmann values). Lattice Boltzmann models came into being when the Cellular Automata procedure was attempted to shorten and simulate the corresponding discrete Boltzmann equation's dynamics. In spite of the fact it was later discovered that the lattice Boltzmann method can be gotten straightforwardly from the continuous Boltzmann equation [74].

4.3 Fundamentals of the Method

In this section, briefly and concisely the most important aspects of the Lattice Boltzmann Method are described, starting from the fundamentals laws on which the method is based, through the equations, schemes and commonly used boundary conditions.

4.3.1 Density Distribution Function and Its Moments

The computing domain is essentially broken down into molecular velocity sets in the Lattice Boltzmann Method (LBM), hence, the degree of domain freedom rises and fluid flow can be defined, namely by the density distribution function *f*. It implies that a fluid's nature characteristic can be separated into a single equation of development. The distribution function of a fluid specifies the mass density in the so-called phase-space, at a certain point in time *t*, position *x* and its propagation speed *c*, as follows:

$$f(t,x,c) = \frac{dm(t,x,c)}{dxdydzdc_x dc_y dc_z} \tag{4.1}$$

Function *f* comprises of a specific package of molecules at a certain position in a control volume *x* distributing them at a certain velocity range [c, c+dc], because it is practically impossible to determine the probability of finding one specific speed value for a given molecule, they are in a constant movement.

Through applying moments which are basically a velocity integral of function weighted over every possible particle velocity to the distribution function, the macroscopic parameters can be established. The number of molecules in control volume must be adequate to maintain physical meaning, i.e. the average state must not be affected by particular molecules' behaviour, this is analogous to the continuum condition.

Two types of moments can be distinguished [75]:

- central moments relative to the bulk velocity *v*:

$$K_{x^l y^m z^n} = \int_c (c_x - v_x)^l \left(c_y - v_y\right)^m (c_z - v_z)^n f dc \tag{4.2}$$

- raw moments which are defined as:

$$M_{x^l y^m z^n} = \int_c c_x^l c_y^m c_z^n f dc \tag{4.3}$$

The sum of *l*, *m* and *n* designates the order of the moment. All the distribution functions are integrated over all possible velocities and weighted with *c*, which finally gives the macroscopic density ρ. Thus, the integration limits are from 0 to infinite, but for simplicity they will be not specified in below formulations. Most common moments are [76]:

- mass density, zeroth order raw moment:

$$\rho = \int_c f dc \tag{4.4}$$

- momentum density, first order raw moment:

$$\rho v = \int_c c f dc \tag{4.5}$$

- kinetic energy, second order raw moment:

$$\rho e = \frac{1}{2} \int_c c^2 f dc \tag{4.6}$$

that, according to the thermal vibration of particles, independent of the bulk velocity, is responsible for a translational transfer of the fluid plus the internal energy:

$$\rho e = \rho \left(\frac{1}{2} v^2 + e_i\right) \tag{4.7}$$

The internal energy e_i can be derived from the fluctuational part of the velocity, where *u* is the particle velocity relative to the fluid velocity, also defined as the thermal particle velocity:

$$u = c - v \tag{4.8}$$

Moreover, internal energy from the kinetic theory can be expressed as:

$$e = \frac{3}{2m} k_B T \qquad (4.9)$$

where k_B denotes Boltzmann constant ($k_B = 1.38 * 10^{-23}\, J/K$) and T is the system temperature. Equation 4.9 couples directly temperature with kinetic energy.

- the first order central moment of *f* weighted with *u* equals:

$$\int_c u f dc = \int_c c f dc - v \int_c f dc = \rho v - \rho v = 0 \qquad (4.10)$$

The above formula can mathematically imply that the thermal molecular velocity is not adding to energy, and thus the distribution of the molecular thermal velocity is basically symmetric.

- the second order central moment describes the momentum flux tensor:

$$p v_\alpha v_\beta + p\delta_{\alpha\beta} - \tau_{\alpha\beta} = \int_c c_\alpha c_\beta f dc \qquad (4.11)$$

and

- the second order central moment related to the bulk velocity *v* gives the stress tensor:

$$p\delta_{\alpha\beta} - \tau_{\alpha\beta} = \int_c (c_\alpha - v_\alpha)(c_\beta - v_\beta) f dc \qquad (4.12)$$

where: $\tau_{\alpha\beta}$ is the shear stress tensor, and $p\delta_{\alpha\beta}$ is the normal stress tensor.

4.3.2 Boltzmann Equation Towards Continuity Equation

In a moving reference system, changes of the density distribution of a fluid can physically only be caused by collision of molecules. Let collision operator Ω*(f(t, x, c))* be a general expression of a change of f between its final and initial state. The simplified version of the Boltzmann equation is as follows:

$$\frac{df}{dt} = \frac{\partial f}{\partial t} + \frac{\partial f}{\partial x_i} * \frac{\partial x_i}{\partial t} + \frac{\partial f}{\partial c_i} * \frac{\partial c_i}{\partial t} = \Omega(f) \qquad (4.13)$$

where $\frac{\partial c_i}{\partial t}$ is acceleration a and can be related to a force F by Newton's second law ($F = ma$). Hence above equation can be equivalently defined as:

$$\frac{\partial f}{\partial t} + c\nabla_x f + \frac{F}{m}\nabla_c f = \Omega(f) \qquad (4.14)$$

The first term of Eq. 4.14 is the change rate of function *f* in a certain time step. The second term is the advection of the particles and the third one denotes the external force F which depends directly on the density ρ.

The rightmost term of 4.14 equation Ω*(f)* consists of a complex integral functional of the distribution function itself, involving differential cross sections and a specific atomic model [77] [78]. The collision operator becomes zero when the control volume is in an equilibrium state.

The zeroth moment of the Boltzmann equation 4.14 for a physical system without an external source (force) term result in:

$$\int_c \left[\frac{\partial f}{\partial t} + c * \nabla_x f\right] dc = \int_c \Omega(f) dc \Rightarrow \frac{\partial}{\partial t}\int_c f dc + \int_c \nabla_x * (cf) dc = \int_c \Omega(f) dc \qquad (4.15)$$

Collision does not change the total mass of the fluid in a certain moving reference volume, therefore:

$$\frac{\partial}{\partial t}\int_c f dc + \nabla * \int_c cf dc = 0 \qquad (4.16)$$

Provided the collision of gas molecules was fully elastic, the collision term would change the total momentum neither. By applying zeroth moment on the Boltzmann equation we obtain the continuity equation:

The collision concept would not alter the total momentum neither if the interaction of gas molecules was completely elastic. As there can be seen, by applying zeroth moment on the Boltzmann equation, we obtain the continuity equation:

$$\frac{\partial}{\partial t}\rho + \nabla * (\rho v) = 0 \qquad (4.17)$$

Moreover, by applying first moment to equation 4.17 one can derive, fundamental to fluid mechanics, the Navier-Stokes equation [79].

4.3.3 General Solution of Simplified Boltzmann Equation

For a system without an external force, the Boltzmann equation 4.13 can be defined as:

$$\frac{\partial f}{\partial t} + c\nabla_x f = \Omega(f) \tag{4.18}$$

Description of the implementation of forces term LBM is presented in [80]. Let is suppose the collision term of equation 4.18 was simplified so that it depends only on the initial condition. Equation then turns into an inhomogeneous linear transport equation with constant coefficients. Its unique solution is obtained accordingly to the below formula:

$$f(t,x,c) = f(0,x-ct,c) + \int_{s=0}^{t} \Omega\left(f(s,x-c*(t-s))\right)ds \tag{4.19}$$

The integral part of equation 4.19 on the right is the description of all collision incident along the direction of traveling. Basing on the shape of the above equation, two steps may be distinguished, that are characteristic features of the LBM operation algorithm:

I. the propagation of the distribution function along its characteristic trajectory, so-called streaming step:

$$f(t,x,c) = f(0,x-ct,c) \tag{4.20}$$

II. influence of collision between molecules on change of distribution function,

$$\Delta f_{collision} = \int_{s=0}^{t} \Omega\left(f(s,x-c*(t-s))\right)ds \tag{4.21}$$

The collision integral over time reduces to a single collision event for a discrete time-stepping. In that case, the solution steps sequence can be turned around:

I. collision impact, leading to post-collision state f*:

$$f^*(t,x,c) = f(t,x,c) + \Delta f_{collision}(t,x,c) \tag{4.22}$$

II. and, the streaming step:

$$f(t+\Delta t, x+\Delta t*c, c) = f^*(t,x,c) \tag{4.23}$$

4.3.4 Equilibrium Distribution Function

The function of equilibrium distribution f^{eq} is the keystone of LBM implementation. It physically contributes on the relaxation of the distribution function in the computing domain. With a properly defined equilibrium distribution function, different physical problems can be solved. A control volume with a constant density distribution function over time represents an equilibrium state, therefore the collision operator *Ω(f)* in such state equals zero. The mathematical formulation is as follows:

$$\frac{df}{dt} = \Omega(f) \equiv 0 \tag{4.24}$$

In this situation, the analytical solution of the integrated collision function for the ideal gas leads to the Maxwell-Boltzmann equation [78]:

$$f^{eq}(\rho, c, v) = \frac{\rho}{(2\pi RT)^{\frac{3}{2}}} exp\left(-\frac{(c-v)^2}{2RT}\right) \tag{4.25}$$

where R is the universal gas constant.

The exponential term of the f^{eq} in Eq. 4.25 can be approximated with polynomials by applying an expansion of the velocity up to the second order expression. Then the velocity space can be transformed from a continuum into a discrete set of velocities with a Gauss-Hermite quadrature. Such estimate is true for low Mach numbers under 0.3, so the process will work only with soft compressions of the fluid [81].

Equation 4.25 is a representation of a scaled three-dimensional normal distribution. The root-mean-square speed outcome product of the Equation 4.25, which is directly related with the speed of sound in the gas, is also proportional to the mean thermal molecular speed u_0 [78]:

$$c_s = \sqrt{RT} = \frac{u_0}{\sqrt{3}} \Rightarrow u_0 = \sqrt{3RT} \tag{4.26}$$

where: $\bar{u}$ – speed of sound, $\bar{u}$ means thermal molecular speed.

Raw and central moments of equilibrium distribution function are defined as follows:

- Mass density, zeroth order raw moment:

$$\rho = \int_c f^{eq} dc \tag{4.27}$$

- Momentum density, first order raw moment:

$$\rho v = \int_c c f^{eq} dc \tag{4.28}$$

As can be noticed zeroth and first raw moments are the same as in Eq. 4.2 and 4.3.

The first central moment of equilibrium distribution function is also the same as in Eq. 4.10.

$$\int_c ufdc = \int_c cfdc - v\int_c fdc = \rho v - \rho v = 0 \tag{4.29}$$

The energy moment is calculated as:

$$\begin{aligned}\frac{1}{2}\int_c u^2 f^{eq} dc = \frac{1}{2}\int_c (c-v)^2 f^{eq} dc = \frac{1}{2}\int_c |c|^2 f^{eq} dc \\ +\frac{1}{2}|v|^2\int_c f^{eq} dc - \frac{1}{2}\int_c 2vc\, f^{eq} dc \\ = \rho e + \frac{1}{2}\rho|v|^2 - \rho|v|^2 = \rho e_i\end{aligned} \tag{4.30}$$

Which relates the thermal particle velocity and the temperature with the internal energy of the control volume via direct connection.

The second order central moment is developed as [82]:

$$p\delta_{\alpha\beta} = \int_c c_\alpha c_\beta f^{eq} dc \tag{4.31}$$

The latter is significant since, under the conditions of equilibrium, it clearly states, only the contribution of normal forces will be experienced by the second order moment. This can be clarified by checking Eq. 4.12, where the stress tensor does contain both normal and shear contributions. Furthermore, if the distribution functions at a given node is in harmony, this implies that the node is completely “relaxed” — it just conducts pressure.

4.3.5 Collision Models

Boltzmann formula (Eq. 4.13) is difficult to solve because of the existing collision term. It requires numerical approximation of the complex integral function which is very tricky to solve. However, interactions of two particles will not greatly affect the values of system measured quantities [83]. It allows to approximate the collision operator into the simple operator without error in the solution's result as long as a common collision operator preserves mass momentum and energy laws and with non-decreasing entropy condition. In the next sections two of most common collision models will be briefly discussed: BGK Single Relaxation Time and Multi-Relaxation Time.

4.3.5.1 BGK-SRT Model

The Bhatnagar–Gross–Krook model [84] is linear approximation of the collision operator defined as:

$$\Omega = -\omega(f - f^{eq}) = -\frac{1}{\tau}(f - f^{eq}) = -\frac{u}{l_f}(f - f^{eq}) \tag{4.32}$$

Equation 4.32 consists of: f^{eq} which is the Maxwell-Boltzmann equilibrium given in the previous section, the collision frequency ω which is the reverse of the mean collision time τ, also known as relaxation time. The time of relaxation between two molecular interactions is equivalent to their mean time and the mean free path length l_f between two collisions.

In an actual implementation, the length between two collisions is a grid property not a real mean free path. In fact, the LBM collision rate is determined from the examination of the fluid's viscous properties (Section 4.3.6). Therefore, there is a clear need of creation of a series of standardised units which relate the LBM framework, the dimensionless unit system, and the physical value system.

4.3.5.2 Discretization of BGK Boltzmann Equation

Let us substitute BGK scheme 4.41 to the Boltzmann equation 4.14. Without external forces, we obtain:

$$\frac{\partial f}{\partial t} + c\nabla f = -\frac{u_0}{l_f}(f - f^{eq}) \tag{4.33}$$

where the particle collision rate can be defined as the ratio of the mean thermal particle speed u_0 with the mean free path l_f. Next, equation 4.33 is transformed according to the Buckingham Π theorem to a characteristic, non-dimensional equation [85]. Including the variables of equation 4.33 and a characteristic macroscopic length L, it appears to us a set of nine variables: t, x, l_f, L, u_0, v, c, and f, which are defined as:

$$\hat{t} = \frac{tu_0}{L} \tag{4.34}$$

$$\hat{x} = \frac{x}{L} \tag{4.35}$$

$$Kn = \frac{l_f}{L} \tag{4.7}$$

$$Ma = \frac{v}{u_0} \tag{4.8}$$

$$\xi = \frac{c}{u_0} \tag{4.38}$$

$$\hat{f} = \frac{fu_0^3}{\rho^3} \tag{4.39}$$

Therefore, non-dimensional formulation of the BGK Boltzmann equation can be formulated as:

$$\frac{\partial \hat{f}}{\partial \hat{t}} + \xi * \nabla_{\hat{x}} \hat{f} = -\frac{1}{Kn} * \left(\hat{f} - \hat{f}^{eq}\right) = \Omega\left(\hat{f}\right) \tag{4.40}$$

Subsequently, for calculation purposes, the non-dimensional phase space and time variables are transformed into the lattice values, which comfortably transform the propagation velocity into the lattice propagation velocity, whose magnitude is unity in a uniform grid. The lattice units are defined as:

$$\bar{\bar{t}} = \frac{\hat{t}}{\Delta \hat{t}} \tag{4.41}$$

$$\bar{\bar{x}} = \frac{\hat{x}}{\Delta \hat{x}} \tag{4.42}$$

$$\bar{\bar{\xi}} = \frac{\Delta \bar{\bar{x}}}{\Delta \bar{\bar{t}}} \equiv 1 \tag{4.43}$$

Once again, phase space is discretized. The outcome are arrays of i velocity directions and with later application of a first order finite differences and a forward time step approximation to Eq. 4.33, we obtain:

$$\begin{aligned} &\frac{f_i(\vec{x}, t + \Delta t) - f_i(\vec{x}, t)}{\Delta t} + \vec{\xi}_i * \frac{f_i\left(\vec{x} + \Delta t * \vec{\xi}_i, t + \Delta t\right) - f_i(\vec{x}, t)}{\Delta t \vec{\xi}_i} \\ &= -\omega * \left(f_i(\vec{x}, t) - f_i^{eq}\right) \end{aligned} \tag{4.44}$$

Knowing that the propagation speed is the rate of the propagation of function *f* over a unit of lattice spacing at each unit of time spacing and with the assumption of the isothermal ideal gas the equation 4.44 can be written as:

$$f_i\left(\vec{x} + \Delta t * \vec{\xi}_i, t + \Delta t\right) - f_i(\vec{x}, t) = -\frac{\Delta t}{\tau} * \left(f_i(\vec{x}, t) - f_i^{eq}\right) \tag{4.45}$$

The left-hand side of the above equation describes the propagation of the distribution function according to the discretized directions in a time step, when the right-hand side describes the change of the distribution function, that tends towards equilibrium with a relaxation time. The generalized equation with introduced matrix collision operator is defined as follows:

$$f_i\left(\vec{x} + \Delta t * \vec{\xi}_i, t + \Delta t\right) - f_i(\vec{x}, t) = -\sum_j \Omega_{ij} * \left(f_j(\vec{x}, t) - f_j^{eq}\right) \tag{4.9}$$

The Navier-Stokes equations can be retrieved via kinematic viscosity and relaxation time direct link, by utilization of the Chapman-Enskog expansion of equation 4.46 [86].

The Chapman–Enskog theory provides a framework in which equations of hydrodynamics for a gas can be derived from the Boltzmann equation. The technique justifies the otherwise phenomenological constitutive relations appearing in hydrodynamical descriptions such as in the N-S equations. In doing so, expressions for various transport coefficients such as thermal conductivity and viscosity are obtained in terms of molecular parameters. Thus, Chapman–Enskog theory constitutes an important step in the passage from a microscopic, particle-based description to a continuum hydrodynamical one.

Then the following link between micro- and macroscopic worlds can be defined [87]:

$$\nu = \left(\tau - \frac{1}{2}\right) c_s^2 \qquad (4.10)$$

where: ν denotes the kinematic viscosity of the fluid.

4.3.5.3 MRT

In contrary to the BGK-SRT model, where one deal with only one coefficient of relaxation, a set of multiple relaxation times (MRT) could be used for all distribution’s functions f_i, equal to the number of finite discrete velocities. Furthermore, it was proven that BGK model has a number of stability problems and shows tendency to fail even when the Reynold numbers are low [88]. to solve these stability problems The LB Multi-Relaxation Time model was introduced by d'Humieres [89].

The MRT-LB model is treated as a generalised operator of collisions of the LB formula 6.46 defined in the evaluated form of a matrix. The distribution functions of the phase space are decomposed into a q-dimensional space, called the moment space. The collision matrix Ω becomes the $q \times q$ matrix, where q is the number of velocities of the set.

The hydrodynamics moments (typically the densities, momentum and several secondary tensors) are included in this matrix also with some non-hydrodynamics moments. They occur due to the fact that in some stencils there are more possible velocities than possible hydrodynamic moments, i.e. in D2Q9 scheme. Their task is to fill out the relaxation time matrix but there is no general well-posed condition to specify them. The non-hydrodynamic relaxation times are usually set close to one but there exist also other techniques that allow to establish the optimal values for these moments [90] [91]. Despite the fact that this approach differs from the kinetic gas theory basis, it provides better stability and accuracy than the BGK-SRT method in most cases. For a detailed derivation, please find d'Humieres et. al. [92].

4.3.6 Lattice Arrangements

It is important to partition the solution domain into lattices. The factitious particles (functions of distribution) exist at each lattice node. Some of these particles migrate (stream) to the neighbouring nodes in defined directions and then collide with the next nodes exchanging information about distributions. The amount of paths, links, depends on the structure of the lattice. lattice spaces must be equidistant in a uniform grid and, in turn, a grid must satisfy symmetry in order to recover the macroscopic formulas satisfactorily from the moments. This is done in a distinct formalism by way of weighted summations with the weighting variable universal. The common terminology is as follow *DnQm,* where n represent the dimension of the problem, and m refers to the speed model, number of linkages. The following subsections includes schemes and basic information about them for 1D, 2D and 3D dimension.

4.3.6.1 One-Dimensional Arrangement

The most basic form of arrangement is the D1Q2 model. There are also the D1Q3 and D1Q5 schemes. The particles move from the central node towards the side neighbours through connections between them, at certain speeds. For 1D cases, the most popular form of organization is the D1Q3 scheme.

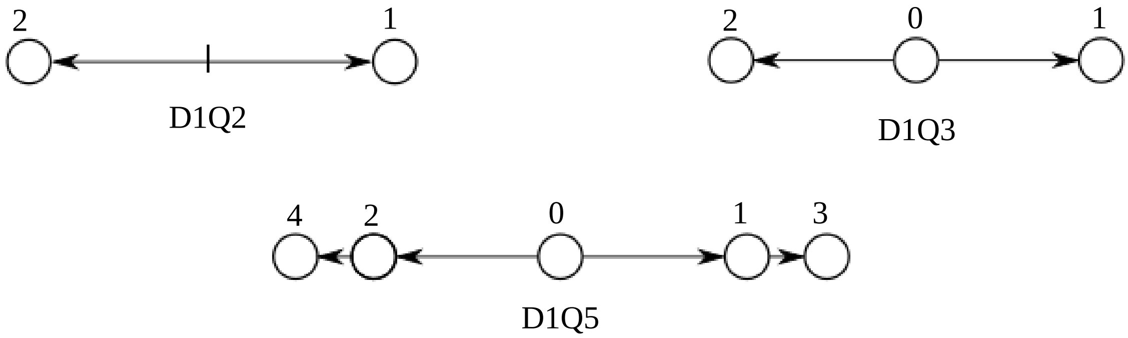

Fig. 4.1. Lattice arrangements for 1-D cases

The continuous propagation speed turns into a set of discrete velocities arbitrary numerated ξ_i . The table below summarizes the values of velocity and weights ω_i of distribution function for each direction of propagation.

D1Q2			**D1Q3**			**D1Q5**		
i	ξ_i	ω_i	**i**	ξ_i	ω_i	**i**	ξ_i	ω_i
-	-	-	0	0	4/6	0	0	6/12
1	1	1/2	1	1	1/6	1	1	2/12
2	-1	1/2	2	-1	1/6	2	-1	2/12
						3	1	1/12
						4	-1	1/12

Fig. 4.2. Set of 1-D arrangements velocities with their corresponding weight coefficient [81]

4.3.6.2 Two-Dimensional Arrangement

The below two diagrams are D2Q4 and D2Q5 arrangements. The first scheme does not contain a central node, and the nodes stream in four perpendicular directions. In the D2Q5 diagram there is an additional central nod whose speed is 0. It is worth mentioning that these diagrams cannot be used to model the fluid flow properly, the D2Q9 model (Fig. 4.3) is used for that purpose.

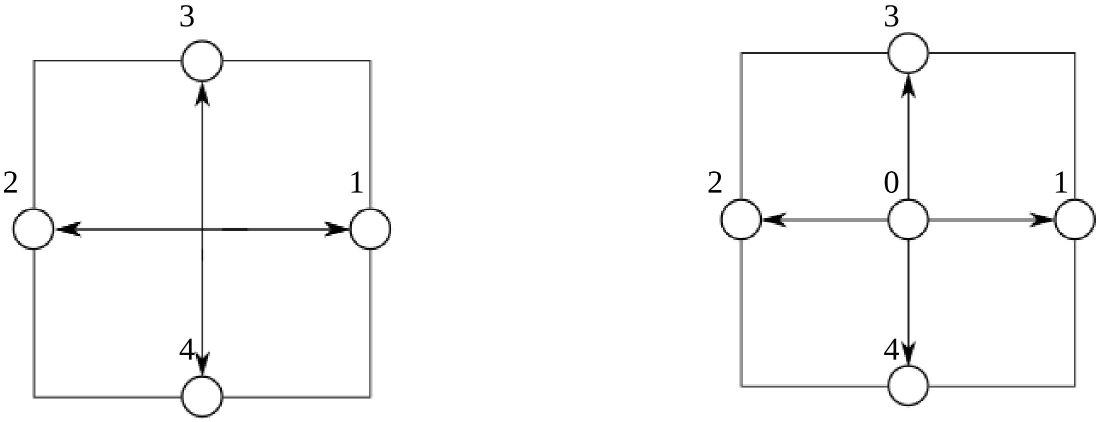

D2Q4 D2Q5

Fig. 4.3. Lattice arrangements for 2-D cases

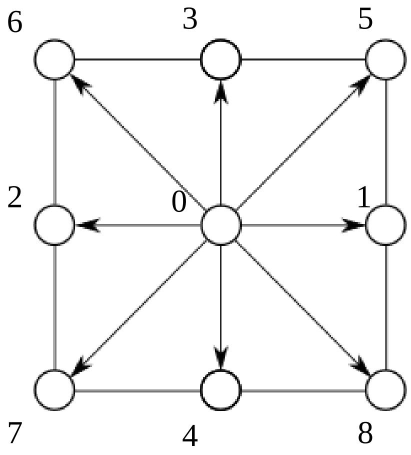

Fig. 4.4. D2Q9 lattice arrangement

Accordingly, additional nodes appear on the vertices that allow to capture the hydrodynamic nature of the flow and more accurately deal with the advection-diffusion equation. This is a very popular model that was also used to analyze 2D flow through the micro-gap channel at a later stage.

D2Q4			**D2Q5**			**D2Q9**		
i	$\boldsymbol{\xi_i}$	$\boldsymbol{\omega_i}$	**i**	$\boldsymbol{\xi_i}$	$\boldsymbol{\omega_i}$	**i**	$\boldsymbol{\xi_i}$	$\boldsymbol{\omega_i}$
-	-	-	0	(0,0)	2/6	0	(0,0)	4/9
1	(1,0)	1/4	1	(1,0)	1/6	1	(1,0)	1/9
2	(0,1)	1/4	2	(0,1)	1/6	2	(0,1)	1/9
3	(-1,0)	1/4	3	(-1,0)	1/6	3	(-1,0)	1/9
4	(0,-1)	1/4	4	(0,-1)	1/6	4	(0,-1)	1/9
						5	(1,1)	1/36
						6	(-1,1)	1/36
						7	(-1,-1)	1/36
						8	(1,-1)	1/36

Fig. 4.5. Set of 2-D arrangements velocities with their corresponding weight coefficient [81]

4.3.6.3 Three-Dimensional Arrangement

For the 3D dimension, the most commonly used schemes are the D3Q15 Fig. 4.6 and D3Q19 Fig.7. The first of them has 15 velocity vectors, and its equivalent with additional nodes on the centres of the front walls consists of 19 velocity vectors.

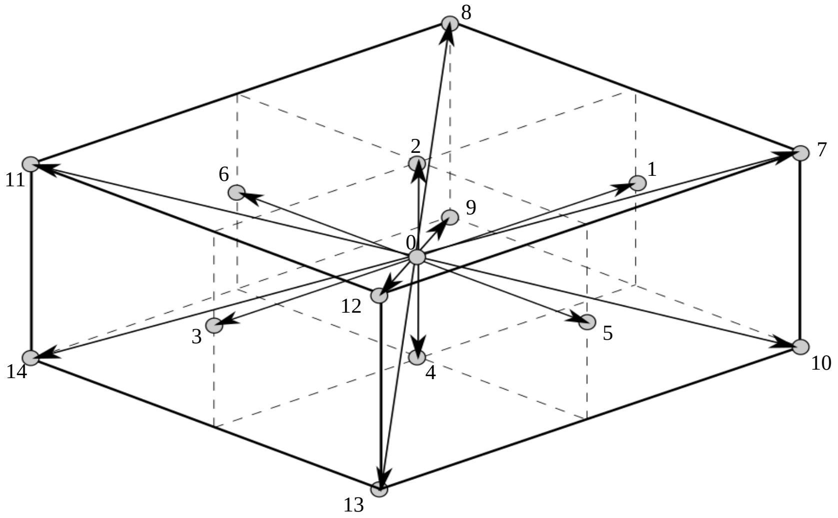

Fig. 4.6. D3Q15 lattice arrangement

It is shown that as the number of distribution functions increases, the accuracy of the simulations improves. The accuracy of the results also depends on how the boundary conditions are defined.

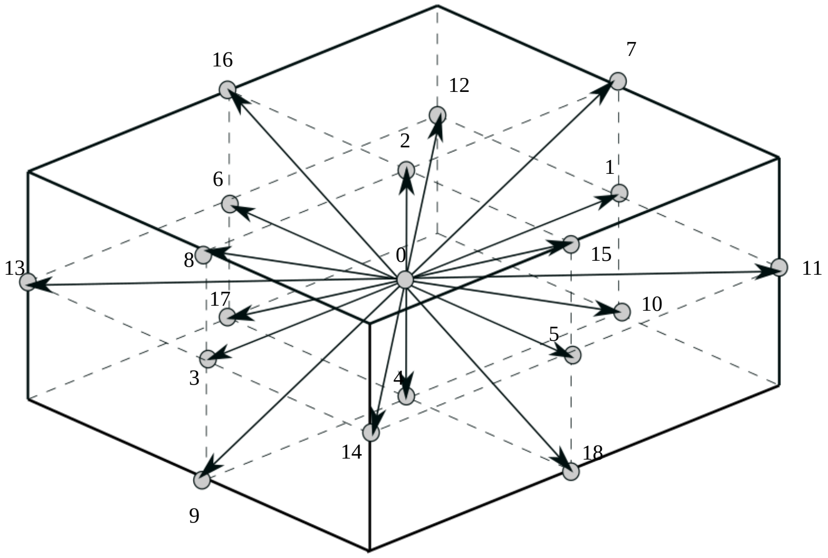

Fig. 4.7. D3Q19 lattice arrangement

The distribution weights are respectively:

D3Q15		D3Q19	
i	$\boldsymbol{\omega_i}$	**i**	$\boldsymbol{\omega_i}$
0	16/72	0	12/36
1-6	8/72	1-6	2/36
7-14	1/72	7-18	1/36

Fig. 4.8. Set of 3-D arrangements weight coefficients [81]

It is also possible to use arrangements with a different number of speed vectors, eg D3Q27. It should be remembered however, that this number has to sufficient to solve the problem and that the nodes lie correctly between each other. In models that take into account the so-called multi-speed approach, it is possible for a molecule to travel to more than one node in a given time step [81].

4.3.7 Boundary Conditions in LBM

The flow characteristics at a limit node cannot be determined using the same method as for the internal nodes therefore, correct boundary conditions need to be established for them in order to ensure a good projection of a hydrodynamic nature. The limitations of a certain domain are usually essential and must be handled carefully, to minimize any errors as much as possible. In the lattice Boltzmann method, many approaches are available to treat well boundary conditions. The most frequently encountered boundary conditions are described in the following paragraphs. A particular emphasis is put on the analysis of the non-equilibrium bounce-back boundary condition and its modifications which was applied into 3D micro-gap flow case done later.

4.3.7.1 General Classification

Computational fluid dynamics cannot rely only on the standalone governing equations, it requires additional definition of accurate initial and boundary conditions that depend on the behaviour of phenomena. It would be impossible to model the phenomenon numerically without the necessary information about its initial state and the behaviour of the fluid itself.

A reason describing how important is setting up proper initial and boundary conditions in the LBM was mentioned i.e. in [93]. In particular, initial conditions inconsistent with boundary conditions will results in occurrence of strong sound waves propagations in the system. However, these waves dissipate at certain point. A coherent procedure for determining the initial condition was proposed by authors of one of next discussed boundary conditions [94] [95].

Analysis in computational fluid mechanics are initial and boundary condition problems. They depend not only on the governing equations, but also on the modelling of the initial state, and the boundary conditions. Boundary conditions can be classified in the following way [96]:

1. Dirichlet boundary conditions
2. Neumann boundary conditions
3. Robin (Cauchy) boundary conditions
4. Periodic boundary conditions

Ad. 1.

Most popular, Dirichlet boundary condition sets the flow quantity U on a specific boundary location x_{BC} to a fixed value a:

$$U(x_{BC}) = a \tag{4.48}$$

These boundary conditions are vastly used for flow velocity and pressure distributions. Specific case of its utilization is related with the so-called no-slip boundary conditions at the walls, when it sets a fixed border velocity to zero

$$U(x_{BC}) = 0 \tag{4.49}$$

Ad. 2.

The next boundary condition type - the Neumann boundary condition, sets the derivative of U to some value a:

$$\frac{\partial U(x_{BC})}{\partial x_i} = a \tag{4.50}$$

The Neumann boundary conditions are typically used in the description of in- or outflow of a fluid, mass or energy.

Ad. 3.

The third type boundary conditions called interchangeably Cauchy or Robin type is a mixture of both previous Dirichlet and Neumann boundary conditions. An example for a Robin type is the free-slip boundary condition at the wall, which models a fixed boundary, where the velocity normal to the wall equals zero:

$$\partial U_{\perp} = 0 \tag{4.51}$$

and for the tangential components $U_{||}$ sets their gradient to zero.

$$\frac{\partial U_{||}(x_{BC})}{\partial x_{||}} = 0 \tag{4.52}$$

General equation form of the Robin boundary condition can be written as:

$$a_1 \frac{\partial U(x_{BC})}{\partial x_i} + a_2 U(x_{BC}) = a_3 \tag{4.53}$$

where: a_1, a_2 and a_3 are fixed values.

Ad. 4.

The last type, the periodic boundary conditions, which are often used in tests and preliminary simulations. Their strength is very easy implementation that allows to exchange the populations from opposite ends of the domain along the direction of fluid motion with a simultaneous reduction of computational resources.

There exist also other more complex boundary conditions that are classified in higher order types, but they will be skipped because they are not in the field of interest of this dissertation.

4.3.7.2 Bounce-Back Method

One of the most commonly used boundary conditions in the LBM is the Bounce-Back (BB) boundary condition. It is based on finding unknown population values directly on the basis of the incoming value of the distribution function and its subsequent reflection with the reverse propagation vector of population. The advantages of this method are the simplicity of its implementation, robustness. It can provide second order accuracy once the geometry boundary is in the middle between lattice nodes and it is also stable at large value of Reynolds number. Moreover, in full-way Bounce-Back method the distribution functions omit the collision step. The disadvantages are the loss of accuracy when the interface between phases is not in a central position between the information exchange nodes. However, there exist various versions of this method that try to deal with interface position problems i.e. [97]. Author of the paper Bouzidi developed the generalization of the Bounce-Back boundary conditions that enables the boundary interface to be put not only in the halfway but also in the arbitrary manner between two grid layers.

Due to the type of distribution function propagation, the Bounce-Back method can be divided into full-way and mid-way BB. In each of these two methods, depending on the boundary conditions assigned to the boundary, one can additionally distinguish between versions with no-slip and free-slip wall treatment [98]. Figures 4.9 and 4.10 respectively show the scheme of operation of the full-way method and mid-bounce back with no-slip and a free-slip horizontal wall.

Full-way Bounce-Back method very commonly applies to the outgoing populations that cross the fluid-solid boundary and reach wall nodes in which populations are unknown (step I – II). Afterwards, these functions are reoriented and sent back to the fluid domain in the next streaming step (III – IV step) therefore, this technique requires two streaming steps to recover the transfer information. Because of the lag in the full-time step between the departure of the populations and the subsequent entry of the incoming populations full-way BB method it is not purely mass-conservative. The computational formulation for no-slip Bounce-Back method is as follows:

$$f_{\bar{\imath}}(\vec{x}_b, t) = \tilde{f}_i(\vec{x}_b, t) \tag{4.54}$$

where: $\vec{x}_b$ is the wall node linked to a corresponding fluid node, $\bar{\imath}$ is the opposite direction of the velocity i, and $\tilde{f}_i$ stands for the post-collision distribution function.

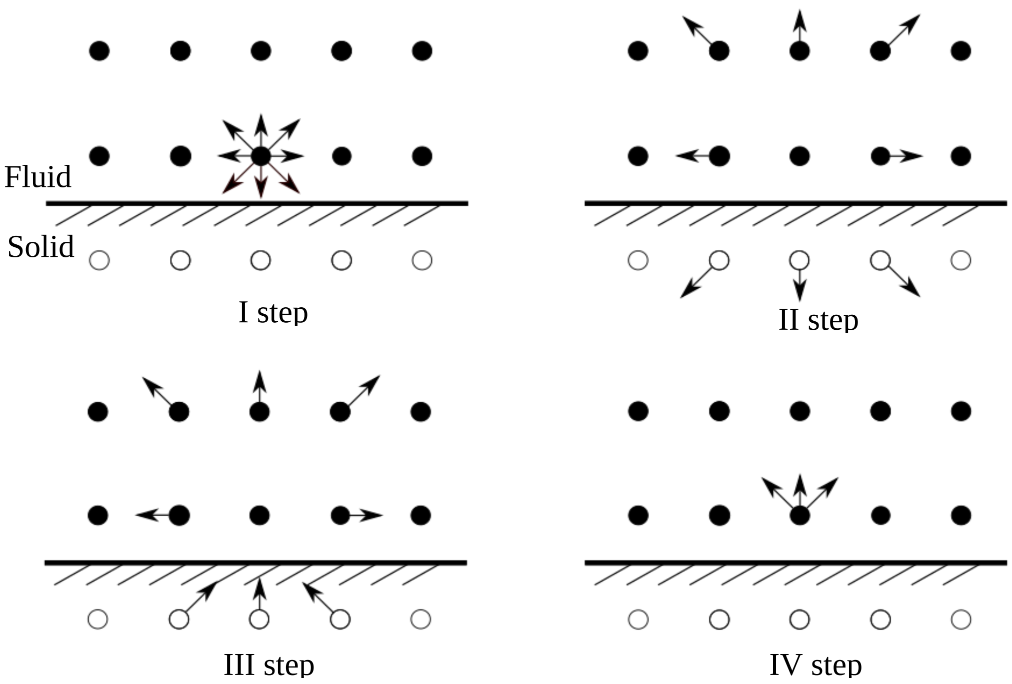

Fig. 4.9. Four steps of full-way bounce-back scheme applied on a no-slip horizontal wall

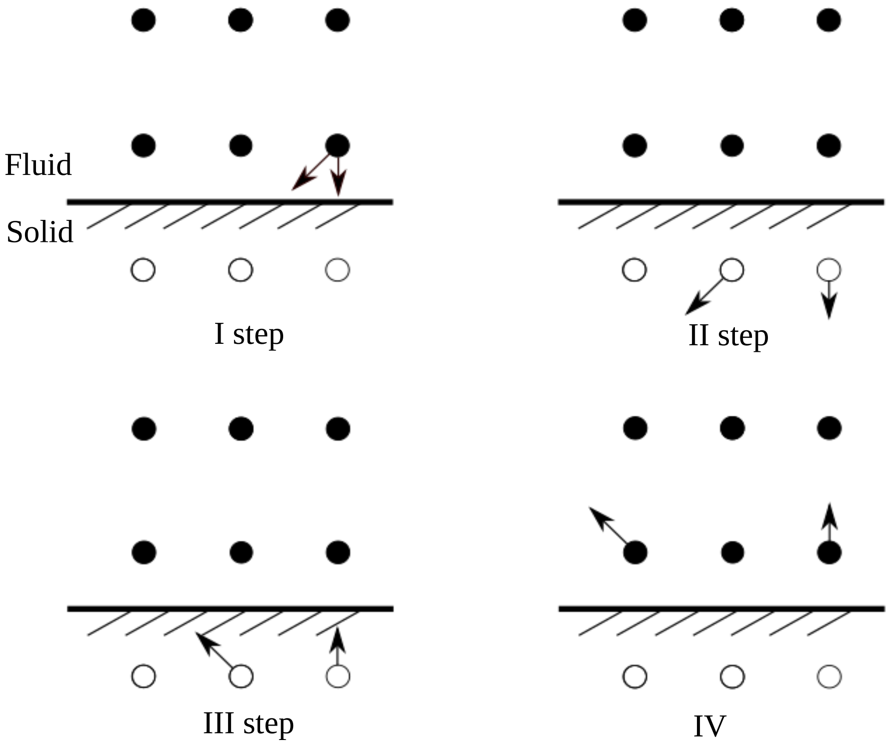

Fig. 4.10. Four steps of full-way bounce-back scheme on applied a free-slip horizontal wall

In case of the free-slip full-way BB method the same rules are valid, however, the specular reorientation of the outgoing populations occurs (Fig. 4.10).

By definition, therefore, the first and second type boundary conditions apply after specular reflection because of the normal velocity component is set along with the gradient of the transversal velocity to zero – Dirichlet BC, and a Neumann BC for the parallel velocity component. In free-slip scenario, the formulation is similar to the no-slip one:

$$f_{\bar{\bar{\imath}}}(\vec{x}_b, t) = \tilde{f}_i(\vec{x}_b, t) \tag{4.55}$$

where: $\bar{\bar{\imath}}$ denotes the specular reflection of the i direction.

Second group of schemes are mid-way BB methods. In contrary to the full-way BB, the mid-way BB does conserve the mass balance at the boundary. The BB rule is also guided within a single streaming phase, implying that the distribution of particles goes back and forth over a full distance. As its name implies, the mid-way BB rule considers the physical boundary right in the centre between the fluid node and the wall node and this makes the midway BB in space to precise in second order. The illustrations on the next page show the mid-way processing schemes.

First step shows an initial state within the populations are stored, then, the streaming step is performed for all the other populations (II step), subsequently, the stored populations that leave the domain are reoriented (III step) and replaced in the prescribed directions (IV step). As with the full-flow BB method, the mid-way BC no-slip technique is totally local and fulfils the principle of returning the particles to their original node in one step. On the other side, on fig. one can notice that free-slip BB method is completely non-local, while outgoing populations stream towards different nodes. Another skilful use of free-slip wall may be useful seeing that, this condition can be also used as a mirror boundary condition for axisymmetric problems.

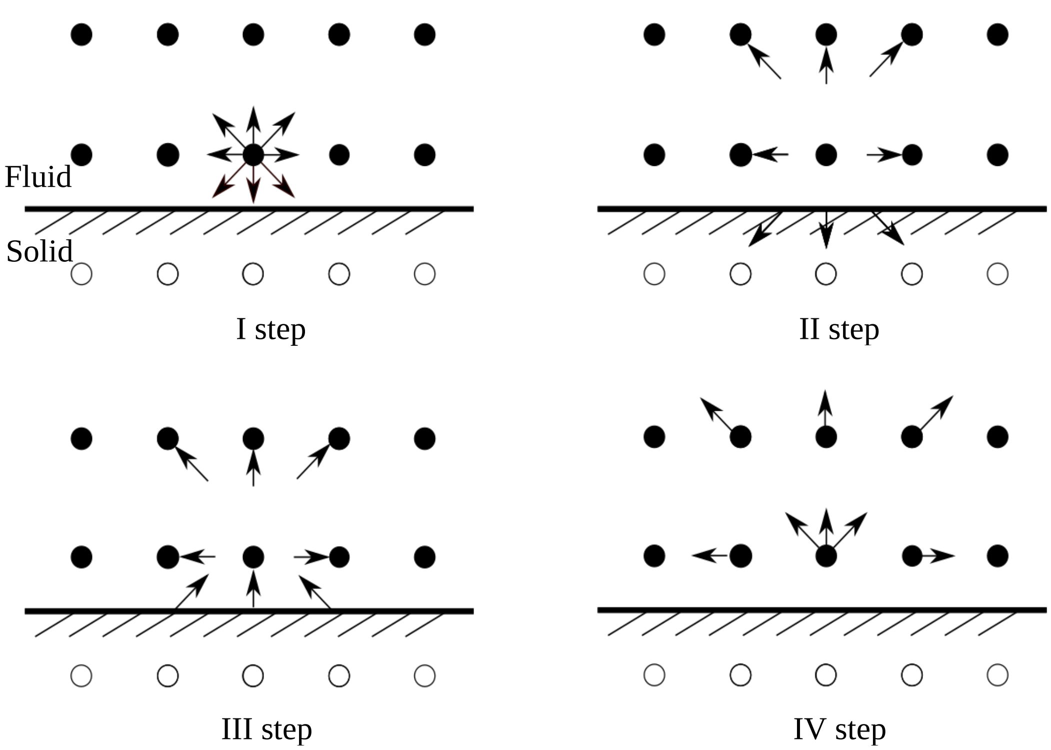

I step

II step

III step

IV step

Fig. 4.11. Four steps of mid-way bounce-back rule applied on a no-slip horizontal wall

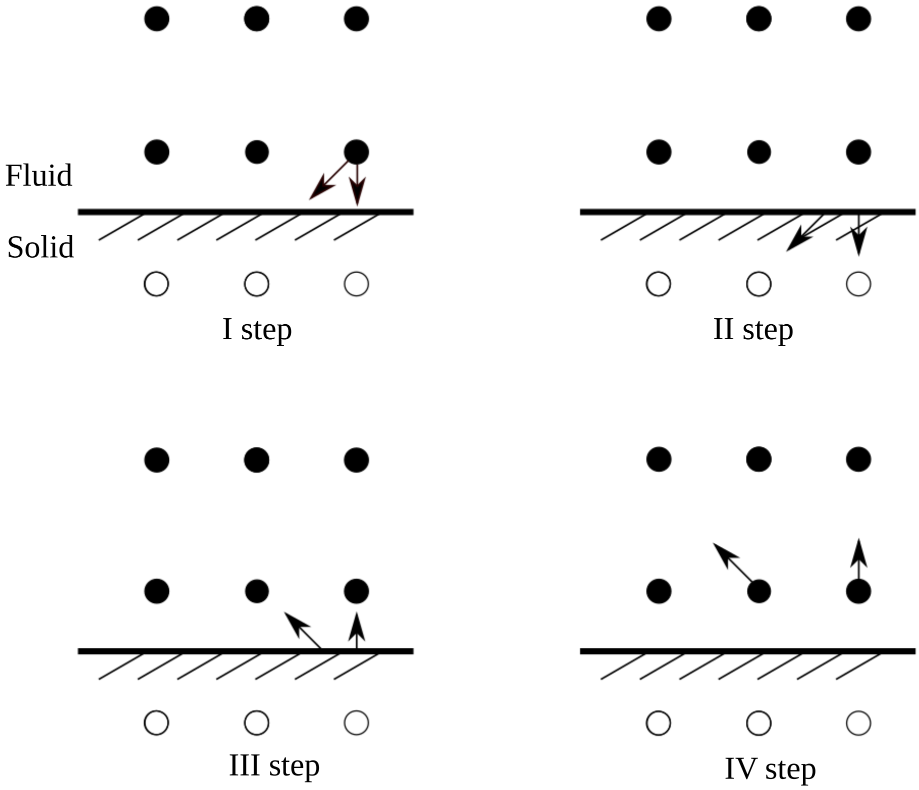

I step

II step

III step

IV step

Fig. 4.12. Four steps of mid-way bounce-back rule scheme applied on a free-slip horizontal wall

The general formulation of the mid-way no-slip BB and free-slip boundary condition are defined respectively as follows [99]:

$$f_{\bar{\imath}}\left(\vec{x}_f, t+\Delta t\right) = \tilde{f}_i\left(\vec{x}_f, t\right) - 6\omega\rho(\vec{\xi}_i * \vec{u}_w) \tag{4.56}$$

where $\vec{x}_f$ denotes a fluid node linked to a corresponding wall node, $\vec{u}_w$ is the velocity of the wall.

$$f_{\bar{\bar{\imath}}}\left(\vec{x}_f + \Delta T_i, t+\Delta t\right) = \tilde{f}_i\left(\vec{x}_f, t\right) \tag{4.57}$$

where: ΔT_i is the distance to the destination node.

Once, one considers in eq. 4.56 that $\vec{u}_w = 0$, which physically means a steady wall, the very right term of the equation will disappear. It results from this fact that the no-slip mid-way BB with a steady wall is applicable to hydrodynamic and passive scalar distribution functions as well. Hence, the following formulation can be written:

$$h_{\bar{\imath}}\left(\vec{x}_f, t+\Delta t\right) = \tilde{h}_i\left(\vec{x}_f, t\right) \tag{4.58}$$

where: h_i can be a distribution function for momentum transfer problems, or g_i for heat or mass transport processes.

4.3.7.3 Curved Walls Treatment

Unfortunately, as with all methods, each has some limitations and there is no exception regarding the Bounce-Back method. To correctly cover the accuracy of the results of the second order, the wall must be a straight one placed exactly between two lattice nodes. The operation algorithm in the case of application on curved wall of any BB method will cause that during the simulation the interface between fluid and solid will be wrongly interpreted. The computational border called as *effective computational wall* will look like stairs with nodes located on it in-line (Fig. 4.13). This obviously will contribute to a reduction in the accuracy of the simulation results. Below, different methods developed to solve the problem of proper bounce-back description for curved surface boundaries will be discussed briefly.

The authors of the first reviewed solution were aforementioned Filippova and Hänel [78]. In their solution the unknown reflected populations are determined as a linear combination of the incoming population and the fictitious boundary equilibrium. The velocity within the solid is obtained by linear extrapolation from the last fluid node and the predefined boundary velocity. (Fig. 4.13).

The weight coefficients of the linear combination are dependent on the respective link's cut ratio and can be obtained from a Chapman-Enskog expansion. However, in the case of wall nodes located close to the solid boundary, a loss of stability occurs for pressure driven channel flows [100].

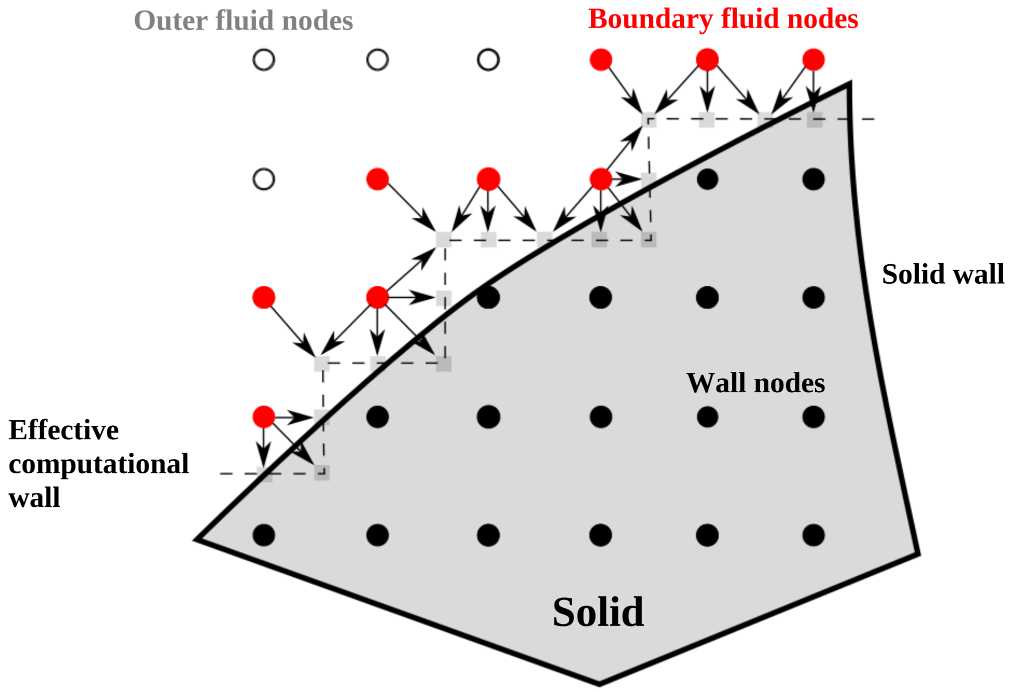

Fig. 4.13. Curved wall object with Filippova and Hänel BB method applied

The cure for above was found by Mei, Luo and Shyv (MLS) [101] who adjusted the boundary fitting scheme and proposed the improved version by introducing presented on Fig. 4.14 Langrangian array of "off-lattice" nodes computationally stored on the boundary (yellow nodes). This set was used then for calculating the link distance from the fluid node to the solid wall.

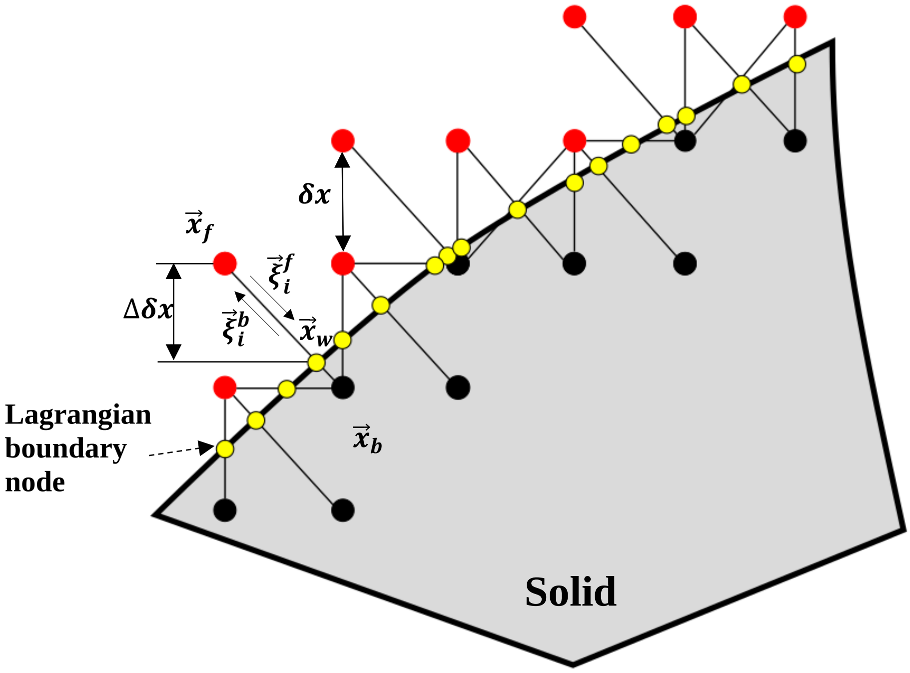

Fig. 4.14. Curved wall object with MLS-BB method applied

Where: $\vec{x}_b$ denotes the lattice wall node, $\vec{x}_f$ is corresponding fluid node, $\vec{x}_w$ denotes the effective wall nodes, $\Delta\delta x$ is the normalised distance between the effective wall node and the fluid node, relative to the fluid-solid distance (δx), $\vec{\xi}_i^b$ $\vec{\xi}_i^f$ are distribution functions of fluid Bounce-Back to solid and vice-versa.
The MLS approach has been proved numerically to improve stability of the system considerably [102]. The mathematical expressions used within MLS-BB can be found in the original paper [101].

Third way to deal with curved object boundaries was already pointed out in the Section 4.3.8.2**,** that is Bouzidi boundary condition [97]. One important feature of this approach is that interpolation is performed only by particle populations in one direction. As a consequence, the one-dimensional case shown in Fig. 4.15 is sufficient to pose the method algorithm.

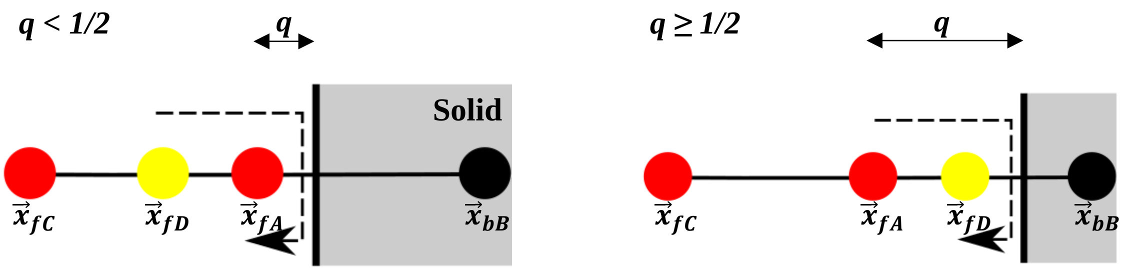

Fig. 4.15. Bouzidi interpolation scheme

Based on the value of wall distance to the closest fluid node that exchange information $\vec{x}_{fA}$, denoted as q, either pre-collision or post-collision is interpolated. If q is equal 0, 1/2, or 1 fluid node with subscript A fully transfers back the information after reaching the wall and the situation reduces to a typical mid or full way Bounce-Back method. However, when q value varies between above ranges, two cases can be distinguished referring to Bouzidi:

1) If $q < 1/2$, then the fictitious particles population at location D is obtained from linear interpolation from destination A and C,
2) If $q > 1/2$, the pre-streaming population at D can be reached only with an extrapolation that is less robust and should be avoided.

Bouzidi has also shown that his technique can be efficiently extended to moving boundary cases [103]. Nevertheless, as Rohden et al. showed in their study, it is difficult to use Bouzidi's algorithm to volumetric systems [104]. It turned out the Bouzidi scheme is vulnerable to failures in the mass conservation equations.

Chun and Ladd [105] proposed in 2007 another way in which curved boundaries within LBM can be handled. They employed the Bouzidi interpolation scheme for the equilibrium distribution and the traditional Bounce-Back method for the non-equilibrium part. The so-called Equilibrium Interpolation (EI) is second-order accurate and requires only one fluid node in between the boundaries. In addition, a location of boundaries remains viscosity-independent, and the method provides higher accuracy and reliability than the linear and quadratic interpolation schemes. Interpolation of equilibrium distribution is potentially the best stable choice from all previously mentioned methods.

4.3.7.4 Zou-He Boundary Condition

In many engineering cases, the speed distribution or constant pressure value at the inlet or outlet of the computational domain is known, e.g. channel flow. In 1997, Zou and He proposed an approach to solve such a problem within the LBM method [102]. Let is consider the case from Fig. 4.15 in which the distributions f_2, f_6, f_3, f_7 and f_4 are known at the inlet. At the top and the bottom, the channel has no-slip horizontal walls. Usually, this issue involves a boundary condition of the Dirichlet form, in which the velocity of the inlet is and pressure at the outlet are fixed. In the analysed case, we are looking for three other distributions at the inlet of the channels f_1, f_5 and f_8, marked with dash lines.

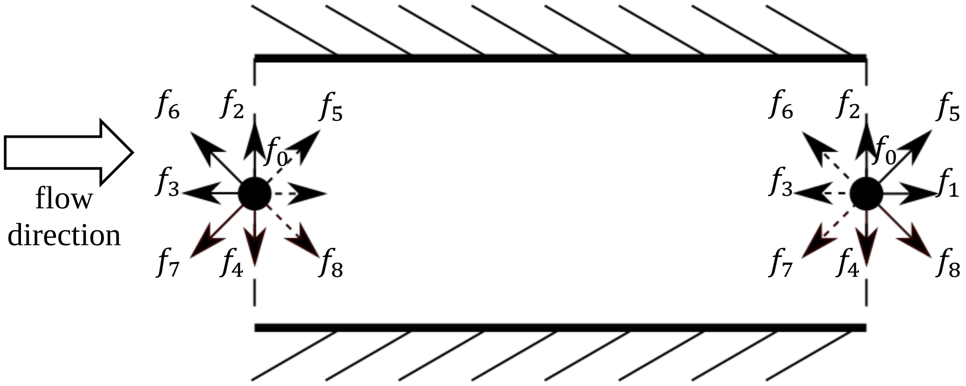

Fig. 4.15. Unknown distributions at the inlet and the outlet of the channel flow

Assuming that the speed is known at the inlet and equals $u_{inlet} = [u, 0]$, and knowing that the sum of all components of the distribution function gives macroscopic density (Eq. 4.4), we get:

$$\rho = f_0 + f_1 + f_2 + f_3 + f_4 + f_5 + f_6 + f_7 + f_8 \tag{4.59}$$

Sum of distribution in x direction:

$$\rho u_x = f_1 - f_3 + f_5 - f_6 + f_7 - f_8 = \rho u \tag{4.60}$$

Sum of distribution in y direction:

$$\rho u_y = f_2 - f_4 + f_5 + f_6 - f_7 - f_8 = 0 \tag{4.61}$$

We have four unknowns (f_1, f_5, f_8 and ρ) and only three equations. Zou and He proposed that the non-equilibrium parts of the populations normal to the boundary are equal to each other, hence:

$$f_1 - f_1^{eq} = f_3 - f_3^{eq} \tag{4.62}$$

The equilibrium distribution functions f_1^{eq} and f_3^{eq} can be calculated respectively to the arrangement type basing on evaluation of equation 4.25. From the equations above it is possible to determine next the missing distribution values at the channel inlet. Following the same algorithm, one is able to establish unknown distributions at the outlet of the channel.

4.3.7.5 Periodic Boundary Condition

To ensure repeating stream propagation features, periodic boundary conditions are essential. The flow parameters are the same over the line *a* as under the line *b*. The movement between these two lines is therefore "equivalent" and along these borders, periodicity can be applied. The distribution functions that are leaving line *a* are the same as the distribution functions entering from line *b* and vice versa. For below case the distribution functions f_7, f_4 and f_8 are unknown on the line *a* and f_6, f_2, f_5 are unknown on the line *b*. The periodic boundary can be defined as follows:

Along line *a*:

$f_{7,a} = f_{7,b}$, $f_{4,a} = f_{4,b}$, $f_{8,a} = f_{8,b}$

Along line *b*:

$f_{6,a} = f_{6,b}$,$f_{2,a} = f_{2,b}$, $f_{5,a} = f_{5,b}$

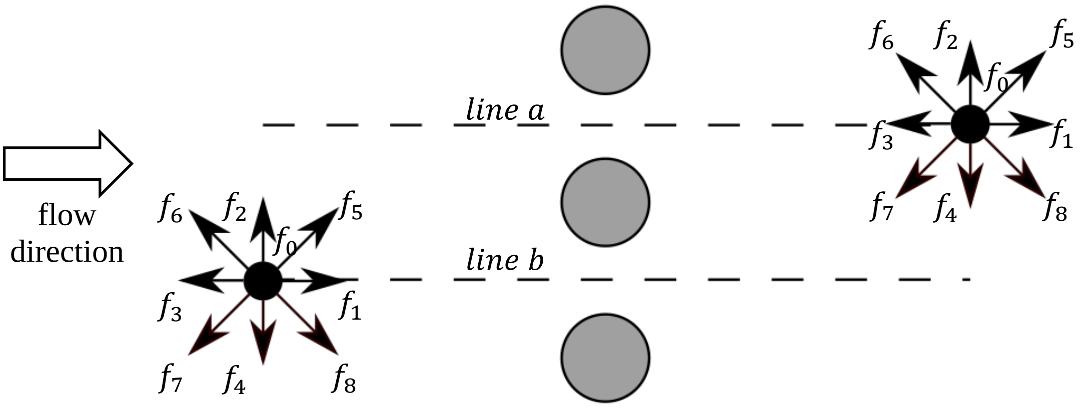

Fig. 4.16. Periodic flow boundary condition

4.3.7.6 Symmetry Boundary Condition

Many practical problems show a symmetry along a line or a plane. Then it is beneficial to find a solution for only one part of the domain, which saves computer resources. For example, flow in a channel, Fig. 4.17, the flow above the symmetry line is mirror image of the flow below the symmetry line. Therefore, the integration should be carried only for one party of the domain, and symmetry condition need to be applied along the symmetry line.

In below case the distribution function f_6, f_2 and f_5 are unknowns. Their mirror images are set to them in order to define unknown functions, i.e., $f_6 = f_7$, $f_2 = f_4$ and $f_5 = f_8$.

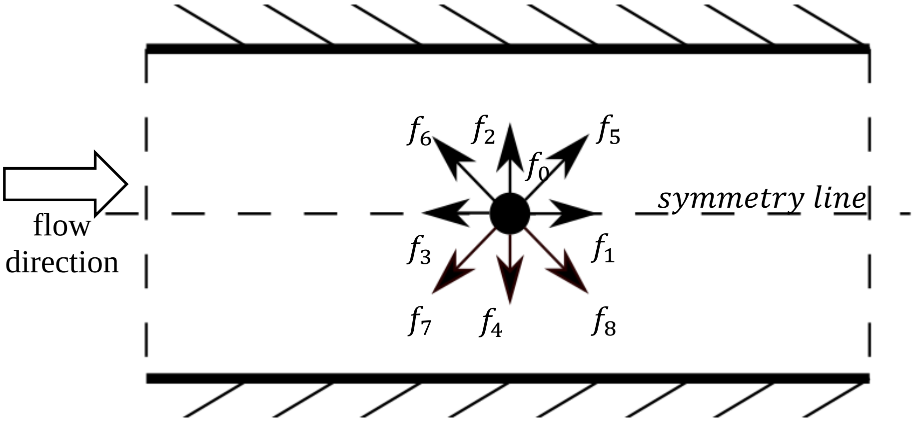

Fig. 4.17. Symmetry flow boundary condition

4.3.7.7 Immersed Boundary Condition

The immersed boundary method (IBM) is widely known and utilised in the classical CFD analysis but it proved its usefulness also in the Lattice Boltzmann Method. First time the IB method was proposed by Peskin in 1970 to simulate the blood flow in a two-dimensional heart model [106].

IBM's fundamental premise is that the fluid-solid boundary is being deformed but at the same moment it is still extremely stable. The deformation or displacement of the boundary generates a force which helps to restore the border to its original shape or location. The fluid field is composed of Eulerian nodes using a fixed cartesian grid and on the other side set of Lagrangian points represents the spatial physical boundary submerged in the fluid. The restorative force on the boundary is then transmitted as body force in the adjacent nodes (Eulerian nodes). The governing flow field equation with a body force can then be solved in the entire fluid field, both inside and outside the boundary. The conventional immersed boundary method also has 2 significant disadvantages:

1) Throughout the solution phase the no-slip boundary condition is not executed and therefore certain streamlines may enter the solid body
2) The embedded near the boundary the Diract delta interpolation function is first-order accurate hence the main solution also is of weaker form.

Similarly, to classical CFD analysis also the LBM typically uses the Cartesian grid and because of that it was possible to fuse these two techniques into the so-called the Immersed Boundary-Latiice Boltzmann Method (IB-LBM),

In 2004 Feng and Michaelides presented this new approach for the first time [107]. They tested utilisation of the IB-LBM to simulate two- and three-dimensional rigid particle motion. In both cases they managed to do that successfully, however, computations of the restoring force were unreliable.

Authors Shu et al. [108] and Wu et al. [109] in their works tried to search for a solution and new ideas based on velocity corrections which could terminate the problem of solid body streamlines penetration. However, both proposed methods were only of the first-order of accuracy due to the use of Dirac’s delta interpolation function.

In 2014 Wang with co-workers [110] came out with a new proposal of approach that can handle the no-slip boundary condition. After calculating the basic velocity field using LBM on the Cartesian mesh, they applied the second-order Lagrange interpolation to correct the velocity in the vicinity of the boundary points on Eulerian mesh. To effectively consider the body force in the lattice Boltzmann equation (eq. 4.13), authors used the model proposed by Guo et al. [80]. Their performed a validation for a two-dimensional steady and unsteady flows around a cylinder and compared results with literature available data. The results matched well, and most importantly problem with streamlines passing through the solid body by satisfying no slip boundary condition was eliminated.

4.4 Chapter Summary

The chapter explains the history of the development and rules of the LBM framework. This is, of course, just part of the knowledge condensed in a pill that reveals the elegance and richness of the process itself. The author wanted to convey the foundations to the reader in a clear and understandable way, making him familiar with an innovative approach of solving the computational problems of fluid mechanic. The method itself is in constant development, and individual companies seeking to encourage new customers to explore and practice with the method by free-access codes or commercial solvers for more advanced industrial applications. The utilisation of the last one will be presented in the next chapter. The boundary conditions and the procedure for calculating the coefficient of heat transfer at the interface of the two bodies in the vicinity of the flowing fluid will also be described in depth.

Chapter 5: Analysis Setup

This chapter is entirely devoted to performing a metal-air-metal thermal contact conductance computational analysis. With knowledge about the basic surface topography descriptors that are available usually in the company, it is possible to more accurately estimate TCC values affecting the temperature distribution of aircraft engine components at the mesoscopic level. The results obtained from numerical simulations will allow a thermal contact conductance correlation to be derived that later will be verified against the available literature data and applied to a macro-scale finite element analysis. Lessons learned will determine the validity and usefulness of the numerical methods which nowadays are mandatory activity of the R&D departments of all aviation companies. Those methods are now also a key aspect of the design of engine components which, due to better knowledge of the temperature fields, can be used for more accurate estimations of the strength and life cycle of the turbine jet engine as well as its durability and reliability. The whole numerical investigation process discussed in this work can be split into the following points:

1. Creation of a script enabling stochastic reconstruction of a mesoscale geometry of two rough surfaces being in contact
2. Study of the influence of size and shape of surface asperities along with applied pressure on thermal contact conductance behaviour
3. Investigation of the impact of various heat transfer modes on TCC values
4. Validation of method against available experimental literature data
5. Construction of an empirical correlation dependent on the findings of the computational analyses
6. Implementation of developed correlation in finite element simulation of aircraft engine low-pressure turbine components

5.1 Stochastic Surface Reconstruction

For the most precise representation of the actual surface contact, surface topographies were reconstructed stochastically with use of numerical tools. In order to do so, firstly a Python algorithm was created [111]. Entire script was based on typically collected industrial surface descriptors like mean absolute slope, arithmetic roughness and gap thickness using the standard Gaussian Cumulative Distribution Function (CDF) [112].

Table 5.1 presents values of the above parameters available for some of the contact pairs in the low-pressure turbine.

Contact / ***Property***	*Blade root – disc lug*	*LPT casing – turbine exhaust case*	*Front vane hook – LPT casing*
Material	PW1484 / PW1113	WASPALOY / H46	INCO718 / MAR-M-247
Roughness Ra [µm]	1.6 / 3.2	1.6 / 1.6	1.6 / 1.6
Thickness δ [mm]	2.08 / 3.46	3.68 / 4.55	3.05 / 4.19
Length L [mm]	1.41	21.01	2.67

Tab. 5.1. Surface descriptors for particular low-pressure turbine contact pairs

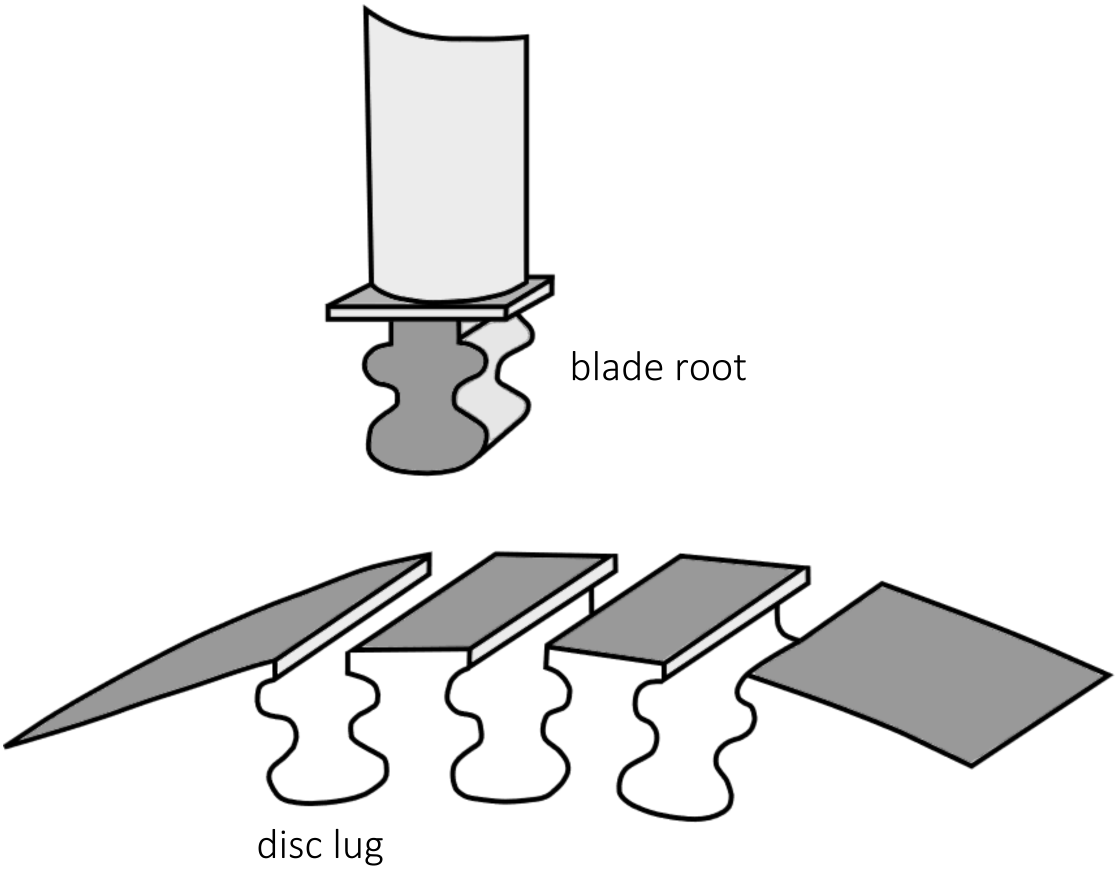

Fig. 5.1. Blade-disc attachment scheme

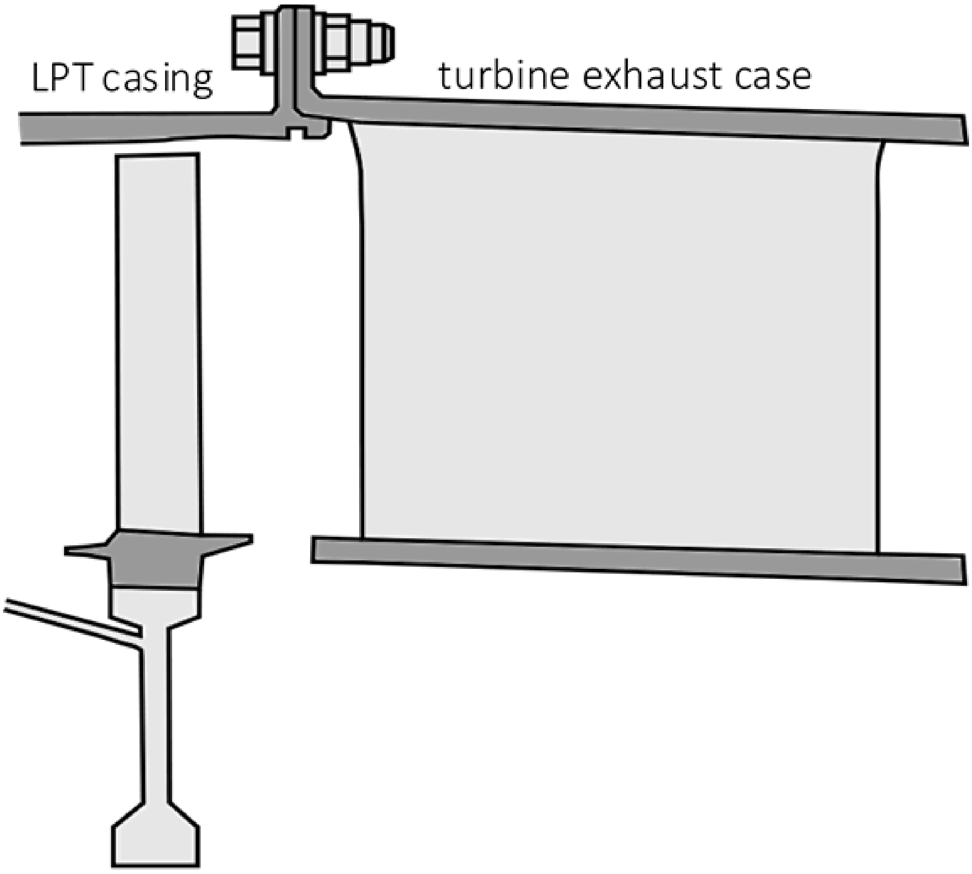

Fig. 5.2. LPT casing with TEC bolted joint assembly

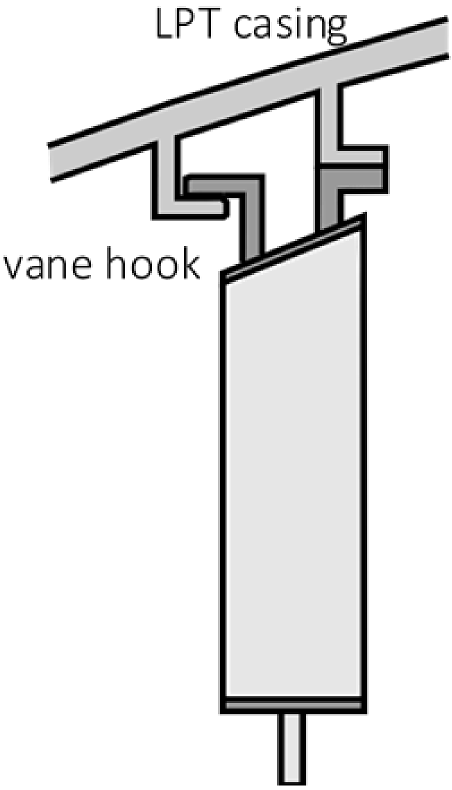

Fig. 5.3. Front vane hook and LPT casing connection

The principle of the script is to generate two-dimensional grid of points with y coordinates equal to the sampled heights about a mean plane parallel to the x-z plane. Then with three-dimensional grid of sampled heights, with the use of appropriate libraries, it is possible to reconstruct triangular mesh for bottom and top surfaces. Both surfaces are spaced apart by a distance measured between mean planes. The user is able to manually specify the artificial thickness of the surfaces to set their upper and bottom limits inside the code. The script performs automatically sharp roughness edges interpolation and removes the places where overlapping occurs, creating a contact spot. Finally, the mesh file is exported to the STL format allowing further utilisations. The following figure illustrates the result of the surface reconstruction example produced by python script.

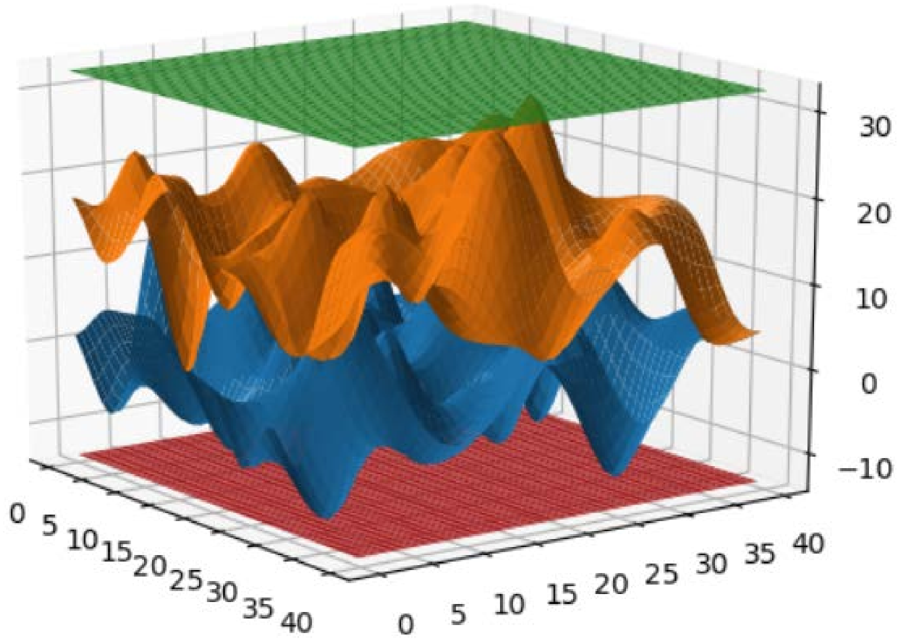

Fig. 5.4. Representative reconstructed 3D top and bottom rough surface case with both equal Ra=5[μm], vertical limits set on 1[μm] above the highest surface points, and separation distance equal 15[μm] measured between mean planes

The next step was to import the mesh into the HyperWorks environment [113] where the side surfaces were formed to close the solid and fluid domains and then construct a tetrahedral mesh for which the energy equation could be solved in further CFD calculations. Side surfaces in all simulations were treated as insulators (adiabatic wall boundary condition) to reduce heat losses.

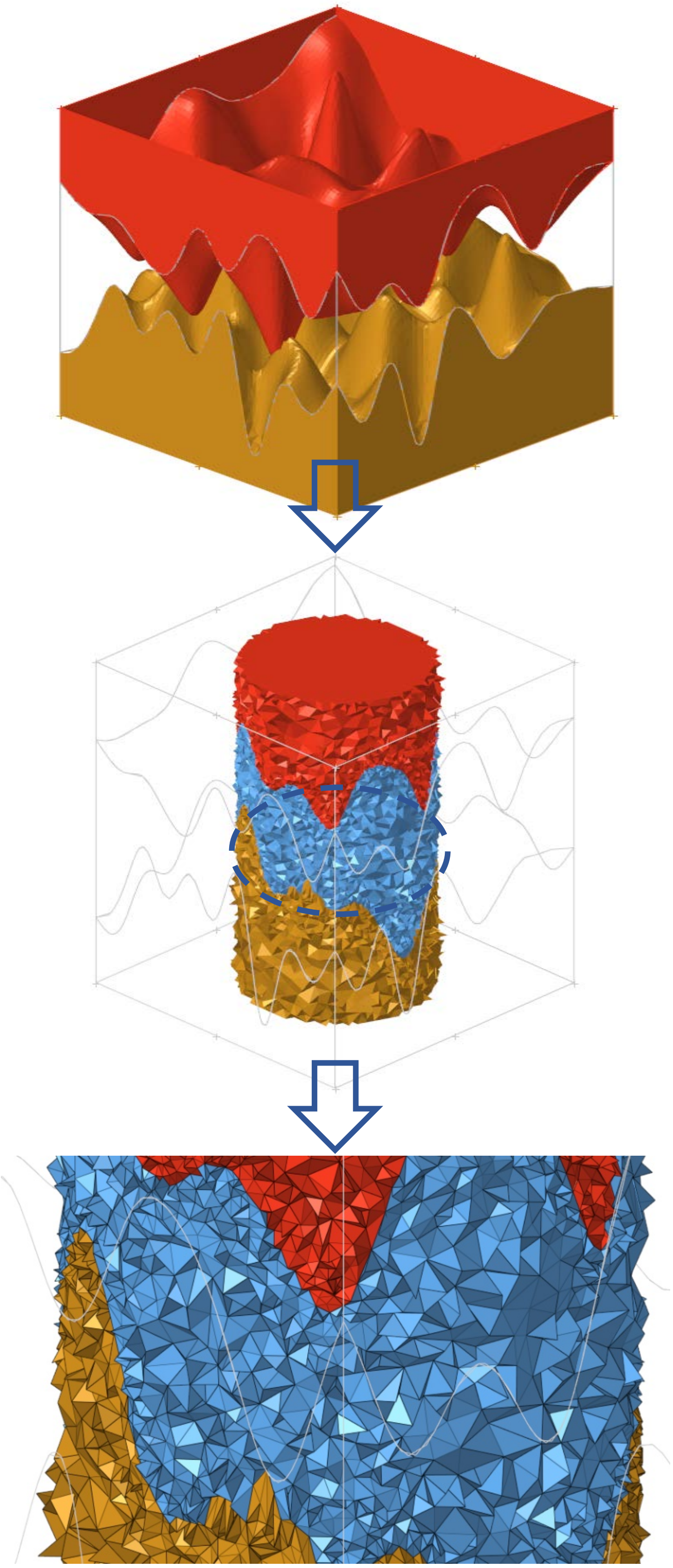

Fig. 5.5. Process of reconstruction of lateral surfaces and the creation of tetrahedal mesh for the solid and fluid domains. The presented 3D volumetric mesh is comprised of a total of 1,842,255 tetrahedral elements

5.2 Thermal Analysis

The simulations performed in order to estimate the thermal contact conductance from the thermal transport across the reconstructed interface were done using two software:

- steady-state conductive, convective and radiative heat transport computations in HyperWorks AcuSolver belonging to Altair Engineering company [114],
- transient forced convection calculations in the commercial X-Flow 2020 software being a part of Dessault Systemes SIMULIA package [115].

The first solver, about which was not too much said in the whole dissertation, is based on the classic Finite Volume Method approach. AcuSolve is characterised by high accuracy resulting from the use of equal order interpolation for all variables. For all governing equations, this results in second-order spatial precision. The emphasis on precision further improves the solver's speed by allowing the use of much less mesh to achieve higher levels of accuracy than is needed to obtain comparable results using other market available CFD solvers. AcuSolve is able to retain its second-order accuracy on all element topologies. Entire pre-processing done in this PhD was confidently simplified by use of tetrahedral elements as solid mesh and in fluid domain, without sacrificing robustness or accuracy. In addition to spatial accuracy, AcuSolve achieves second-order accuracy in time.

Thermal transport and conjugate heat transfer are no newcomers to this software. In AcuSolve code evaluates the convective heat transfer coefficient from the turbulent near-wall boundary layer similarly solution which is applicable for both velocity and temperature fields. For the momentum equations, solver uses the velocity one to enforce turbulence wall conditions and the temperature one to enforce conditions for the energy equation. The beauty of this approach is that in order to get the heat transfer coefficient, AcuSolve does not even need to solve the temperature field. Solver merely requires the flow equation to be resolved and the thermal material properties, conductivity and Prandtl number to be defined. This approach is reasonably reliable and non-oscillatory and works for complex industrial cases where the flow can arrive from a number of directions and with differing temperature conditions. However, knowledge of the edge position of the boundary layer (in terms of y+) is needed. As this is incredibly difficult to quantify exactly for general industrial flows, AcuSolve calculates it as a large y+, which can be freely modified by the user. The solution is very resistant to this value.

Additionally, in the dissertation it was attempted to perform an analysis using a kinetic-based CFD solver. Despite the other free-access dedicated software for the LBM that are available on the market, such as Palabos [116], SailfishCFD [117], or OpenLB [118] decision was made not to try to interfere with ready-made examples and programming functors - like in OpenLB written in C++ - because that would require many weeks or even months to become familiar with the language syntax and then arduous preparations and validations of obtained solutions for all cases considered in the dissertation. One could be tempted to do it for one specific case with a ready set of boundary conditions, but the parametric studies that are the lion's share of this work exclude the implementation of such a solution.

X-Flow software contains user-friendly and transparent GUI thanks to which it is easy to operate on complex geometry, boundary conditions or live results projecting. Producents delivered many tutorials which allowed for a quick practical learning and made it easier to get familiar with the rules prevailing in entire LBM environment.

Hundredths of simulations were carried out to determine the dependence of TCC on surface descriptors and the applied pressure. The first step was to make a comparison of the mean values of the surface heat transfer coefficients computed from the randomly generated 3D interface models for the interface temperature ranging from 600[K] to 1000[K] with increment of 100[K] to check the general result scatter. Above temperature range represents operational conditions of vane hook and casing component during an aircraft take-off and following cruise flight.

The 3D interface models were reconstructed and analysed for each of the temperature values. For both, top and bottom surface a high temperature steel MAR-M-247 was used. Air was considered as interstitial, static fluid. In order to keep the mesh possible to comprehend within the calculations, the three-dimensional interface model was reconstructed by sampling 25 asperity pairs. For all simulations Ra=5[μm] and d=15[μm] was assumed. Temperature difference of 10[K] was applied across interface to avoid potential nonlinearities in bodies temperature-dependent properties. It is generally recognised that thermal conductivity, density and specific heat varies with temperature for air and steel, therefore it was important to consider that influence in performed computations. Tabulated values of thermal conductivities, specific heats and densities for air and steel are given below.

Air			
Temperature	**Conductivity**	**Specific heat**	**Density**
T [K]	*k [W/mK]*	*Cp [J/kgK]*	ρ *[kg/m^3]*
600	0,046	1051	0,589
700	0,052	1075	0,504
800	0,057	1098	0,441
900	0,063	1120	0,392
1000	0,068	1141	0,353
Steel MAR-M-247			
Temperature	**Conductivity**	**Specific heat**	**Density**
T [K]	*k [W/mK]*	*Cp [J/kgK]*	ρ *[kg/m^3]*
600	300	19,99	8329
700	350	21,58	8254
800	380	23,61	8179
900	460	27,14	8099
1000	550	32,02	8012

Tab. 5.2. Values of thermal conductivity, specific heat and density under different temperatures for air and steel MAR-M-247 [119] [120]

Illustration 5.6 shows an example of the temperature distribution across the three-dimensional interface obtained during steady-state calculations. It can be observed, according to the theory, that heat flow is restricted to flow through the metal contact spots forced by the interspersed air pockets and their lower thermal conductivity.

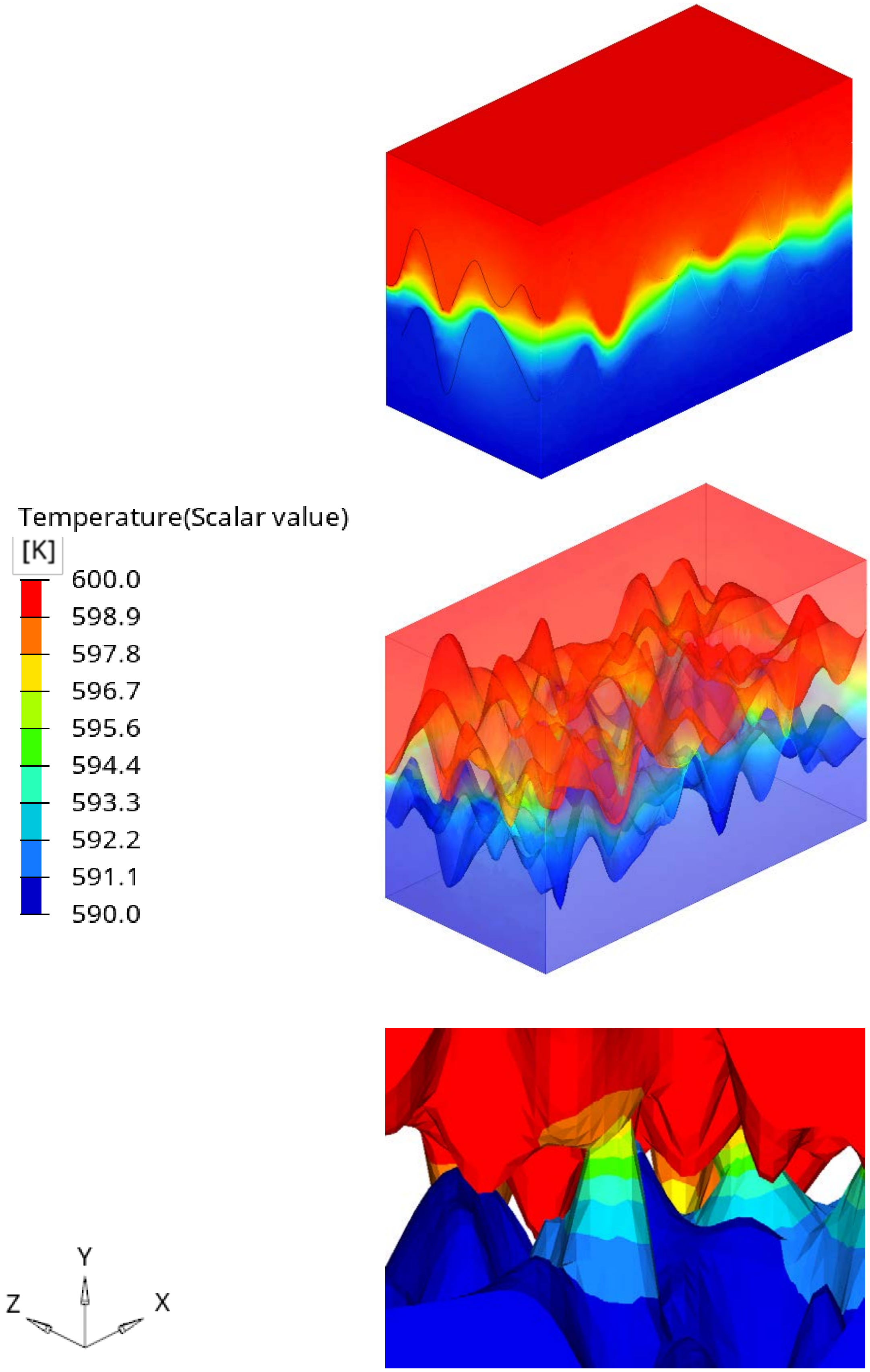

Fig. 5.6. Temperature distribution for three-dimensional steel-air-steel interface model

In order to derive interface effective conductance few steps had to be made. It was first necessary to determine both limit surfaces heat flux average value. Their integrated average output was got from the numerical calculations. Subsequently, the arithmetic value from the two obtained results was determined. Since all side walls were treated as insulators, heat travelled from the top to bottom only, thus integrated over surface average heat flux density was almost identical on both ends. Small differences were purely numerical errors.

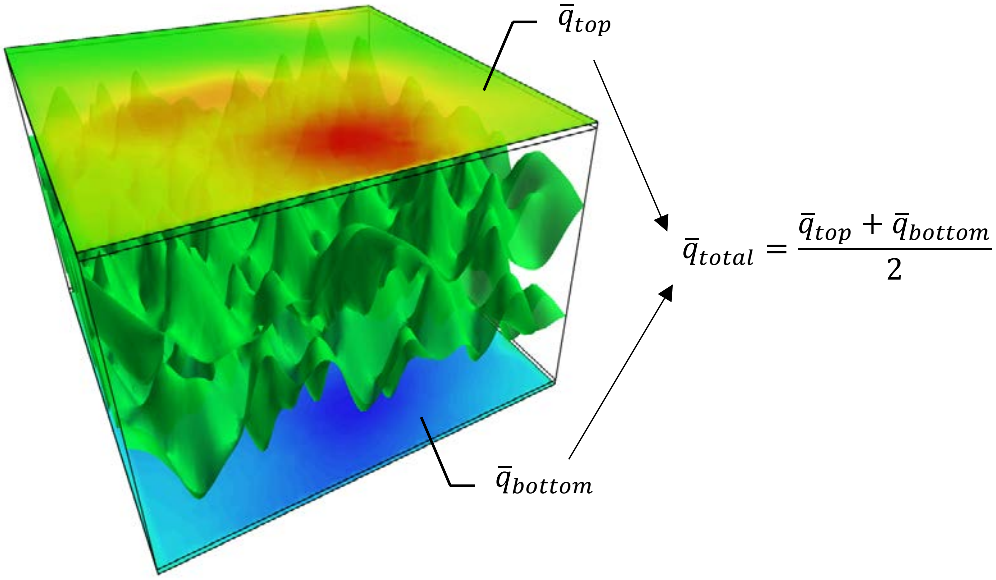

Fig. 5.7. Upper and bottom limit surface heat flux distribution

Next, temperature drop ΔT across the interface was measured by reading nodal values in close proximity of the contact region. Finally, by assuming that the heat flow is one-dimensional, the interface's TCR could be calculated with use of the following formula:

$$TCR = \frac{\Delta T}{\bar{q}_{total}} \tag{5.1}$$

Since, in vast majority of conducted studies their authors report the TCC values instead of the TCR, the reciprocal of Eq. 5.1 along with the TCC term will be used in further considerations to ease legibility of the argument.

The derived thermal contact conductance from steady-state computations for all five ensembles were collected and presented in Figure 5.8.

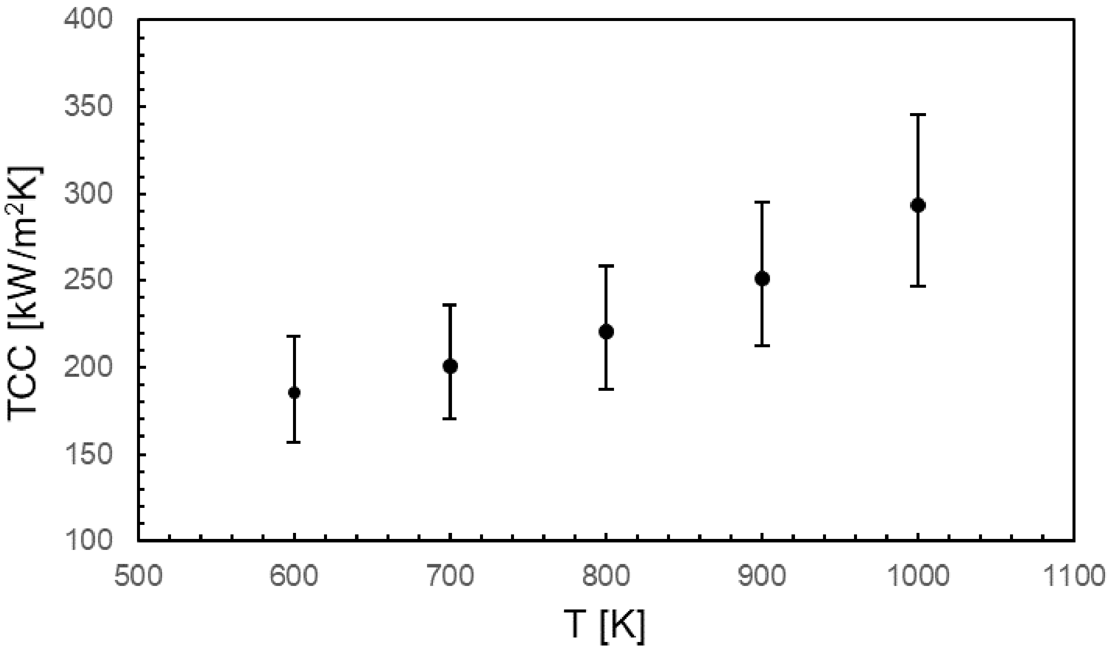

Fig. 5.8. Variation in TCC value with temperature increase for five 3D interface models

Standard deviations from the average TCC value obtained for individual temperatures were as follows:

Temperature [K]	*Mean TCC [kW/m^{2}K]*	*Standard deviation [%]*
600	185,27	13,75
700	201,23	13,60
800	220,51	13,56
900	251,60	13,73
1000	293,30	14,03

Tab. 5.3. Standard deviations of mean TCC value of five reconstructed contact pairs under different temperatures

Based on the above values, it can be stated that despite randomly generated surface shapes, the total dispersion of TCC values for each different temperature was at similar level.

An important thing from the point of view of numerical calculations is always to examine the impact of the mesh size on the accuracy of the obtained results. To check this, a sensitivity study was carried out for one of the contact pairs, changing the size of the tetrahedral element in the fluid and solid domains from 0.5 to 2 [μm]. The results of the obtained average TCC value were presented in the Table 5.4.

Element size [μm]	*Elements number [-]*	*TCC [kW/m²K]*
0.5	9,227,057	153,9
0.75	2,772,711	155
1	1,238,218	156,1
1.5	447,518	160,9
2	307,008	165,9

Tab. 5.4. Sensitivity study results of different mesh sizes and their impact on the TCC value

The data from Tab. 5.4 was presented in the form of the graph below. With use of the exponential function ($y = 149{,}23e^{0{,}0513x}$), a very accurate approximation (R^2=0,9794) of the data series obtained in numerical analyses and extrapolation for neighbouring values of the element size was made.

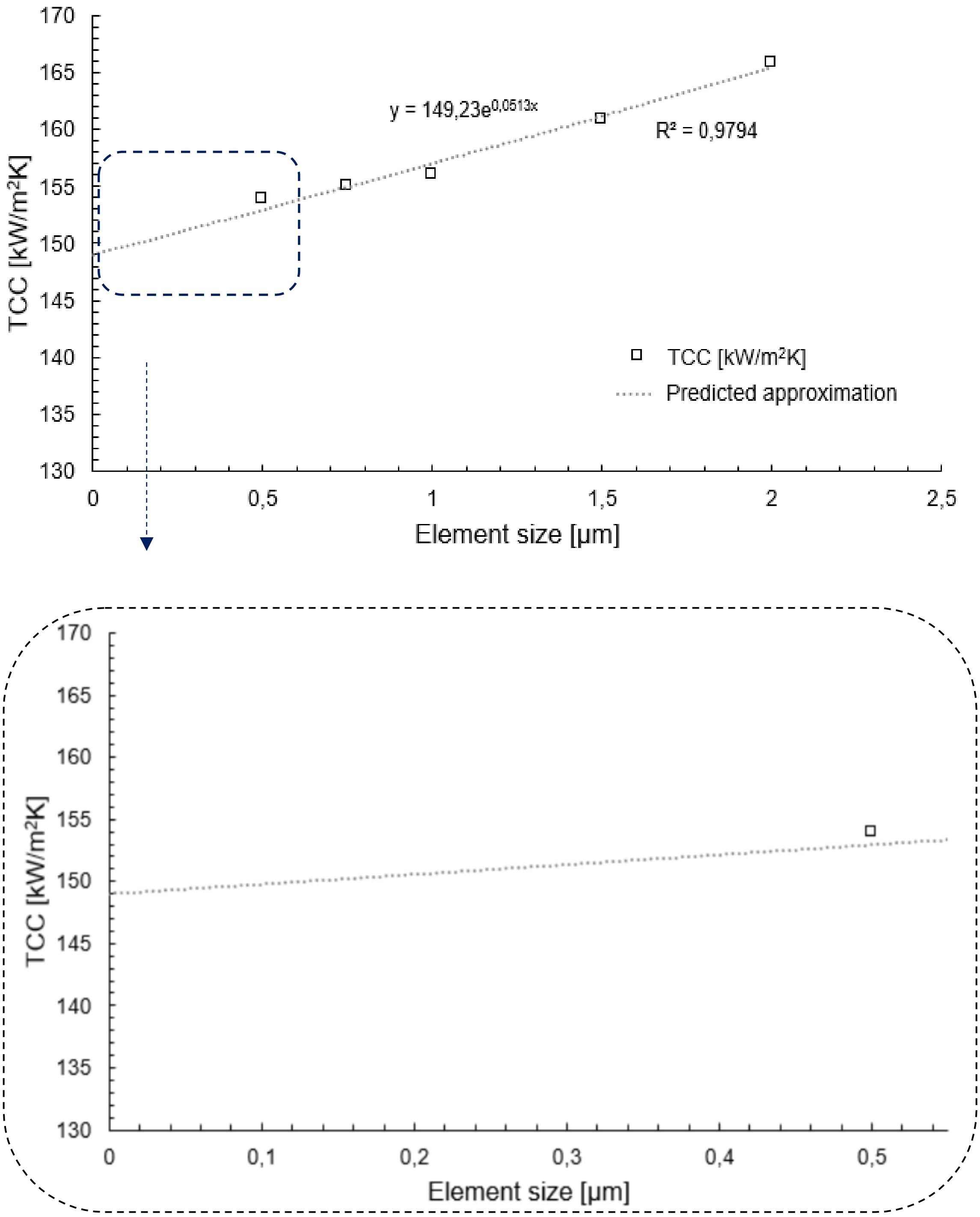

Fig. 5.9. Obtained TCC value depending on the size of the mesh element

An increase in the element size from 0.5 to 1 [µm] changed the TCC value by 1.4%. In turn the element enlargement from 1 to 2 caused a change in the TCC by 6.3%. Thus, it can be seen that the quality of discretization has an impact on the final TCC results. Furthermore, a subsequent change in the size of the element from 0.5 to 0 [µm] showed the linear character of the change captured in the Fig. 5.9 reaching the TCC value of about 149 [kW/m^{2}K]. The problem with smaller elements is their drastically growing number, which extends the meshing and calculation time, parallel requiring more computational memory resources of work station. All analyses were carried out on a workstation with the Intel® Core™ i7-6700HQ 2.60GHz processor and 8GB RAM. Therefore, it was decided that in order to maintain a rational balance between the time needed to prepare the CFD analysis and the quality of results for all calculations carried out in previous and subsequent numerical analyses, a volumetric element with a minimum size of 1 [µm] and growth ratio 1.1 was adopted.

5.3 Heat Transfer Modes Intensity

One of the main aims of the work was to check the influence of heat modes other than conduction such as radiation, natural and forced convection on thermal contact resistance (conductance). For this purpose, separate analyses were performed in which appropriate boundary conditions were set so as to enable to capture each heat transfer mode influence on the total heat transfer distribution.

5.3.1 Radiation

The highly loaded situation was considered to decide whether radiation through air pockets is a prevalent form of heat transfer. In case of no interaction between the two surfaces, the radiative heat transfer rate was contrasted with the overall heat transfer for a 3D interface model. The interstitial air was assumed to be non-participating, and black body emissivity models were defined for both surfaces. The conjugate thermal transport simulation was carried out with a mean interface temperature of 1000[K] applied on top surface and 10[K] less for bottom one. A high temperature of 1000[K] was considered hence the radiative heat flux was enhanced. Because the media under consideration were air (assumed to be 100 percent transparent) and metallic solids (assumed to be 100 percent opaque), the radiation transfer model for surface-to-surface (S2S) was used. Deterministically the S2S model measures the sharing of radiative energy between grey diffuse surfaces using view factors. As well as being ideal for the task at hand, the S2S model was selected because it is the most computationally effective model.

After calculation was done the radiative heat flux was about 14[%] of the total heat flux of the system. It was also decided to check what will happen when the temperature delta is close to 100[K], which is the case for the weak or moderate contacts. The effect of radiation in this case was 32[%].

On the one hand, these results can be considered as having a partial effect on heat exchange and that they should be included in the TCC calculations, however, with interfaces consisting of connection areas, the proportion of the surface area involved in the transmission of radiation through the air pockets is much smaller. In fact, the emissivity of metals being in contact in real turbine engine is smaller than the ideal emissivity of the black body (app. 1/3 lower). Therefore, the contribution of radiation to the overall thermal transport across the interface is deeply under consideration border and may be neglected.

5.3.2 Free Convection

The effect of natural convection was determined by the Grashof criterion number. Based on the effective width of the distance (from 10 [μm] to 30 [μm]) between the surface pairs, Grashof number values were found to be very small, approximately 10^{-5}. Therefore, one can easily ignore the free convection in the air pockets. Additionally, even for the smallest separation distance considered (d=0), the average size of the mesoscale air pockets equal ~10[μm] which is few orders of magnitude higher compared to the mean free path of air which is 64[nm] at standard temperature 288.15[K], pressure 101325[Pa] and humidity 0% regarding to [121].

As a result, for the air trapped in the pockets, the Fourier’s law of heat conduction is completely valid.

5.3.3 Forced Convection

To check the effect of forced convection on heat distribution in the micro-flows, two numerical approaches were used: the classic CFD method taking into account fluid domain discretization and the approach exclusively described in Chapter 4 the Lattice Boltzmann Method.

Each of the methods has its own rules, assumptions, boundary conditions and code execution guidelines. Demonstration of forced convection using LBM serves to emphasise the possibilities of the method different from the one commonly used and to shed light on its strengths and weaknesses in issues of thermal flow through complex geometries.

5.3.3.1 Classical CFD Approach

The preliminary validation of the method was done by using the classical CFD approach with simultaneous investigation of the forced convection impact on the TCC. The findings of the numerical thermal model of the turbine engine were used as reference values. For a representative case in this analysis, a contact between the front vane hook and low-pressure turbine casing with accompanying take-off phase operational conditions was selected. During the take-off phase of the aircraft from the ground and its subsequent climbing, the engine components are subjected to the largest thermomechanical loads hence its choice. The microscopic fragment of reconstructed surfaces with assigned boundary conditions typical for take-off conditions has been presented below.

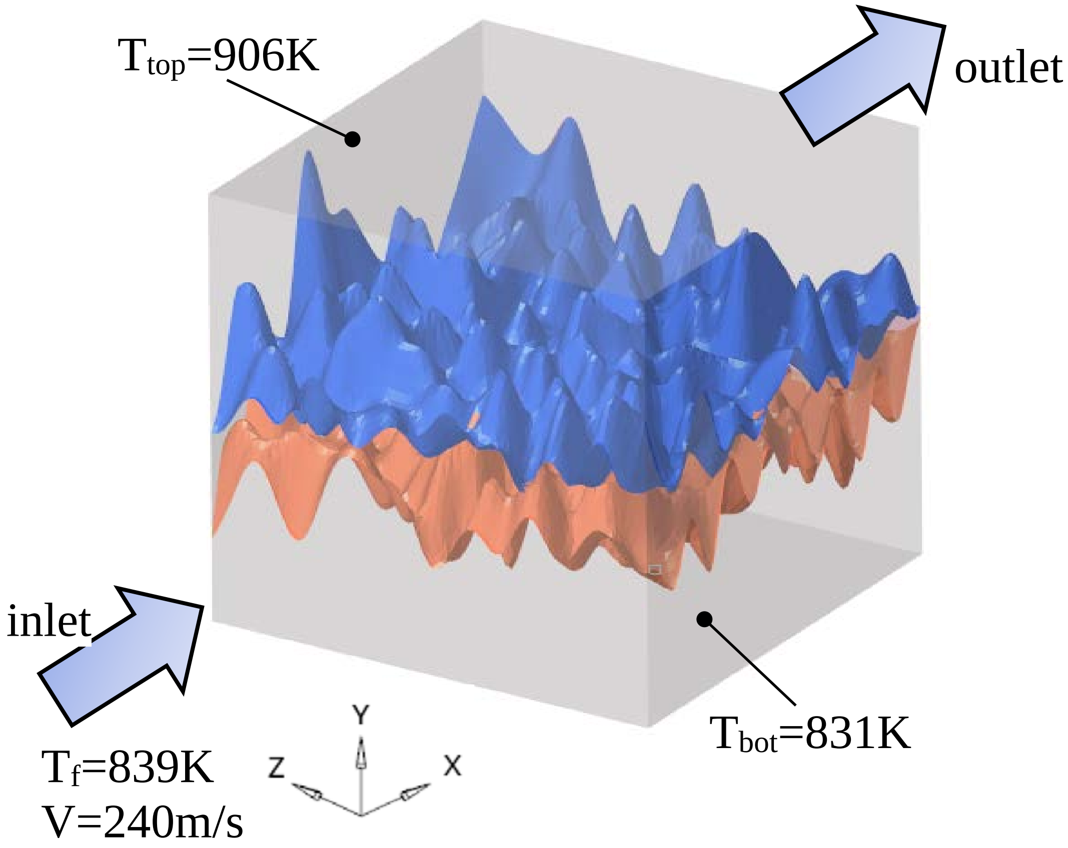

Fig. 5.10. Reconstructed surfaces of low-pressure turbine casing and front vane hook

The one-equation Spallart-Almaras turbulence model [122] was adopted for the analysis purposes. There are two main factors which decided to use this model for given operating conditions discussed in this chapter:

I. The S-A model involves the solution of only one transport equation for kinematic turbulent viscosity. Consequently, the computational effort is lower compared to the commonly used two-equation models like k-epsilon or k-omega.

II. Furthermore, this is the only RANS (actually uRANS) turbulence model used also by XFlow. Thus, it has a function of a bridge between the different calculation methods of the fluid mechanics presented in the dissertation.

Because of the above and the success of the model due to its robustness, fast execution when modelling complex flows, as well as not demanding high memory resources along with achieving strong convergence, the S-A model was chosen for simulation purposes.

The compressibility effect was omitted due to its practical absence for the geometry under consideration and acting boundary conditions. T

The separation distance was 5[μm] which roughly corresponds to the pressure of the order of 1[GPa] that is found in this region. The estimation process of the separation gap will be more precisely presented in Chapter 5.4.

The results of thermal steady-state analysis are shown in Figure 5.11 where the distribution of heat transfer coefficient was presented for the bottom and top surface.

The average value of the heat transfer coefficient was 90.4[W/m^{2}K].

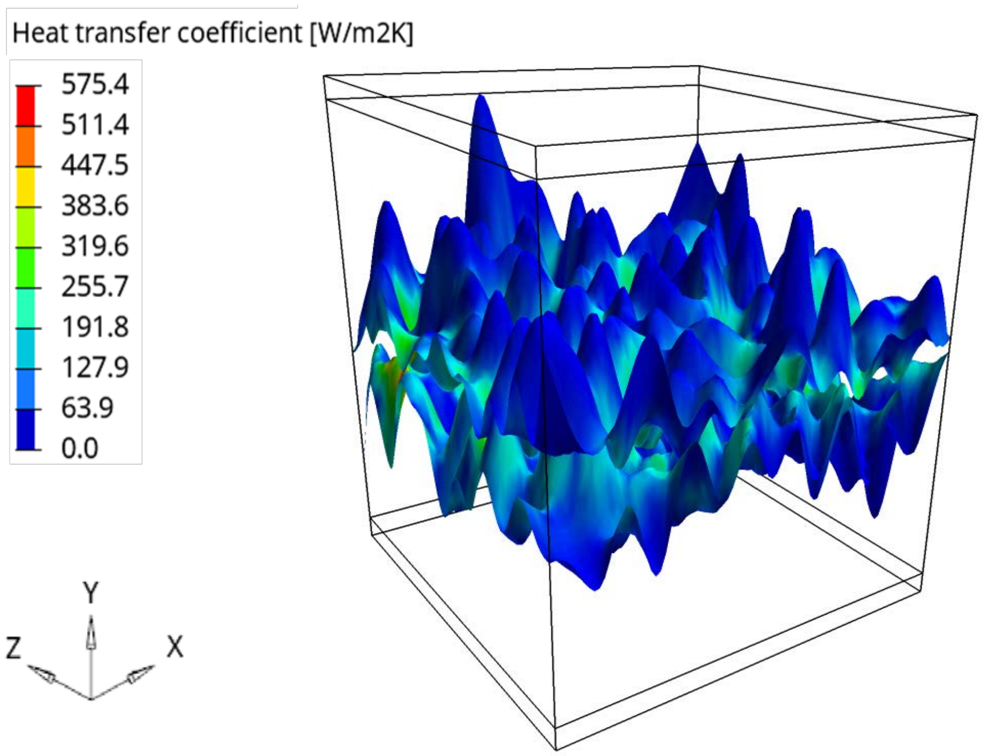

Fig. 5.11. Heat transfer coefficient distribution for low-pressure turbine casing and front vane hook connection

For the discussed case, an additional analysis was made taking into account only the heat flow from the top to bottom surface, excluding forced convection computation. Based on the results, it was found that the effect of forced convection changed the value of HTC only by 6[%]. Hence, as the effect of flowing fluid with a temperature close to the temperature of both surfaces it does not play a such significant role in the overall thermal contact resistance settlement, thus it was decided to check the change in fluid temperature and its effect on HTC at constant surface temperatures. The analyses were performed from 600[K] to 1000[K] for the temperature of the flowing medium with applied increment of 100[K], additionally taking into account the change in air thermophysical properties. The selection of the above boundary conditions was made due to the fact that these are typical values accompanying the contact of vane hook and turbine casing during the take-off of the aircraft and its further cruise phase of flight. The following table shows the results of analyses of the average surface HTC for the change of the medium temperature.

Fluid temperature [K]	*Mean HTC [W/m^{2}K]*
600	109,4
700	101,9
800	90,4
900	86,2
1000	81,5

Tab. 5.5. Mean heat transfer coefficient value variation for the temperature changes of flowing air

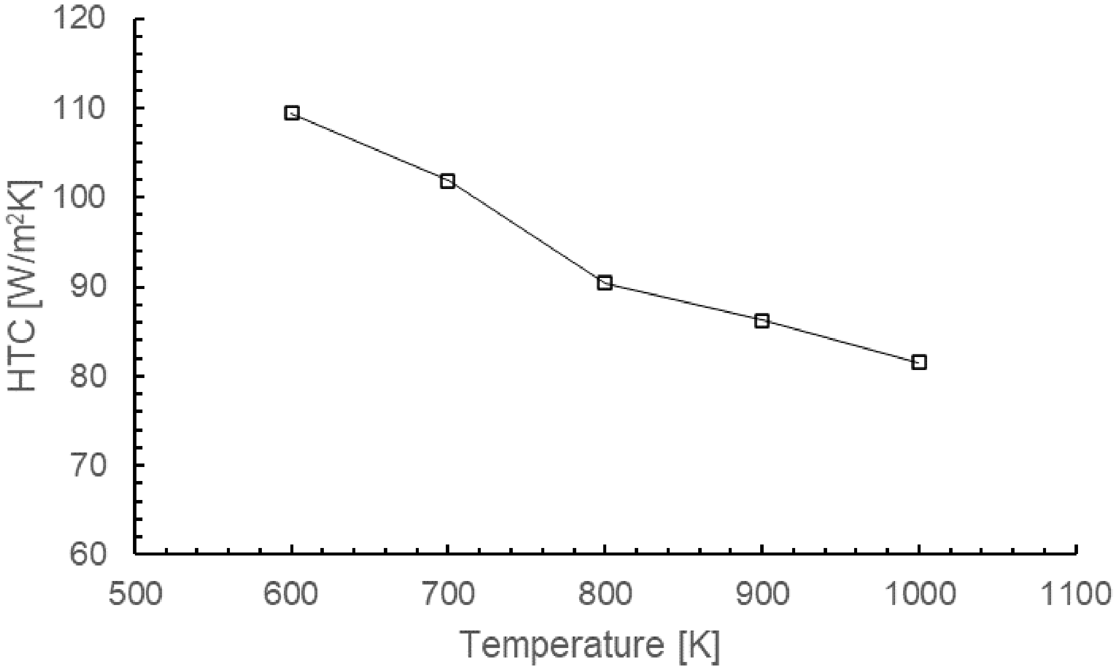

Fig. 5.12. Mean surface HTC in function of air temperature

Based on the above results, it can be seen that at a constant temperature of the contact surfaces, an increase in the temperature of the flowing air causes a slight decrease in the heat transfer coefficient on the surface. For the fluid temperature range between 600 and 1000[K] overall scatter for HTC is equal 28[W/m^{2}K] and it is purely resulting from the wall heat transfer equation (Eq. 3.1). Through increasing the value of the denominator at which the temperature of the fluid and the metal (which is constant) is recorded, the value of the heat transfer coefficient is reduced. Therefore, in the case of a medium such as air and metals with very low thermal conductivity, the convective heat transfer in the thermal contact resistance phenomenon may be completely omitted.

5.3.3.2 Lattice-Boltzmann Method Approach

The simulated forced convection was also carried out using the Lattice Boltzmann system in order to verify the behaviour of the moving fluid in the interface gap and to state if in the mesoscale exists any phenomenon not observable in the classic CFD approach. The identical flow case with exactly same boundary conditions like in Chapter 5.3.3.1 were used to run the simulations using particle-based kinetic solver XFlow.

In XFlow the conjugate heat transfer analysis is performed simultaneously by solving for solid conduction and fluid convection. The solid geometry set as conjugate heat transfer must be watertight volume and the normal must be point outwards. Solid has to have specified same thermo-physical parameters inputs like in the classical CFD approach i.e.: thermal conductivity, initial temperature law, specific heat capacity, density and optional volume heat. CHT is only available for fixed and enforced geometries.

A precisely identical geometry to that used in the classic CFD approach was introduced into the virtual wind tunnel used by XFlow environment. This virtual wind tunnel consisted of a rectangular domain with dimensions of (0.1 x 0.05 x 0.05) [mm]. A far-field velocity boundary condition was used at the inlet, upper and lower boundaries, and zero gage pressure was applied at the outlet. Periodic boundary condition was set on the side walls.

The collision operator used in XFlow is based on the multiple relaxation time scheme presented in Chapter 4.3.5.3. However, as opposed to standard MRT, the scattering operator is implemented in central moment space. The relaxation process is performed in a moving reference frame by shifting the discrete particle velocities with the local macroscopic velocity, naturally improving the Galilean invariance and the numerical stability for a given velocity set. The simulation time was equal 10 seconds with the time step 9.94827e-06[s] which was automatically estimated by XFlow to ensure the numerical stability.

Since LBM is a CFD technique based on particles it does not require a time-consuming meshing process. For each geometry the pre-processor produces the initial octree lattice structure based on the shape of the input file and the user-specific resolution.

The lattice can have many layers of description that are organised in ordered hierarchy and solves spatial and temporal scales that are two times smaller than the previous layer. The solver has also the ability to modify the lattice structure later if the computational domain changes i.e. due to the presence of moving parts or if the resolution changes dynamically to adapt to the flow patterns so-called adaptive wake refinement. In the analysed example far-field lattice resolved scale was equal to 0.01[mm] along with the static wall target resolved scale equal $7{,}81*10^{-5}$[mm].

As in the classical CFD approach, the Spallart-Almaras turbulence model was used for the LBM analysis. In the case of turbulence, a thing worth mentioning is also the fact that the lattice is automatically refined in the lattice elements where the vorticity reaches the threshold value. Similarly, eight neighbouring lattice elements are combined to create a coarser lattice product when the vorticity is smaller than another threshold. This saves strongly computational resources and eliminate the need to manually refine the domain’s structure.

The temperature is calculated from the energy equation which is modelled according to the following sensible-enthalpy conservation equation:

$$C_p \frac{D(\rho T)}{Dt} = \nabla \cdot (k \nabla T) + \nabla \cdot (\tau \cdot \vec{v}) - p \nabla \vec{v} \tag{5.2}$$

Where: C_p is the specific heat capacity, ρ is the density, T is the temperature, k is the thermal conductivity, τ is the viscous stress tensor, $\vec{v}$ the velocity vector and p is the pressure field.

The last term in the Eq. 5.2 represents the influence of compressibility effects. However, for the analysis the so-called segregated energy thermal model was used. That means that the energy equation is solved without the compressibility term and buoyancy effects are included in the flow-motion equations using Boussinesq approximation. Heat transfer coefficient is estimated basing on well-known macroscopic wall heat transfer (Eq. 3.1).

In XFlow fluids are considered as non-participating media by default. Therefore, radiation source term is not accounted for in the energy Eq. 5.2. However, XFlow do consider S2S radiative heat transfer model, which is modelled according to Montecarlo model. But to save consistency between classic CFD and LBM approaches, radiation was not applied in the LBM model.

The following illustration presents the wind tunnel domain consisting of levels with the following number of elements:

- Level 0 has 25 active elements,
- Level 1 has 600 active elements,
- Level 2 has 4398 active elements,
- Level 3 has 21338 active elements,
- Level 4 has 162224 active elements.

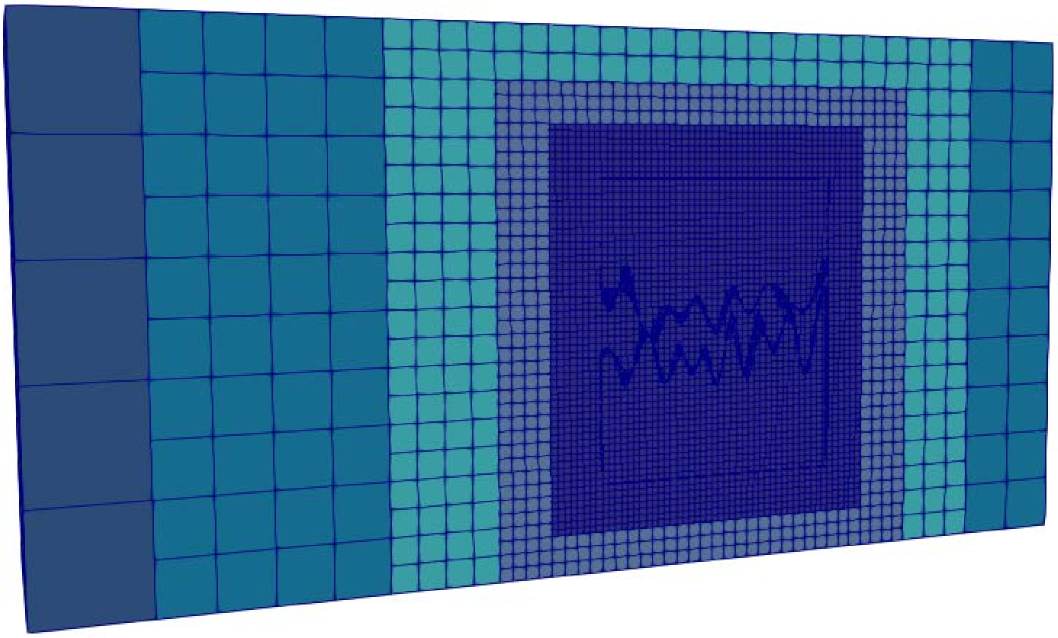

Fig. 5.13. Computing domain divided into five octree levels

On next figures, the mesh compaction alongside the geometry as well as the distribution of the surface heat transfer coefficient obtained by LBM analysis were presented.

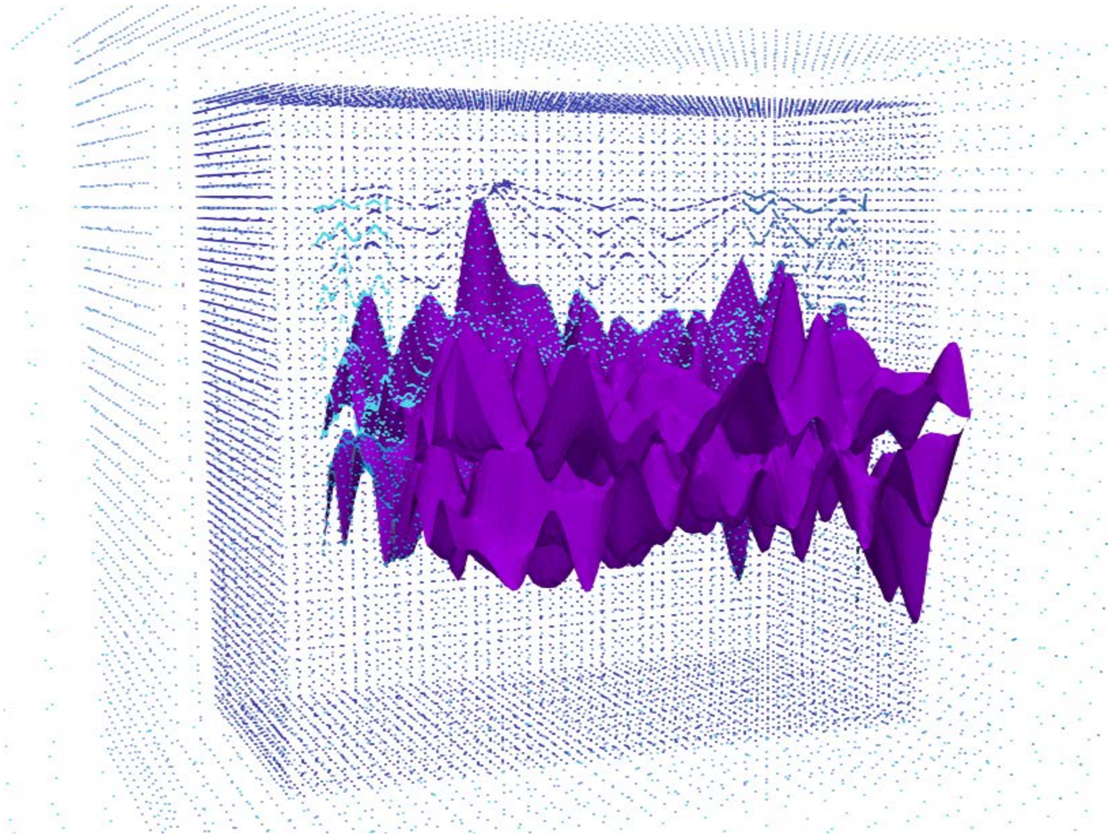

Fig. 5.14. Spatial arrangement of computational elements surrounding the static walls of two contact surfaces (side walls suppressed)

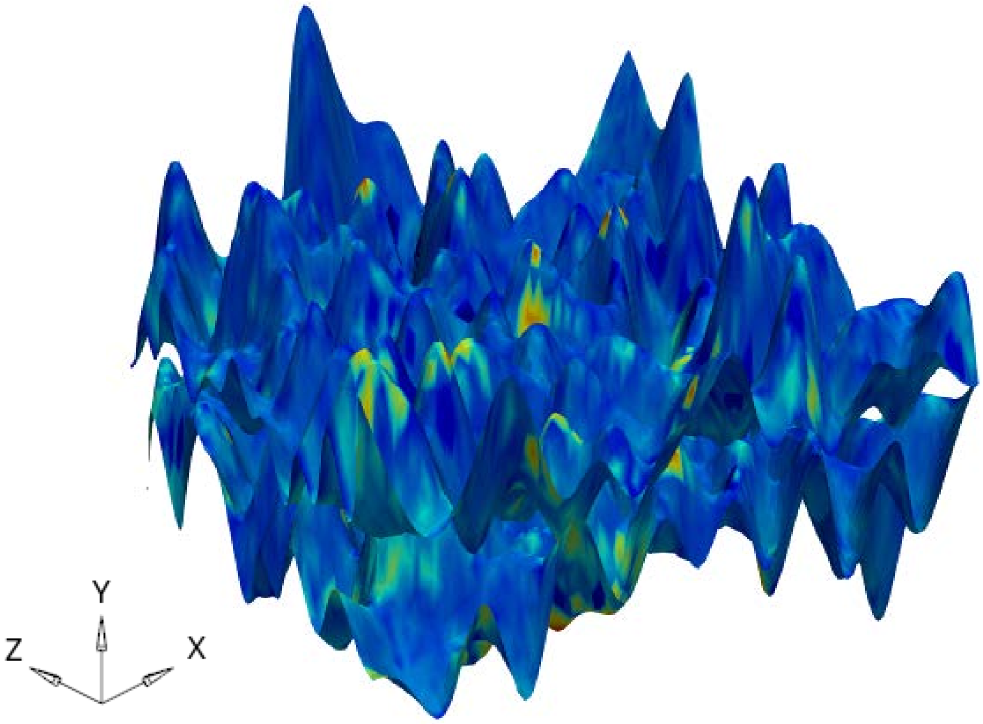

Fig. 5.15. Heat transfer coefficient distribution on surface obtained by LBM simulation

The average value of the heat transfer coefficient was 92.7[W/m^{2}K], which is very similar to that obtained in Chapter 5.3.3.1. The differences in the distribution of the heat transfer coefficient on the surface between the classical CFD and those obtained with the LBM are directly derived from the nature of each of the methods, i.e. the static tetrahedral mesh in which the energy equation is solved, and the more "chaotic" propagation and mutual collisions of air molecules. The increase in local values is directly linked to the impingement on given surfaces of these particles.

The decision to present under different point of view the method dealing with flows in micro-gaps resulted from the need to demonstrate of the all benefits that other CFD methods bring. Using traditional CFD software, many of industrial problems require time-consuming meshing process which often leads to errors or even divergence of the simulation. To handle mesh creation its improvement and refinement separate departments in many companies are built to focus solely only on this topic. Thanks to XFlow and its particle-based and fully Lagrangian approach, the complexity of the geometry surfaces is no longer a limiting factor, even in the presence of moving parts, allowing to solve complex industrial problems. Furthermore, the time required in XFlow to set up the case is about 10 minutes and mainly consists of geometry import, the flow and boundary specifications, and the resolution setup. On the other hand, its disadvantage is quite a long calculation time, which for the above case was about 4 hours. Nevertheless, in authors opinion, methods similar to the above, may serve as the core in the field of microfluidics in the nearest future.

The general problem under consideration, is not too complicated from the point of view of numerical and classic mechanics, since we do not deal here with any geometry acceleration, thrilling turbulence effect, sophisticated multiphase flow, etc. It is pure aerodynamic stream flow combined with thermal analysis. Thus, in such a realistically simple situation, the potential of the presented approaches cannot be completely emphasised.

Thanks to the micro-gap studies, the author was able to obtain awareness of the topic and confirm from the mesoscale viewpoint that not much happens if we go one floor down with scale. This indicates that the usage of macroscale CFD instruments to study the aero-thermal can be accepted if all restrictions regarding boundary conditions are met and the surface geometry is appropriately handled. The utilisation of innovative methods based on particle-based solvers also shows the credibility and acceptability of the results, which is also satisfying.

5.4 Method Validation

Pre-validation in Chapter 5.3 was conducted on the basis of a low-pressure turbine thermal model with help of two separate computational approaches. However, in order to fill the curiosity void and achieve relative confidence as to the accuracy of the process, the method was also confronted with the experimental results available in the literature.
The computed TCC values were compared to the values recorded experimentally by A. Tariq [123]. In his work, bench tests were carried out to examine the axial heat flow and the effect on the TCC value at interface under vacuum conditions. Three different contact pairs made of copper, brass and stainless steel were tested with various roughness values (1-5 μm). In the experiment the samples were subjected to contact pressure for which the values changed from 0.6 to 15[MPa], thus in order to proper reflect the conditions prevailing in it, it was necessary to implement an additional variable in the numerical model.

The effect of the pressure boundary condition was modelled indirectly with modification of the separation distance, between the mean planes of the contacting surfaces. It was done instead of the necessity of reconstruction of the interfacial structure between two pressurised surfaces. Such model considers only the thermal part from the general thermo-mechanical problem and assumes that the mechanical nature of the model (pressure vs. displacement) is already known.

Singhal et. al. model [124] was used to calculate the separation distance depending on the contact pressure. Firstly, dependence values between pressure and separation distance were extracted from authors obtained data and then by matching the logarithmic function additional five separation distances for given loads distinguished in Tariq’s work were estimated. The table 5.5 presents variation of the distance between mean planes as a function of pressure.

Pressure [MPa]	*Separation distance [μm]*
0,6	33,81
5	25,66
8	23,85
12	22,29
15	21,43

Tab. 5.5. Separation distance in pressure function computed basing on Singhal model [124]

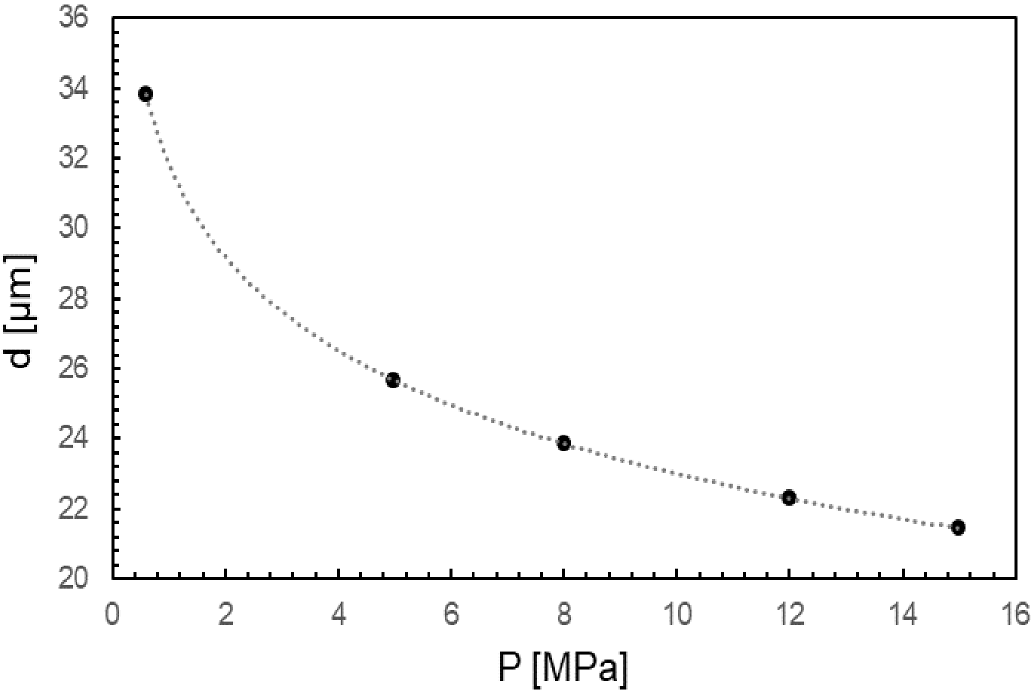

Fig. 5.16. Dependence of separation distance as a function of contact pressure, experimental values for validation

The Singhal model has been tested for a pressure range of 6[MPa]. The author is aware that the extrapolation of data to measurement points from the Tariq et. al. it is very risky and burdened with a high value of uncertainty, but apart from building an experimental facility and conducting a research for specific contact pairs and different pressure values, it is impossible to measure their values more precisely. Hence, a decision was made to adopt the presented model, which will indirectly simulate the mechanical part of the thermal contact resistance phenomenon.

For the purpose of classical CFD analysis validation, the contact between two copper block specimens (99% pure) with given in the paper dimensions and of equal roughness varying from 1.07, 1.57, 2.02 and 2.82[μm] was considered. The following material properties were adopted:

Copper (99% pure)		
Conductivity	**Specific heat**	**Density**
k [W/mK]	*Cp [J/kgK]*	ρ *[kg/m^3]*
398	376	8960

Tab. 5.6. Values of thermal conductivity, specific heat and density for copper [125]

Experimental setup and the steady-state TCC values measured experimentally for the copper pair as a function of the applied pressure are shown in Fig. 5.17 and 5.18.

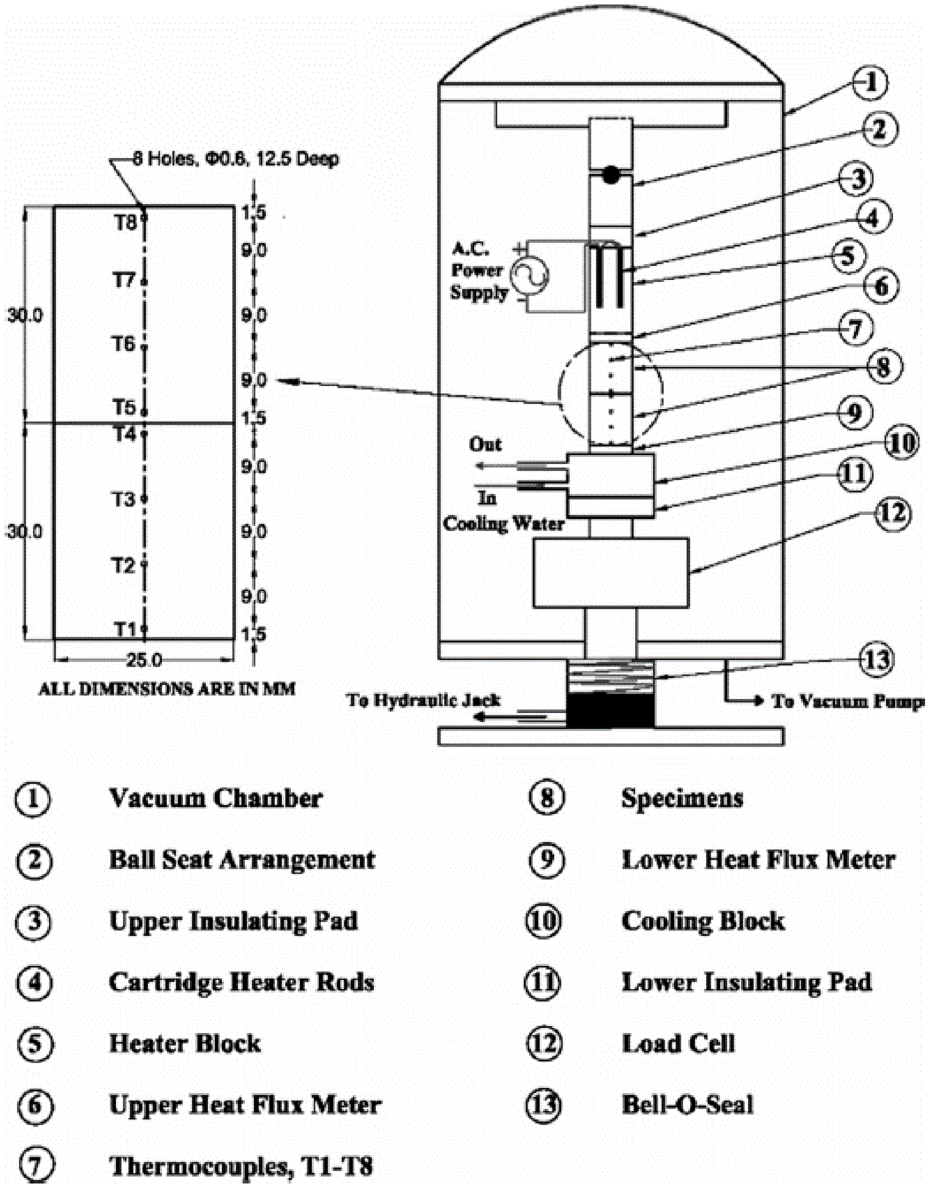

Fig. 5.17. Schematic view of A. Tariq [123] experimental setup and thermocouples position in the specimens

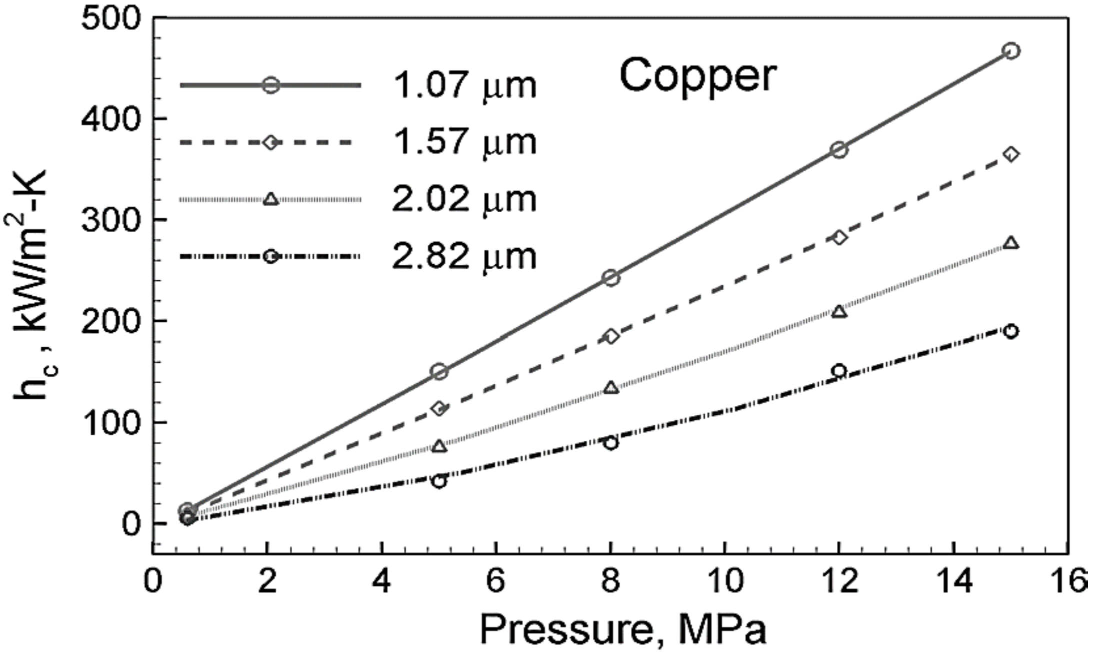

Fig 5.18. TCC versus pressure, experimental data used in the validation study [123]

The results were confronted with the already existing analytical correlations. Below is the result of this confrontation with the Mikic model [35]:

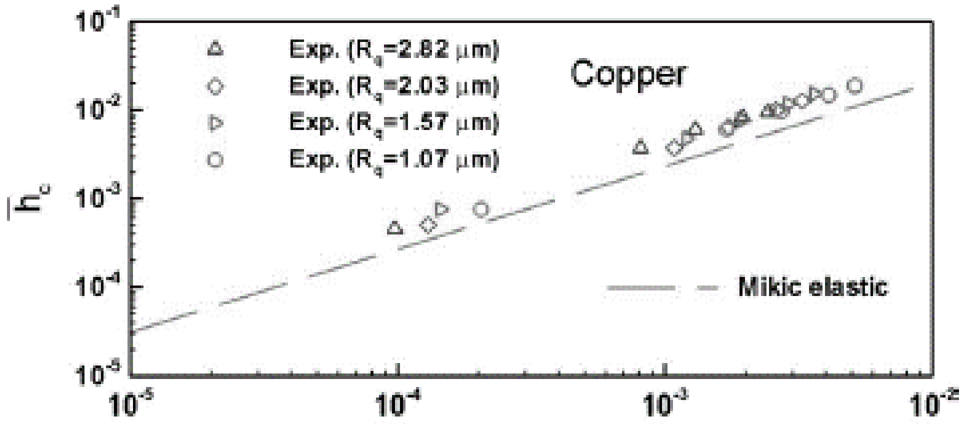

Fig. 5.19. Thermal contact conductance compared with the Mikic [35] experimental model based on the principle of elastic deformation for copper

The major source of uncertainty in the estimation of TCC was due to the heat losses, errors in heat flux estimation, errors in the estimation of temperature drop at the interface, and positional inaccuracy of the thermocouple’s instalment. The overall uncertainty for the estimation of TCC has been determined on the basis of law of error propagation and it was found that maximum value of uncertainty equals 24.3[%] for copper specimens.

All roughness cases were tested for the PhD method validation purposes. After reconstructing the surface geometries, the boundary conditions corresponding to the temperature values obtained during the measurement of thermocouples near the interface were assigned and 1D transfer of heat was simulated.

As the medium in the experiment was a vacuum, and numerical solver AcuSolve makes it impossible to define it explicitly, the whole fluid domain remained discretised, but the specific heat value was raised by an exponent of 20, and the conductivity was reduced by the same amount, thereby following the vacuum assumptions. The results obtained after the simulations were summarised in Fig. 5.20.

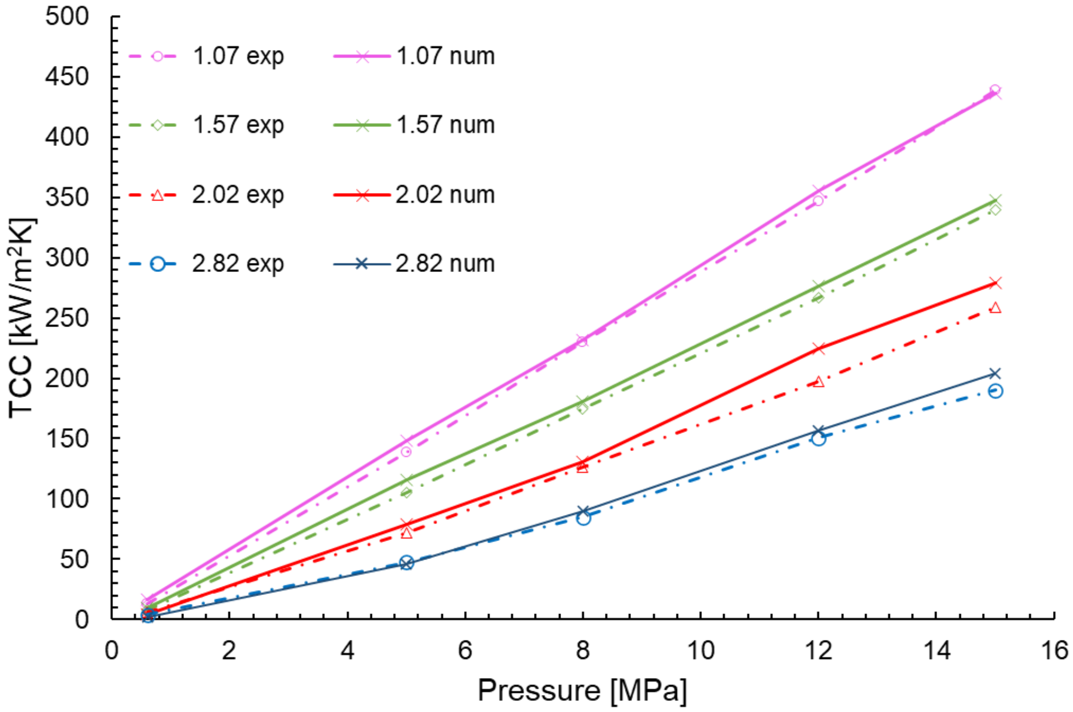

Fig 5.20. Comparison of TCC values in function of pressure for experiment and numerical analysis with differences for individual measurement points

As can be seen, the observed numerical outcomes were found to be in very close alignment with the experimental data. The average TCC difference levels were 1.9, 4.8, 8.1, and 4.4[%] respectively for 1.07, 1.57, 2.02, 2.82[μm] of surface roughness. Therefore, basing on this and taking into account experiment uncertainty the presented procedure was considered to be accurate for a specified set of temperature boundary conditions and different surface roughness.

Owing to the absence of reported experimental data of the flow through microchannels, validity of the LBM computations has become elusive. Measurement of the required values at the microscopic level has not been presented in any of the papers, thereby preventing validation of the method itself. Software developers, however, ensure that testing experiments have been carried out for several other experimental cases, such that it is appropriate to presume in advance (and with some scepticism) that the outcomes and distributions produced by their solver for the microflows actually take place. Nevertheless, forced convection itself, as a form of heat exchange, still does not play such a key role in thermal contact resistance phenomenon if the temperature difference between the components and the moving fluid is similar as in the aircraft turbine engine regions under dissertation considerations.

5.5 Probability of Contact

Using surface descriptors such as mean arithmetic roughness and separation distance in a pressure function it is possible to determine whether and in what number a contact between two surfaces will occur. Despite the fact that the real contact area at high pressure values approaches only 1-2[%] of the apparent contact region, conduction across surface asperities plays a dominant role in the transmission of heat, thereby the TCC value. Therefore, it is important to estimate the amount of contact spots coming from the process of stochastic surface generation. The Python script includes a variable that probes the points of the surface height, but the places of mutual contact of the solids can only be determined after the surface pair is generated and checked by manual counting. Therefore, a basic statistical method was employed to quantify the amount of asperities that could be tested a priori.

For a prescribed separation distance, interaction between two asperities exists only if the total of the asperity pair heights is equal to or greater than its value. The probability of contact between two surfaces can thus be expressed as:

$$Prob(z_1 + z_2 \geq d) \tag{5.3}$$

In order to know the value of such expressed probability, the script uses an algorithm that calculates the cumulative distribution function from the sum of the heights of the transformed form of the above equation:

$$1 - Prob(z_1 + z_2 < d) \tag{5.4}$$

Using equation 5.4, the potential number of surface contacts was calculated multiplying the observed probability values by the sampling number. For both surface roughness it was equal 5[µm]. Obtained data can be seen in Table 5.7.

Separation distance [μm]	*CDF Contact probability [-]*	*Number of contacts [-]*	
		10^4 Samples	*10^3 Samples*
33,81	0,008	1	0
25,66	0,230	23	2
23,85	0,419	42	4
22,29	0,677	68	7
21,43	0,867	87	9

Tab. 5.7. Probability of contact spots occurrence in function of separation distance

In addition, the cumulative distribution function plot for the lower surface is presented in Fig. 5.21, from which the pure Gaussian distribution of asperities on the surface can be seen.

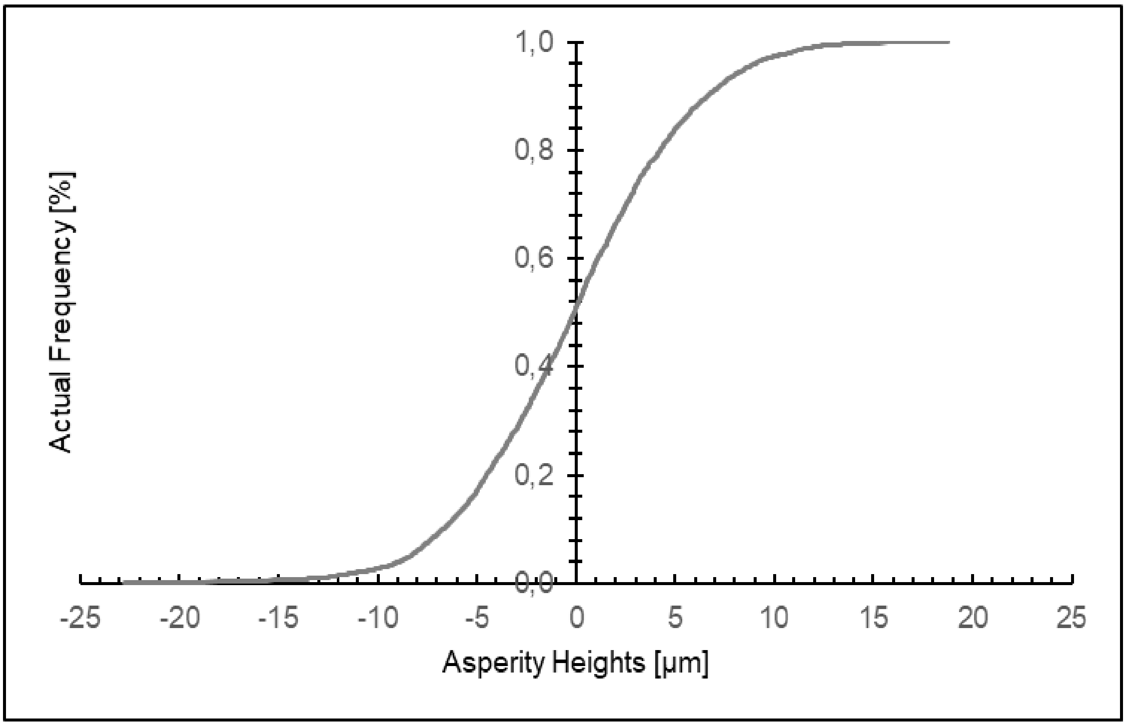

Fig. 5.21. Cumulative distribution function for one of the contact pair surfaces

On the basis of the aforementioned results, it can be clearly stated that as the contact pressure increases simultaneously the distance between the surfaces decreases, consequently raising the number of contact points. In addition, a significant difference between the contact points and the number of samples of roughness height can be inferred. It is therefore so necessary to preserve a certain equilibrium in simulations because of the increasing number of elements needed to reconstruct surfaces and subsequent computational fluids and solid domains. In order to eliminate complexities during all numerical analyses related with memory allocation, an effort was made to maintain the amount of samples constant at 10^3 level.

5.6 TCC Correlation

As already discussed in previous chapters, TCC largely depends on the geometrical properties of the surface, which are often not taken into account or overestimated by engineers in many industries. In this chapter a solution will be proposed in the form of the correlation enabling the determination of the TCC value depending on the two main surface descriptors - roughness and separation distance related with contact pressure.

Several simulations have been carried out for various contact pairs generated with surface reconstruction script. Top and bottom surfaces had a constant value of temperatures, 600[K] from above and 590[K] from below. MAR-M-247 was adopted as the solid material while the space between the pairs was filled with the air. The results obtained for the above assumptions are presented in the chart below.

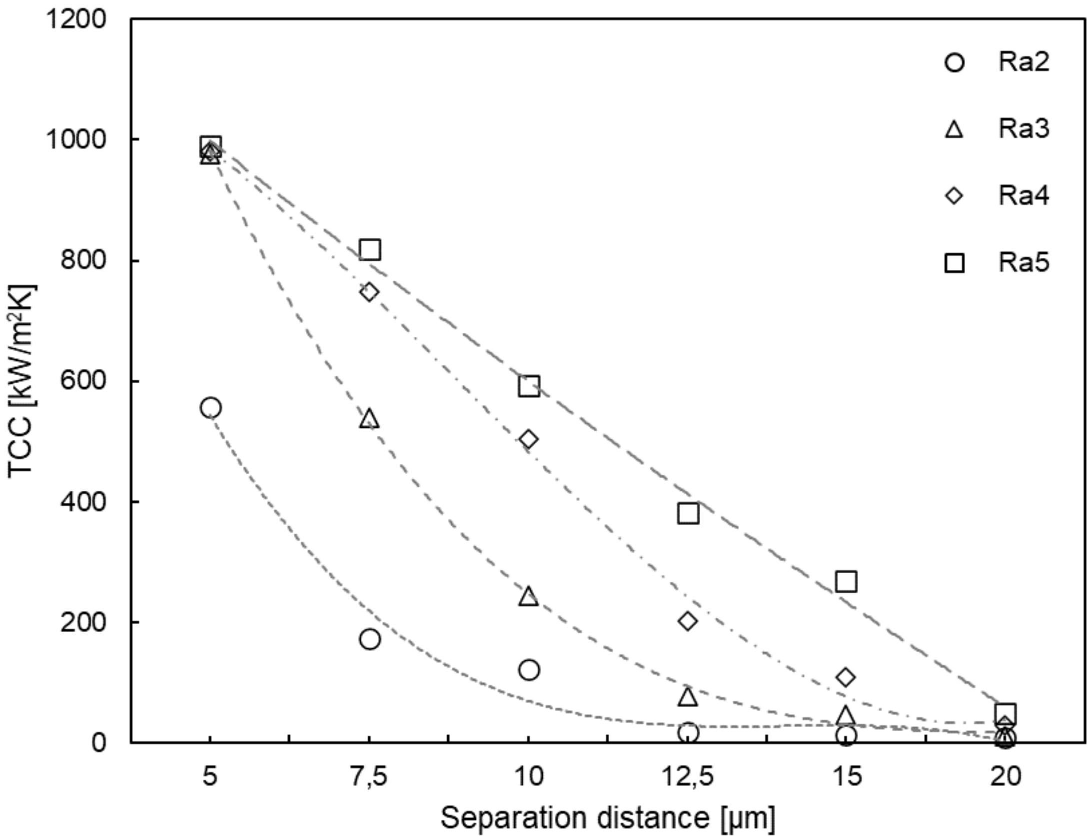

Fig. 5.22. TCC in function of separation distance and surface roughness

The values obtained reflect well the theory presented in the dissertation. A characteristic increase in the TCC value with simulatenous decrease in the separation value and a change in the roughness value can be observed. Also worth noting is the change in the nature of the approximation of the distribution for different roughness values from linear for Ra=5[um] to hyperbolic for Ra=2[um]. MATLAB software [126] was used to check this estimation more specifically. Software provides a CurveFitting toolbox which contains a graphical user interface (GUI) that allows to perform specialized statistical and data-fitting operations. Polynomial regression method [127] was used to get the best fit by minimizing the sum of the squares of the deviations of the calculated values from the data. Polynomial model curves are given by:

$$y = \sum_{i=1}^{n+1} p_i x^{n+1-i} \tag{5.5}$$

where: n +1 is the order of the polynomial, n is the degree of the polynomial, and is between $1 \leq n \leq 9$.

The order provides the number of coefficients to match, and the degree gives a highest power of the predictor variable.

By using polynomial regression technique in MATLAB CurveFitting toolbox, it is possible to adjust the sampled data with second, third and even higher-degree equations. As expected, the more terms the equation contains, the "better" the fit, at least in the sense that the distance between the measured and predicted data points decreases. Polynomial model utilises the least squares method which is a statistical procedure to find the best fit for a set of data points by minimizing the sum of the offsets or residuals of points from the plotted curve. The main advantages of polynomial fits include reasonable flexibility for data that is not too complicated (scattered). The main disadvantage is that high-degree fits can become very unstable. Additionally, polynomials of any degree can provide a good fit within the data range, but can diverge wildly outside that range. Therefore, it is important to preserve certain caution while performing any extrapolation.

Below output charts from the surface fitting of the results obtained in numerical analyses, along with the TCC contour plot in two-dimensional space and a map of residuals for individual data point were presented.

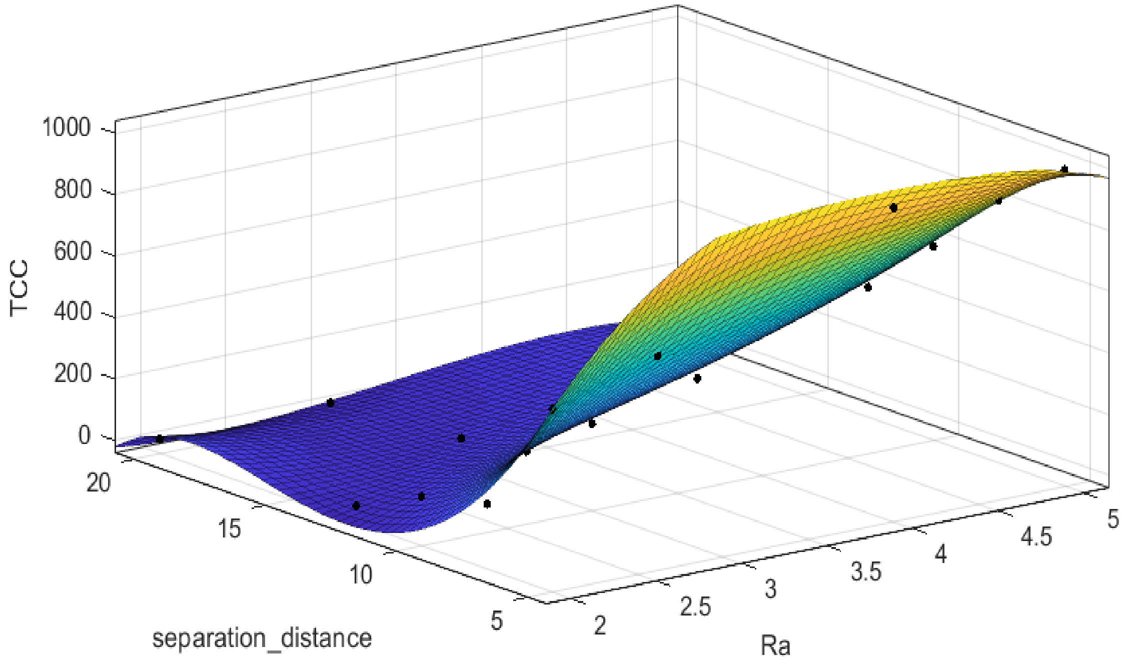

Fig. 5.23. Polynomial surface fit of TCC numerical data

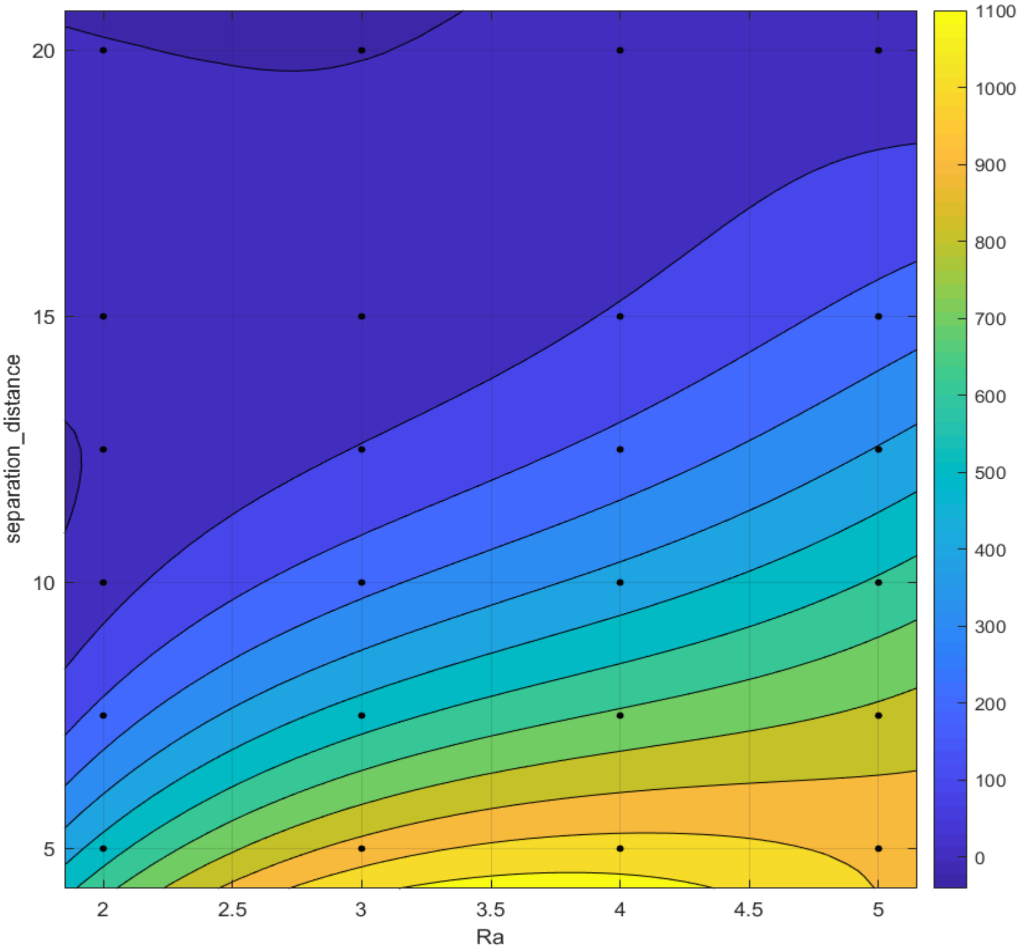

Fig. 5.24. Contour plot of TCC values as a function of surface roughness and separation distance

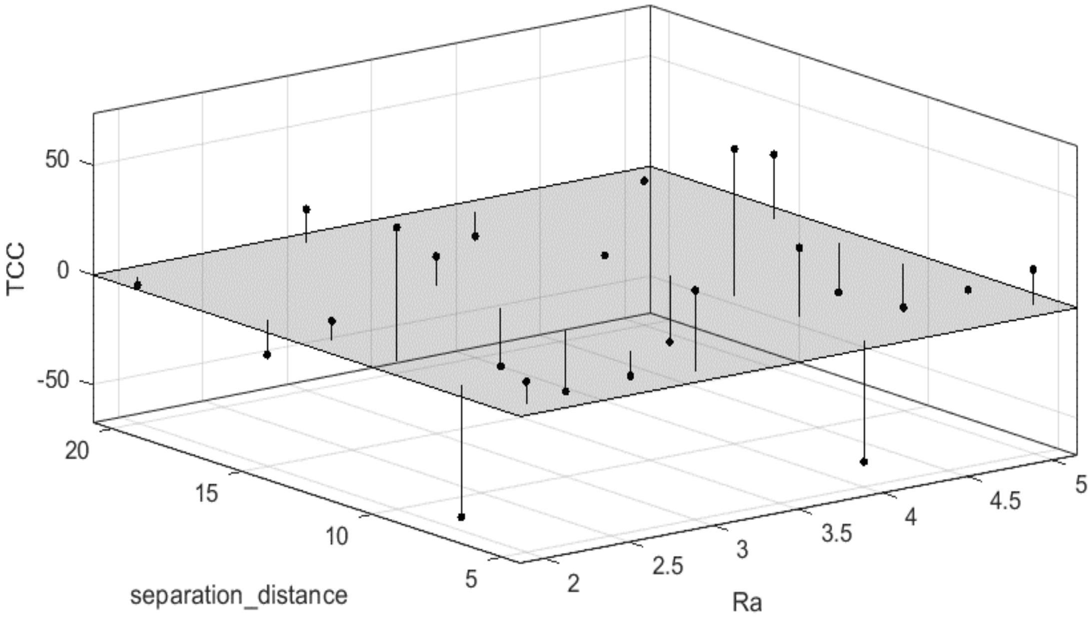

Fig. 5.25. Residual map for individual points of numerical analysis

Based on the results obtained, it was possible to propose a 4-th degree nonlinear polynomial approximating the TCC values in the range from 5 to 20[µm] for the separation distance (corresponding to contact pressure from 0.6[MPa] to 1[GPa]) and roughness values in the range from 2 to 5[µm] with reasonably high precision. The equation is defined as follows:

$$\begin{aligned} TCC(Ra,d) = {} & p_{00} + p_{10} * Ra + p_{01} * d + p_{20} * Ra^2 + p_{11} * Ra \\ & * d + p_{02} * d^2 + p_{30} * Ra^3 + p_{21} * Ra^2 * d + p_{12} \\ & * Ra * d^2 + p_{03} * d^3 + p_{31} * Ra^3 * d + p_{22} * Ra^2 * d^2 \\ & + p_{13} * Ra * d^3 + p_{04} * d^4 \end{aligned} \tag{5.6}$$

where, p_{ij} are the coefficients with 95[%] confidence bounds whose values were presented in Tab. 5.8:

Constant	Value	Confidence bounds
p_{00}	216.9	(157.3, 276.6)
p_{10}	160.7	(77.58, 243.9)
p_{01}	-355.6	(-427.6, -283.6)
p_{20}	15.07	(-26.13, 56.27)
p_{11}	-96.35	(-199.1, 6.448)
p_{02}	200.4	(44.4, 356.5)
p_{30}	7.73	(-40.9, 56.36)
p_{21}	67.2	(36.27, 98.13)
p_{12}	-49.14	(-78.93, -19.35)
p_{03}	-10.55	(-51.7, 30.6)
p_{31}	-19.04	(-68.71, 30.64)
p_{22}	-42.96	(-73.94, -11.99)
p_{13}	41.53	(6.72, 76.34)
p_{04}	-15.03	(-79.18, 49.11)

Tab. 5.8. Constants in the TCC surface-fit of Eq. 5.4

The above equation made it possible to approximate the results in the most accurate way. The parameters that allowed to state this were sum of the squares of the errors (SSE) and R-square parameter, whose values were respectively $2.318*10^4$ and 0.9915. SSE is a paramater that measures the total deviation of the response values obtained from the fit to the response valus observed. It is often called the summed of square of residuals. A value close to zero means that the model has a low random error variable and that the fit will be more suitable for predicition. The R-square states how succesfull the fit is in explaining the variation of the data. It is defined as the square of the correlation between the observed and the predicted response values. R-square can take on any value between 0 and 1 where R -value of 1 is a perfect fit.

In order to thoroughly test the precision of the correlation and assess its utility in practice, in the next months, MTU Aero Engines' thermal analysis and computational methods departments will try to verify it under different angles. The final conclusions will enable to determine further way of its development and thus help decide if the so established correlation should be introduced someday to daily usage.

5.7 Chapter Summary

In this chapter, the entire workflow for performing numerical simulations in order to determine interface thermal contact conductance has been presented. The principle of the script used to generate three-dimensional rough surfaces was discussed in conjunction with the meshing process and the element size influence on the results. Separate thermal analysis was carried out to check the influence of heat transfer modes on the TCC. The thermal contact phenomenon was considered in two different scales using classical CFD and Lattice-Boltzmann Method approach. Subsequently, findings were validated with experimental data, demonstrating strong agreement with each other. Finally, the TCC analytical correlation being the main task of the doctorate and its way of derivation was presented and discussed. In the next last chapter, attention is devoted to more specific details on entire analyses process and overall discussion about the dissertation aspects.

Chapter 6: Final Summary

The sixth, final chapter provides a review of the research performed so far and suggestions that may help to further improve analysis of the thermal contact resistance phenomenon.

6.1 Summary

Doctoral dissertation has been divided into chapters devoted to discussion of the entire core of the thermal contact resistance phenomenon. In the first of these, attention was focused on methods for describing solid rough surfaces. As it is generally known, no surface is perfectly flat. At the microscopic level, one can find multiple peaks and valleys that characterise the quality of the surface. There are three commonly distinguished ways of surface description in literature: deterministic, stochastic and fractal. Each of them has been described in detail, presenting the equations and assumptions governing each of them separately. Due to their different character of surface treatment, it is important to choose the appropriate surface description depending on each investigated issue peculiarity.

The next of the chapters described the principles of heat transfer accompanying the contact of two rough solid bodies. A number of factors determining and influencing the TCC were discussed. Characterisation of fluid regimes was depicted according to the temperature and related to this Knudsen criterion number defining the intermolecular distance. Correlations introduced over the years determining the value of the conductance coefficient on the metal-air-metal interface were presented. The foundations of single and multi-asperity models on which the above correlations are based were described, as well as ways of energy transfer on the interface between different mediums at atomic level. Additional chapters were devoted to considerations about vibrations and their impact on heat distribution, bolted joints and hysteresis effect which also contribute to non-linear changes in thermal contact resistance.

Subsequent chapter spoke about the innovative approach of conducting numerical calculations for fluids based on the kinetic equation of Boltzmann – Lattice Boltzmann Method. The foundations of the method, its strengths and weaknesses, propagation schemes depending on dimensions of the problem, types of their application, boundary conditions, ways of dealing with the curved edges of the objects under consideration and conjugate heat transfer were discussed in detail.

All numerical analyses were presented in Chapter 5. A Python script was created that allowed free creation of rough surfaces in a stochastic manner. Basic parameters describing surface such as: arithmetic mean height of rough profile, mean absolute slope, as well as geometrical factors such as object thickness and separation distance between two surfaces were also taken into account and implemented within the program code. The roughness height distribution was subjected to the Gaussian distribution, commonly used in the study of the dissertation’s main topic. The script interpolated sharp-pointed edges, and automatically recognised overlapping areas where it created contact spots. In addition, using Delanuay triangulation method, script created a mesh that was subsequently exported in separate .stl files. The files were then converted from the .stl format to the .step file, thus enabling their import into the HyperWorks environment. In the HyperMesh software, a further part of the reconstruction of the side walls took place, so as to successively carry out the process of filling out the solid and fluid domains with a non-structured tetrahedral mesh. With use of AcuSolve – a commercial numerical CFD solver, also as HyperMesh belonging to Altair - a number of analyses were carried out, examining the impact of individual modes of heat transfer on the TCC.

At the very beginning, the case of pure conduction was tested for five different stochastically generated contact pair geometries with air as interstitial medium and different surface operating temperatures. The goal was to analyse the spread of TCC values on the interface due to change of surface profile and temperature values applied on boundaries. The influence of temperature on the variability of material properties such as conductivity, specific heat and density was taken into account. The results showed a constant trend with standard deviation from the average TCC value obtained of approximately 14 percent. Afterwards, the effect of radiation as well as free and forced convection were investigated. Using a dedicated commercial LBM solver – XFlow – it was possible to carry out the mesoscopic analysis for forced convection in the case of low-pressure turbine housing and vane hook connection. The final results stated that the impact of radiation for the most extreme severe temperature load case was of range of 14[%] of the entire heat flux for ΔT equal 10[K] and 32[%] for temperature difference of 100[K]. In the case of free convection, the Grashof criterion number of (10^{-5}) made it possible to state that there is practically no place of such heat mode in microcontacts. Forced convection changed about 6% the total heat transfer coefficient in the flow through the micro-gap for a given input data which also turned out to have very low impact. Additional numerical studies were conducted to show the change in fluid temperature and its influence on the HTC. Comparably, also in this case the nature of the changes turned out to be insignificant, ultimately excluding convection as a factor with a major effect on the thermal resistance in microchannels.

An innovative technique has been presented for solving CFD problems. The purpose of implementing the LBM approach was in the interest of the author, who wanted to introduce other than traditional approach a method of numerical fluid computations. The CFD framework XFlow employs a kinetic particle-based solver that differs from the typical mesh-based analyses. The Lattice Boltzmann Method proved that it is able to solve advanced industrial problems even in the presence of complex geometries. The presented methodology has demonstrated that the method can be used with success for the thermal microflows. The XFlow did not face convergence issues, the code proved to be robust, efficient and accurate in terms of flow pattern predictions. Despite not discovering the new wheel, the method itself and its use gives great opportunities in even more complicated microflows over and inside complex geometries. The LBM should be treated as appropriate tool for analysing cases presented in this work. Its additional advantages are the lack of necessity of meshing, which was and still is a breakneck challenge in the case of classic CFD approach and domain discretisation for most of the companies.

The accuracy of the classical CFD procedure was checked with the experimental results for the two copper specimens under loading given by Tariq [123]. The performed numerical analyses showed great compliance with the literature data, thus confirming its reliability. The mechanical part of thermomechanical analysis was completely omitted in the dissertation. By using the simplified model presented by Singhal [124], the separation distance between surfaces was modified explicitly depending on the contact pressure only.

Eventually, a new correlation was developed allowing thermal contact conductance derivation. The correlation is based on the mean arithmetic roughness and separation distance that is, widely-used parameters describing the finishing quality of the surface. For the varying roughness and separation distance, 24 separate simulations were conducted to obtain the TCC value. With the use of MATLAB software, it was possible to approximate the obtained results with a surface defined by 4-th degree nonlinear polynomial, being the final correlation. Formula will be tested and confronted with the tools and models used at MTU Aero Engines in the nearest future.

6.2 Recommendations for Future Development

As it is commonly known, everything in the world can be further refined, not excluding some aspects of this study. Due to the work character, which was purely numerical, one of the key elements of technical doctoral dissertations was omitted i.e. experimental research. In order to fully determine the reliability of the results obtained by means of the simulation's results, it would be necessary to perform bench tests for material samples and boundary conditions corresponding to real contact pairs in the aircraft turbine engine. Unfortunately, due to the pandemic, the budget for the experiment was withdrawn, thus preventing its implementation as part of the Implementation PhD ministerial program. Hope does not die, and the author deeply believes in the possibility of carrying it out in the future.

Optimisation should be first dedicated to improving efficiency and performance of the rough surface reconstruction process. Generation of contact pairs and meshing their domains took the most time of analysis setup preparations. Certainly, it would be possible to make an algorithm implementing automatically obtained files from the Python script into the HyperWorks environment. The software allows i.e. of the incorporation of TCL scripts that could handle this issue.

Another recommendation is a deeper investigation of the mechanical model, which in this study has been significantly simplified. The pressure acting on contact pairs obviously causes deformations and nonlinear changes in the actual contact area of asperities. An accurate model describing the nature of the surface modification should be developed and linked with the thermal part to make the model more physically consistent. Such solution will allow to better estimate the strength and life cycle of working parts.

From the point of view of an aircraft engine work specification, it would be necessary to take into account the amplitude and frequency of vibrations. This factor plays a significant role and its influence should not be ignored in the view of oscillations of contact pressure, thereby potential changes in the TCC values.

Dissertation presents the phenomenon of thermal contact resistance under macro- and mesoscopic scales. In the world of progressive miniaturisation and condensation into microscopic dimensions, expanded studies should be conducted to include micro and submicro scales effect. With help of that it would be possible to incorporate higher-order effects of smaller roughness scales, which were unfortunately not captured using LBM analyses. It is highly probable that new correlations would be derived thus enabling more accurate TCC predictions. For this purpose, fractal description of the surface or high-quality topographic scanners including Molecular Dynamics (MD) analysis may be used.

Chapter 7: Bibliography

[1] Mohamad A. A., "Lattice Boltzmann Method: Fundamentals and Engineering Applications with Computer Codes", Springer Science & Business Media, 2011.

[2] Montessori A., Falcucci G., "Lattice Boltzmann Modeling of Complex Flows for Engineering Applications", Morgan & Claypool Publishers, 2018.

[3] Nayak P. R., “Random Process Model of Rough Surfaces”, Journal of Lubrication Technology, 1971.

[4] Voss R. F., “Fractals in Nature: From Characterization to Simulations", The Science of Fractal Images, New York, Springer-Verlag 21-70, 1988.

[5] Voss R. F., “Random Fractals: Characterization and Measurement”, Scaling Phenomena in Disordered Systems, New York, Plenum Press 1-11, 1985.

[6] Majumdar A. and Bhushan B., "Role of fractal geometry in roughness characterization and contact mechanics of surfaces", ASME J. Tribol. 112, 1990.

[7] Bhushan B., "Surface roughness analysis and measurement techniques", vol. 1. Boca Raton: CRC Press; 2001.

[8] Bhushan B., "Contact mechanics of rough surfaces in tribology: Multiple asperity contact", Tribol Lett, 1998.

[9] Jacobs T. D., Junge T., and Pastewka L., “Quantitative characterization of surface topography using spectral analysis”, Surface Topography: Metrology and Properties, 2017.

[10] Bhushan B., “Introduction to Tribology”, 2nd edition, John Willey & Sons Inc., New York, 2013.

[11] Madhusudana C.V., "Thermal Contact Conductance", Mechanical Engineering Series, Springer-Verlag New York Inc., 1996.

[12] Jackson L. J., Bhavnavi S. H., Ferguson T. P., "A multiscale model of thermal contact resistance between rough rufaces", Journal of Heat Transfer, Vol. 130, 2008.

[13] Bahrami M., Culham J. R., Yananovich M. M., and Schneider G. E., “Review of Thermal Joint Resistance Models for Nonconforming Rough Surfaces”, Applied Mechanics Reviews, 2006.

[14] Cooper M.G., Mikic, B.B. and Yovanovich, M., "Thermal Contact Conductance: International Journal of Heat and Mass Transfer, 12. 279-300, 1969.

[15] Bahrami M., Culham J. R., Yananovich M. M., and Schneider G. E., “Thermal Contact Resistance of Nonconforming Rough Surfaces", Contact Mechanics Model, Journal of Thermophysics and Heat Transfer, Vol. 18, 2004.

[16] Bhushan B., “Handbook of Micro/Nanotribology: Second Edition”, Mechanics & Materials Science, CRC Press LLC, 2019.

[17] Davies S., Hall P., "Fractal analysis of surface roughness by using spatial data", J. R. Statist. Soc. B 61, 1999.

[18] Borodich F.M., Evans H.P., "Fractal Characterization of Surfaces". In: Wang Q.J., Chung YW. (eds) Encyclopedia of Tribology. Springer, Boston, MA, 2013.

[19] Ganti S. and Bhushan B., "Generalized fractal analysis and its applications to engineering surfaces", Wear, 1995.

[20] Liu G., Zhu J., Yu L. and Wang Q. J., “Elasto-Plastic Contact of Rough Surfaces”, Tribology Transactions, 2001.

[21] Barber J.R., “Thermoelastic instabilities in the sliding of conforming solids”, Proc. R. Soc. Lond. A, 1969.

[22] Cengel Y. and Ghajar A., “Heat and Mass Transfer: Fundamentals and Applications”, 6th Edition, 2020.

[23] Grujicic M., Zhao C.L. and Dusel E.C., “The effect of thermal contact resistance on heat management in the electronic packaging”, Applied Surface Science, 2005.

[24] Fieberg C. and Kneer R., “Determination of thermal contact resistance from transient temperature measurements”, International Journal of Heat and Mass Transfer, 2008.

[25] Donghuan L. & Zhang J., “Numerical simulation of high-temperature thermal contact resistance and its reduction mechanism”, PLOS ONE, 2018.

[26] Hamasaiid A., Dargusch M., Davidson C., Loulou T., and Dour G., “A Model to Predict the Heat Transfer Coefficient at the Casting-Die Interface for the High Pressure Die Casting Process”, 2007.

[27] Donghuan L., Luo Y. and Shang X., "Experimental investigation of high temperature thermal contact resistance between high thermal conductivity C/C material and Inconel 600", International Journal of Heat and Mass Transfer, 2015.

[28] Ruifeng D., Tianran G., Xunliang L., and Zhi W., Effects of contact pressure, interface temperature, and surface roughness on thermal contact conductance between stainless steel surfaces under atmosphere condition", International Journal of Heat and Mass Transfer, 2016.

[29] Tang Q., He J. and Zhang W., "Influencing factors of thermal contact conductance between TC4/30CrMnSi interfaces", International Journal of Heat and Mass Transfer. 86. 694-698, 2015.

[30] Greenwood J., "Constriction Resistance and the Real Area of Contact. British Journal of Applied Physics", 17. 1621-1632, 1966.

[31] Zhang X., Cong P. and Fujii M., "A Study on Thermal Contact Resistance at the Interface of Two Solids". International Journal of Thermophysics. 27. 880-895, 2006.

[32] Bejan A., Kraus A. D., "Heat transfer handbook”, New York: John Wiley & Sons, 2003.

[33] Greenwood J., “Contact of Nominally Flat Surfaces,” Proc. R. Soc. Lond. A295:300–319, 1966.

[34] Cooper M. G., M. M. Yovanovich, and B. B. Mikic, “Thermal Contact Conductance,” Int J. Heat Mass Transf., vol. 153, pp. 317–23, 1969.

[35] Mikic B. B., “Thermal contact conductance; theoretical considerations,” Int. J. Heat Mass Transf., vol. 17, pp. 205–214, 1974.

[36] Kumar S. S. and Ramamurthi K., “Thermal contact conductance of pressed contacts at low temperatures,” Cryogenics (Guildf)., vol. 44, no. 10, pp. 727–734, 2004.

[37] Bush A. W., Gibson R. D., Thomas T. R., Polytechnic T., and Road B., “The elastic contact of a rough surface,” vol. 35, pp. 87–111, 1975.

[38] Sridhar M. R. and Yovanovich M. M., “Elastoplastic contact conductance model for isotropic conforming rough surfaces and comparison with experiments,” J. Heat Transf., vol. 118, no. 1, pp. 3–9, 1996.

[39] Zhang X., Cong P. Z., and Fujii M., “A study on thermal contact resistance at the interface of two solids,” Int. J. Thermophys., vol. 27, no. 3, pp. 880–895, 2006.

[40] Zhang X., Cong P., Fujiwara S., and Fujii M., “A new method for numerical simulation of thermal contact resistance in cylindrical coordinates,” Int. J. Heat Mass Transf., vol. 47, no. 5, pp. 1091–1098, 2004.

[41] Tomimura T., Matsuda Y., Zhang X., and Fujii M., “Computer simulation of thermal contact conductance based on random numbers,” JSME Int. J. Ser. B Fluids Therm. Eng., vol. 43, no. 4, pp. 665–670, 2000.

[42] Kapitza P. L., “The Study of Heat Transfer in Helium II”, J. Phys. USSR, 4:181, 1941.

[43] Khalatnikov I. M., "Zh. Eksp. i Teor Fiz”, 1952.

[44] Khvesyuk V., Liu B., Barinov, A., “Development of acoustic and diffuse mismatch models for predicting the Kapitza resistance”, Journal of Physics: Conference Series, 2019.

[45] Swartz E. T., Pohl R. O., “Thermal boundary resistance”, Rev. Mod. Phys. 61, 1989.

[46] Furmański P., Wiśniewski T. S., Banaszek J., "Thermal contact resistance and other thermal phenomena at solid-solid interface", Istitute of Hear Engineering - Warsaw university of technology, 2008.

[47] Dongari N., Sharma A. and Durst F., "Pressure-driven diffusive gas flows in micro-channels: From the Knudsen to the continuum regimes", Microfluidics and Nanofluidics. 6. 679-692, 2009.

[48] Song S. and Yovanovich M. M., "Correlation of Thermal Accommodation Coefficient for 'Engineering' Surfaces", Fundamentals of Conduction and Recent Developments in Contact Resistance, ASME HTD-Vol. 69, p117, 1987.

[49] Rettner C., "Determination of Accommodation Coefficients for N2 at Disk-Drive Air-Bearing Surfaces", Journal of Tribology-transactions of The Asme 119, 1997.

[50] Fan G., Manson J.R., "Calculations of the Energy Accommodation Coefficient for Gas-Surface Interactions", Chemical Physics 370, 2008.

[51] Sonnick S., Meier M., Ünsal-Peter G., Erlbeck L., Nirschl H., and Rädle M., "Thermal Accommodation in Nanoporous Silica for Vacuum Insulation Panels", International Journal of Thermofluids, 2020.

[52] Zhu Z., Zhang L.-W., Gu S.-D., "Experimental investigation of transient heat transfer between Hastelloy C-276/narrow air gap/silicon steel", School of Materials Science and Engineering, Dalian University of Technology, Dalian 116085, China, 2012.

[53] Fieberg C., Kneer R., "Determination of thermal contact resistance from transient temperature measurements", International Journal of Heat and Mass Transfer 51 1017–1023, 2008.

[54] Lozinskii M. G., "High Temperature Metallography", Elsevier, 2013.

[55] Usamentiaga R., Venegas P., Guerediaga J., Vega L., Molleda J. and Bulnes F. G., "Infrared Thermography for Temperature Measurement and Non-Destructive Testing", ISSN 1424-8220, 2014.

[56] Crisóstomo J., Pitarma R., "The Importance of Emissivity on Monitoring and Conservation of Wooden Structures Using Infrared Thermography", Advances in Structural Health Monitoring, Maguid H.M. Hassan, IntechOpen, 2019.

[57] Shojaeefard M. H., "Inverse heat transfer problem of thermal contact conductance estimation in periodically contacting surfaces, Journal of Thermal Science volume 18, 2009.

[58] "Weiganda B., Lipnicki Z., ""Development of the contact layer and its role in the phase change process"", International Journal of Heat and Mass Transfer
Volume 93, 2016."

[59] Bourouga B. et. al., "Experimental study of thermal sliding contact parameters at interface seat of large strains", International Journal of Material Forming, 2010.

[60] Beck J. V., "Determination of optimum, transient experiments for thermal contact conductance", International Journal of Heat and Mass Transfer Volume 12, 1969.

[61] Altun Ö. & Böke E., "Heat Transfer Analyses of Thermal Barrier Coatings on a Metal Substrate", ISI BILIMI VE TEKNIGI DERGISI-JOURNAL OF THERMAL SCIENCE AND TECHNOLOGY 33. 101-109, 2013.

[62] Katsuyama H. & TakahashiS. & Akoshima M., "Evaluation of thermal conductivity and interfacial thermal resistance of thermal barrier coating", The Proceedings of Conference of Kanto Branch, 2018.

[63] Morega A., "Thermal Contact Resistance Between Two Flat Surfaces That Squeeze a Film of Lubricant", Journal of Heat Transfer-transactions of The Asme - J HEAT TRANSFER. 115. 763-767. 10.1115/1.2910749, 1993.

[64] Devices for Damping Mechanical Vibrations: Mildred Benton Naval Research Laboratory, United States government printing office, Washington, 1957

[65] Vance M., Ying D., and Nikolajsen, J. L., "Actively Controlled Bearing Dampers for Aircraft Engine Applications", Proceedings of the ASME 1999 International Gas Turbine and Aeroengine Congress and Exhibition. Volume 4: Manufacturing Materials and Metallurgy; Ceramics; Structures and Dynamics; Controls, Diagnostics and Instrumentation; Education; IGTI Scholar Award; General. Indianapolis, Indiana, USA. V004T03A004. ASME. https://doi.org/10.1115/99-GT-018, 1999.

[66] Duffy K. P., „Overview of NASA GRC Research on Damping of Jet Engine Blades”, Pennsylvania State University, 2012.

[67] Rötscher, F., "Die Maschinenelelemente", Berlin, 1927.

[68] Madhusudana C.V., "Thermal Contact Conductane", second edition, Springer, 2013.

[69] Yeh C. L. et al., "An experimental investigation of thermal contact conductance across bolted joints", Department of Mechanical Engineering, 2001.

[70] Howells R. I. L., Probert S. D., Jenkins J. H., J. Strain Anal. 4 11 5-20, 1969.

[71] Bradley T. L., Lardner T. J., Mikic, B. B., "Bolted Joint Interface Pressure for Thermal Contact Resistance." ASME. J. Appl. Mech., 1971.

[72] Li Y.Z., Madhusudana C.V., Leonardi E., “On the enhancement of the thermal contact conductance: Effect of loading history,” Journal of Heat Transfer, 122, pp. 46-49, 2000.

[73] McNamara R., Zanetti G., "Use of the Boltzmann Equation to Simulate Lattice-Gas Automata", Phys. Rev. Lett. 61, 2332, 1988.

[74] Xiaoyi H., Li-Shi L., "Theory of the lattice Boltzmann method: From the Boltzmann equation to the lattice Boltzmann equation", PHYSICAL REVIEW E. 56. 6811-6817. 10.1103, 1997.

[75] Zhao Y., Wu Y., Chai Z., Shi B., "A central-moment multiple-relaxation-time collision model", Computers & Mathematics with Applications, 2019.

[76] A. A. Mohamad, "Lattice Boltzmann Method: Fundamentals and Engineering Applications with Computer Codes", Springer Science & Business Media, 2011.

[77] Chapman, S., Cowling T.G., "The Mathematical Theory of Non-uniform Gases", Cambridge Mathematical Library, 3rd Edition, 1991.

[78] Filippova O., D. Hänel, "Lattice-Boltzmann simulation of gas-particle flow in filters", Computers andfluids 26, 1997.

[79] Hudong C., Shiyi C., Matthaeus W., "Recovery of the Navier-Stokes Equations Using a Lattice-Gas Boltzmann Method", Physical Review A. 45. 10.1103, 1992.

[80] Guo, Z., Zheng C., Shi B., "Discrete lattice effects on the forcing term in the lattice Boltzmann method", Physical Review E 65(4): p. 046308, 2002.

[81] Atif M., Namburi M., Ansumali S., "Higher-order lattice Boltzmann model for thermohydrodynamics". Physical Review E. 98. 53311. 10.1103, 2018.

[82] Suiker, A. S. and Chang, C. S., "Application of higher-order tensor theory for formulating enhanced continuum models", Acta Mechanica, 142(1-4):223–234, 2000.

[83] Cercignani, C. "Mathematical Methods in Kinetic Theory, Springer", Boston, MA, 1990.

[84] Bhatnagar P. L., Gross E. P., Krook M., "A Model for Collision Processes in Gases. I. Small Amplitude Processes in Charged and Neutral One-Component Systems" Phys. Rev. 94, 511, 1954.

[85] Buckingham, E. "On physically similar systems; illustrations of the use of dimensional equations", Phys. Rev. 4{4), 1914.

[86] Deville M.O., Gatski T.B., "The Boltzmann Equation. In: Mathematical Modeling for Complex Fluids and Flows", Springer, Berlin, Heidelberg, 2012.

[87] Chen, S. and Doolen, G. D., "Lattice Boltzmann method for fluid flows", Annual Review of Fluid Mechanics, 30(1):329–364, 1998.

[88] Nathen Patrick & Gaudlitz, Daniel & Krause, Mathias & Adams, Nikolaus, "On the Stability and Accuracy of the BGK, MRT and RLB Boltzmann Schemes for the Simulation of Turbulent Flows", Communications in Computational Physics. 23. 846-876. 10.4208/cicp.OA-2016-0229, 2018.

[89] Coveney P. V., Succi S., D'Humières D., Ginzburg I., Krafczyk M., Lallemand P., Luo L.-S., "Multiple–relaxation–time lattice Boltzmann models in three dimensions", Phil. Trans. R. Soc. A.360437–451, 2002.

[90] Bennett S., "A Lattice Boltzmann model for diffusion of binary gas mixtures", PhD thesis, King’s College, Cambridge, 2013.

[91] Lallemand P. and Luo L.-S., "Theory of the lattice Boltzmann method: Dispersion, dissipation, isotropy, Galilean invariance, and stability", Phys. Rev. E, 61:6546–6562, 2000.

[92] D’Humières, D., "Multiple–relaxation–time lattice Boltzmann models in three dimensions", Philosophical Transactions of the Royal Society of London A: Mathematical, Physical and Engineering Sciences, 360 1792):437–451, 2002.

[93] Skordos P. A., "Initial and boundary conditions for the lattice Boltzmann method", Phys. Rev. E 48, 4823, 1993.

[94] Yu D., Mei R., and Shyy W., "A Unified Boundary Treatment in Lattice Boltzmann Method", 2003.

[95] Mei R., Luo L., Lallemand P., and D’Humières D., "Consistent Initial Conditions for LBE Simulations", Computers & Fluids, 35 pp. 855–862, 2006.

[96] Hirsch C., „Numerical Computation of Internal & External Flows", Butterworth-Heinemann, Great Britan, 2007.

[97] Bouzidi M., Firdaouss M., and Lallemand P., "Momentum transfer of a Boltzmann-Lattice fluid with boundaries", Physics of Fluids, 13, pp. 3452–3459, 2013.

[98] Ting Zhang & Shi, Baochang & Guo, Zhaoli & Lu, Jianhua., "General bounce-back scheme for concentration boundary condition in the lattice-Boltzmann method", Physical review. E, Statistical, nonlinear, and soft matter physics. 85. 016701. 10.1103, 2012.

[99] Ladd A. J., "Numerical simulations of particulate suspensions via a discretized Boltzmann equation. part 1. theoretical foundation", Journal of Fluid Mechanics, 271:285–309, 1994.

[100] Yu D., Mei R., Luo L.-S. and Shyy W., "Viscous flow computations with the method of lattice Boltzmann equation", Prog. Aerosp. Sci. 39, 329–367, 2003.

[101] Mei R., Luo L.-S., and Shyy W., "An accurate curved boundary treatment in the lattice Boltzmann method", Journal of Computational Physics, 155(2):307 –330, 1999.

[102] Zou Q. and He X., "On pressure and velocity boundary conditions for the lattice boltzmann bgk model", Physics of Fluids, 9(6):1591–1598, 1997.

[103] Lallemand P. and Luo L.-S., "Lattice Boltzmann method for moving boundaries", J. Comp. Phys. 184, 406–421, 2003.

[104] Rohde M., KandhaiD., Derksen J. J. and Van den Akker H. E. A., "Improved bounceback methods for no-slip walls in lattice-Boltzmann schemes: Theory and simulations", Phys. Rev. E 67, 066703, 2003.

[105] Chun B. and Ladd A. J. C., "Interpolated boundary condition for lattice Boltzmann simulations of flows in narrow gaps", Phys. Rev. E 75, 066705, 2007.

[106] Peskin C. S., "Numerical analysis of blood flow in the heart", J. Comput. Phys., 25, pp.220–252., 1977.

[107] Feng Z. G. and Michaelides E. E., "The immersed boundary-lattice Boltzmann method for solving fluid-particles interaction problems", J. Comput. Phys., 195, pp. 602–628, 2004.

[108] Shu C., Liu N. Y. and Chew Y. T., "A novel immersed boundary velocity correction-lattice Boltzmann method and its application to simulate flow past a circular cylinder", J. Comput. Phys., 226, pp. 1607–1622, 2007.

[109] Wu J. and Shu C., “Implicit velocity correction-based immersed boundary-lattice Boltzmann method and its applications”, J. Comput. Phys., 228 (2009), pp. 1963–1979.

[110] Wang X., Shu C., Wu J. and Yang L. M., „A Boundary Condition-Implemented Immersed Boundary-Lattice Boltzmann Method and Its Application for Simulation of Flows Around a Circular Cylinder", Advances in Applied Mathematics and Mechanics, pp. 811-829 813, 2014.

[111] https://www.python.org/

[112] Arora J. S., "Introduction to Optimum Design (Third Edition)", Elsevier, 2012.

[113] https://altairhyperworks.com

[114] https://altairhyperworks.com/product/AcuSolve

[115] https://www.3ds.com/products-services/simulia/products/xflow/

[116] https://palabos.unige.ch

[117] http://sailfish.us.edu.pl

[118] https://www.openlb.net

[119] https://www.engineeringtoolbox.com/air-specific-heat-capacity-d_705.html

[120] https://www.researchgate.net/figure/Properties-of-MAR-M247-Ni-based-superalloy-vs-temperature-a-Thermal-conductivity-b_fig7_268509009

[121] Jennings S. G., "The mean free path in air", J. Aerosol Sci., Vol. 19, No. 2, pp. 159-166, 1988.

[122] Blazek J., "Computational Fluid Dynamics: Principles and Applications", Elsevier, 2011.

[123] Tariq A., Asif M., “Experimental investigation of thermal contact conductance for nominally flat metallic contact,” Heat Mass Transf. und Stoffuebertragung, vol. 52, no. 2, pp. 291–307, 2016.

[124] Singhal V., et. al. "An Experimentally Validated Thermo-Mechanical Model for the Prediction of Thermal Contact Conductance", CTRC Research Publications, 2005.

[125] http://www-ferp.ucsd.edu/LIB/PROPS/PANOS/cu.html

[126] https://www.mathworks.com/products/matlab.html

[127] Montgomery D. C., Peck E. A., Vining G. G., "Introduction to Linear Regression Analysis 5th Edition", 2012.

[128] Frekers Y., Helmig T., Burghold E. M., and Kneer R., “A numerical approach for investigating thermal contact conductance,” Int. J. Therm. Sci., vol. 121, pp. 45–54, 2017.

[129] Yüncü H., “Thermal contact conductance of nominally flat surfaces,” Heat Mass Transf., vol. 43, no. 1, pp. 1–5, 2006.

[130] Madhusudana C. V., “Heat Flow Through Conical Constrictions,” AIAA J., vol. 18, no. 10, pp. 1261–1262, 1980.

[131] Zou M., Yu B., Cai J., and Xu P., “Fractal Model for Thermal Contact Conductance,” J. Heat Transfer, vol. 130, no. 10, p. 101301, 2008.

[132] Zhang P., Cui T., and Li Q., “Effect of surface roughness on thermal contact resistance of aluminium alloy,” Appl. Therm. Eng., vol. 121, pp. 992–998, 2017.

[133] Shi L. and Wang H., “Investigation on thermal contact resistance by photothermal technique at low temperature,” Heat Mass Transf., vol. 43, no. 11, pp. 1179–1184, 2007.

[134] Zheng X., Liu D., Wei D., and Shang X., “Experimental investigation of high temperature thermal contact resistance with interface material,” Theor. Appl. Mech. Lett., vol. 1, no. 5, p. 051009, 2011

[135] Xing L., Zhang W., Zhang X. Z., and Yue C. X., “Experimental Investigation of Contact Heat Transfer at High Temperature Based on Steady-State Heat Flux Method,” Exp. Heat Transf., vol. 23, no. 2, pp. 107–116, 2010.

[136] Gopal V., Whiting M. J., Chew J. W., and Mills S., “Thermal contact conductance and its dependence on load cycling,” Int. J. Heat Mass Transf., vol. 66, pp. 444–450, 2013.

[137] Wahid S. M. S., Madhusudana C. V, and Leonardi E., “Solid spot conductance at low contact pressure,” Exp. Therm. Fluid Sci., 2004

[138] Ansumali S. and Karlin I.V.. “Kinetic boundary conditions in the lattice Boltzmann method”, Physical Review E - Statistical, Nonlinear, and Soft Matter Physics, 66 (2):1–6, 2002.

[139] Zou Q. and He X.., “On pressure and velocity boundary conditions for the lattice Boltzmann BGK model”, Physics of Fluids, 9(6):1591, 1997.

[140] Succi S., “The Lattice Boltzmann Equation: For Fluid Dynamics and Beyon Numerical Mathematics and Scientific Computation”, Clarendon Press, 2001.

[141] Murashov M. V. and Panin S. D., “Modeling of thermal contact conductance,” 2010 14th Int. Heat Transf. Conf. IHTC 14, vol. 6, no. January 2010, pp. 387–392, 2010.

[142] Nie X., “A lattice-boltzmann / finite-difference hybrid simulation of transonic flow”, 2009.

[143] Higuera, F. J., Succi, S., and Benzi, R. “Lattice gas dynamics with enhanced collisions”, EPL (Europhysics Letters), 1989.

[144] Heubes, D., Bartel, A., and Ehrhardt, M., “Characteristic boundary conditions in the lattice boltzmann method for fluid and gas dynamics”, Journal of Computational and Applied Mathematics, 262:51 – 61, 2014.

[145] Izquierdo S., Martinez-Lera, P., and Fueyo, N., “Analysis of open boundary effects in unsteady lattice boltzmann simulations”. Computers and Mathematics with Applications, 58(5):914–921, 2009.

[146] Suga K., “Lattice Boltzmann methods for complex micro-flows: applicability and limitations for practical applications”. Fluid Dynamics Research, 45(3):034501, 2013.

[147] Yang Z., “Lattice Boltzmann outflow treatments: Convective conditions and others”, Computers and Mathematics with Applications, 65(2):160–171, 2013.

[148] Zou Q. and He X., “On pressure and velocity boundary conditions for the lattice Boltzmann BGK model”. Physics of Fluids, 9(6):1591, 1997.

[149] Spinelli G. and B. Celik, "Leveling Out Interface Temperature for Conjugate Heat Transfer Problems", Computers & Fluids, 2020.

[150] Tong Z.-X. et. al., "Two-dimensional numerical model for predicting fouling shape growth based on immersed boundary method and lattice Boltzmann method", Applied Thermal Engineering, 2020.

[151] Sahraoui N. et.al., "Numerical investigation of low Prandtl number effect on mixed convection in a horizontal channel by the lattice Boltzmann method", Heat Transfer, 2020.

[152] Ye H. et. al., "OpenFSI: A highly efficient and portable fluid–structure simulation package based on immersed-boundary method", Computer Physics Communications, 2020.

[153] Qu W. et. al., "Microstructural Evolution Mechanism of Semi-solid Slurry: A Study Using Phase-Field-Lattice-Boltzmann Scheme", Journal of Materials Processing Technology, 2020.

[154] Yang B. et. al., "A Multiple-Relaxation-Time Lattice Boltzmann Model for Natural Convection in a Hydrodynamically and Thermally Anisotropic Porous Medium under Local Thermal Non-Equilibrium Conditions", Journal of Thermal Science, 2020.

Appendix

I. Three-dimensional surface reconstruction script

```
####################################################################
# SURFACE RECONSTRUCTION SCRIPT
####################################################################

import math
import random
import matplotlib.pyplot as plt
import numpy as np
from scipy.interpolate import Rbf
from stl import mesh
import matplotlib.tri as mtri

####################################################################
# Standard Gaussian Distribution Cumulative Distribution Function (CDF)
####################################################################

znorm_max = 6.0  # height distribution range from -6σ to +6σ
znorm_min = -6.0
N_intervals = 10000  #  number of discretization bands
del_z = (znorm_max - znorm_min) / (N_intervals - 1)  # del_z – band width
znorm = [znorm_min]
smoothing_factor = 5

for i in range(1, N_intervals):
    znorm.append(znorm_min + i * del_z)

####################################################################
#  Error function
####################################################################

def erf(x):
    a1 = 0.254829592
    a2 = -0.284496736
    a3 = 1.421413741
    a4 = -1.453152027
    a5 = 1.061405429
```

```
    p = 0.3275911
    sign = 1
    if x < 0:
        sign = -1
    x = abs(x)
    t = 1.0 / (1.0 + p * x)
    erfx = 1.0 - (a1 * t + a2 * (t ** 2) + a3 * (t ** 3) + a4 * (t ** 4) + a5 * (t ** 5)) *
math.exp(-x * x)
    return sign * erfx

#####################################################################
# Compute Cumulative Distribution Function (CDF)
#####################################################################

cdf = [0.0]
for i in range(1, N_intervals):
    term = znorm[i - 1] / (math.sqrt(2))
    cdf.append(0.5 * (1.0 + erf(term)))

#####################################################################
# Interface descriptors
#####################################################################

Ra1 = 5  # arithmetic mean roughness of bottom surface
s1 = 1.25 * Ra1  # root mean roughness (RMS) of bottom surface
Ra2 = 5 # arithmetic mean roughness of top surface
s2 = 1.25 * Ra2  # root mean roughness (RMS) of top surface
N = 101 # number of sampled heights
dx = 4 # sampling interval
h = 5 # separation distance

#####################################################################
# Bottom surface
#####################################################################

# scale standard height distribution using RMS height of bottom surface
z1 = []
for i in range(1, N_intervals + 1):
    z1.append(znorm[i - 1] * s1)

x4_bottom_a = np.arange(0,N*dx,dx)
```

```
z4_bottom_a = np.arange(0,N*dx,dx)
y4_bottom_a = []
for i in range(x4_bottom_a.size):
   y4_bottom_a.append([])
   for j in range(x4_bottom_a.size):
      y4_bottom_a[i].append(0)

for i in range(x4_bottom_a.size):
   for j in range(z4_bottom_a.size):
      R = random.random()
      for k in range(1, N_intervals):
         index1 = k - 1
         index2 = index1 + 1
         ht1 = cdf[index1]  # ht1- minimum height limit of band j
         ht2 = cdf[index2]  # ht2- maximum height limit of band j
         if (R >= ht1 and R < ht2):
            pk = z1[index1]
            y4_bottom_a[i][j] = pk

x4_bottom, z4_bottom = np.meshgrid(x4_bottom_a,z4_bottom_a)
y4_bottom = np.array(y4_bottom_a)

###################################################################
# Top surface
###################################################################

z2 = []
for i in range(1, N_intervals + 1):
   z2.append(znorm[i - 1] * s2)

x4_top_a = np.arange(0,N*dx,dx)
z4_top_a = np.arange(0,N*dx,dx)
y4_top_a = []
for i in range(x4_top_a.size):
   y4_top_a.append([])
   for j in range(x4_top_a.size):
      y4_top_a[i].append(0)

for i in range(x4_top_a.size):
   for j in range(z4_top_a.size):
      R = random.random()
```

```
        for k in range(1, N_intervals):
            index1 = k - 1
            index2 = index1 + 1
            ht1 = cdf[index1]  # ht1- minimum height limit of band j
            ht2 = cdf[index2]  # ht2- maximum height limit of band j
            if (R >= ht1 and R < ht2):
                pk = z2[index1]
                y4_top_a[i][j] = pk + h

x4_top, z4_top = np.meshgrid(x4_top_a,z4_top_a)
y4_top = np.array(y4_top_a)

##################################################################
# Surface smoothing using smoothing factor
##################################################################

rbf = Rbf(x4_bottom, z4_bottom, y4_bottom, epsilon=2)
x_bottom_sm_1                                                     =
np.arange(0,(N*smoothing_factor)*(dx/smoothing_factor),(dx/smoothing_factor
))
z_bottom_sm_1                                                     =
np.arange(0,(N*smoothing_factor)*(dx/smoothing_factor),(dx/smoothing_factor
))
x_bottom_sm,z_bottom_sm = np.meshgrid(x_bottom_sm_1,z_bottom_sm_1)
Y_bottom_smooth = rbf(x_bottom_sm,z_bottom_sm)
rbf = Rbf(x4_top, z4_top, y4_top, epsilon=2)
x_top_sm_1                                                        =
np.arange(0,(N*smoothing_factor)*(dx/smoothing_factor),(dx/smoothing_factor
))
z_top_sm_1                                                        =
np.arange(0,(N*smoothing_factor)*(dx/smoothing_factor),(dx/smoothing_factor
))
x_top_sm,z_top_sm = np.meshgrid(x_top_sm_1,z_top_sm_1)
Y_top_smooth = rbf(x_top_sm, z_top_sm)

##################################################################
# Remove intersections
##################################################################

for i in range(N*smoothing_factor):
    for j in range(N*smoothing_factor):
```

```
        if Y_bottom_smooth[i][j] > Y_top_smooth[i][j]:
            Y_bottom_smooth[i][j] = Y_top_smooth[i][j]
        if Y_top_smooth[i][j] < Y_bottom_smooth[i][j]:
            Y_top_smooth[i][j] = Y_bottom_smooth[i][j]

###############################################################
# Limits
###############################################################
margin = 1

# Finding max and min Y values
max_height = np.amax(Y_top_smooth)
min_height = np.amin(Y_bottom_smooth)

# Finding top and bottom surfaces
top_surface = max_height + margin
bottom_surface = min_height - margin
surf_top = np.empty_like(Y_top_smooth)
surf_bottom = np.empty_like(Y_bottom_smooth)
for i in range(N*smoothing_factor):
    for j in range(N*smoothing_factor):
        surf_top[i][j] = top_surface
        surf_bottom[i][j] = bottom_surface

###############################################################
# STL export
###############################################################

x_bottom_sma = x_bottom_sm.flatten()
z_bottom_sma = z_bottom_sm.flatten()
Y_bottom_smootha = Y_bottom_smooth.flatten()

tri = mtri.Triangulation(x_bottom_sma,z_bottom_sma)

data = np.zeros(len(tri.triangles), dtype=mesh.Mesh.dtype)
bottom_mesh = mesh.Mesh(data, remove_empty_areas=False)
bottom_mesh.x[:] = x_bottom_sma[tri.triangles]
bottom_mesh.y[:] = z_bottom_sma[tri.triangles]
bottom_mesh.z[:] = Y_bottom_smootha[tri.triangles]
bottom_mesh.save('bottom_surface.stl')
```

```
x_top_sma = x_top_sm.flatten()
z_top_sma = z_top_sm.flatten()
Y_top_smootha = Y_top_smooth.flatten()

tri = mtri.Triangulation(x_top_sma,z_top_sma)

data = np.zeros(len(tri.triangles), dtype=mesh.Mesh.dtype)
top_mesh = mesh.Mesh(data, remove_empty_areas=False)
top_mesh.x[:] = x_top_sma[tri.triangles]
top_mesh.y[:] = z_top_sma[tri.triangles]
top_mesh.z[:] = Y_top_smootha[tri.triangles]
top_mesh.save('top_surface.stl')

##################################################################
# Plots
##################################################################

ax = plt.axes(projection='3d')
ax.plot_surface(x_bottom_sm,z_bottom_sm, Y_bottom_smooth)
ax.plot_surface(x_top_sm,z_top_sm, Y_top_smooth)
ax.plot_surface(x_top_sm,z_top_sm, surf_top)
ax.plot_surface(x_bottom_sm,z_bottom_sm, surf_bottom)
plt.show()

##################################################################
# Exporting surfaces to text files with XYZ points
##################################################################

file_bottom = open("surface_bottom.txt","w+")
for i in range(N*smoothing_factor):
    for j in range(N*smoothing_factor):
        file_bottom.write(str(x_bottom_sm[i][j]) + " " + str(z_bottom_sm[i][j]) + " " +
str(Y_bottom_smooth[i][j]) + "\n")
file_bottom.close()

file_top = open("surface_top.txt","w+")
for i in range(N*smoothing_factor):
    for j in range(N*smoothing_factor):
        file_top.write(str(x_top_sm[i][j]) + " " + str(z_top_sm[i][j]) + " " +
str(Y_top_smooth[i][j]) + "\n")
file_top.close()
```

```
file_top_limit = open("limit_top.txt","w+")
for i in range(N*smoothing_factor):
    for j in range(N*smoothing_factor):
        file_top_limit.write(str(x_bottom_sm[i][j]) + " " + str(z_bottom_sm[i][j]) + " "
+ str(surf_top[i][j]) + "\n")
file_top_limit.close()

file_bottom_limit = open("limit_bottom.txt","w+")
for i in range(N*smoothing_factor):
    for j in range(N*smoothing_factor):
        file_bottom_limit.write(str(x_bottom_sm[i][j]) + " " + str(z_bottom_sm[i][j])
+ " " + str(surf_bottom[i][j]) + "\n")
file_bottom_limit.close()
```

II. Limit surface point cloud HyperMesh import script

```
proc p_ReadCloudPointFile {FilePath} {
	set fpt [open $FilePath]
	set buf [string map {, .} [read $fpt]]
	close $fpt
	set lines [split $buf \n]
	foreach line $lines {
		if {[scan $line "%f %f %f"x y z]==3} {
			*createnode $x $y $z
			}
	}
}

set fileTypes {
		{"Data"		{.dat} }
		{"All files"	*	}
}

set file_name  [tk_getSaveFile -filetypes $fileTypes -title "DataFile" ]
p_ReadCloudPointFile $file_name;
```